POLITECNICO DI TORINO

Corso di Laurea Magistrale in

INGEGNERIA BIOMEDICA

Tesi di Laurea Magistrale

PLANE WAVE IMAGING METHODS FOR ULTRAFAST ULTRASOUNDS

Relatori

Prof. Filippo Molinari, Politecnico di Torino
Prof. Mengxing Tang, Imperial College London
Prof. Luca Mainardi, Politecnico di Milano

Candidato

Elena Hilary Rondoni

Anno Accademico 2018/2019

"Science is made up of mistakes,
but they are mistakes which it is useful to make,
because they lead little by little to the truth."

Jules Verne, *Journey to the Center*
of the Earth

Abstract

Ultrafast ultrasound is an imaging technique intended to replace conventional ultrasound scanning when very high temporal resolutions are needed, *e.g.* to detect movements or to reduce motion artefacts. Traditionally, echography consists in conveying focused ultrasound waves line by line and in juxtaposing the received backscattered echoes from each line. In the last decade, the development of parallel computing, especially in terms of GPUs (graphics processing units), paved the way to the definition of a new method for ultrasound imaging, namely the plane wave transmission. Thanks to this new technique, it is possible to insonify the entire image area in a single transmission, rather than using a number of focused lines. Plane wave imaging greatly decreases the time requested to perform a scan and allows to increase the frame rate by two orders of magnitude, reaching frequencies of thousands of Hz. Disadvantage of this technique is the absence of the focus, which allows to concentrate the energy in specific regions to improve the spatial resolution. As a consequence, even though the frame rate largely increases, the image quality worsens. Several studies have been carried out to restore the image quality while using this new imaging technique. A notorious attempt by Montaldo *et.al.* explored the use of a series of plane wave transmissions, each with a different steering angle, to be subsequently beamformed and coherently compounded into one single frame, in order to virtually and dynamically recreate focusing points. Nevertheless, according to this technique, a large number of plane waves is required to perfectly restore the image quality. Even though in this way the maximum frame rate decreases, the advantage of plane wave imaging still persists, as images obtained through this method, with comparable quality to those obtained with conventional ultrasounds, can still be acquired with higher frame rates than traditional ones. Later on, other studies based on the Montaldo method directed their research towards higher quality ultrafast images. Two techniques in particular are reported and compared in this work: multiplane waves imaging and cascaded dual-polarity waves

imaging. Their objective is to find a way of amplifying the transmitted signal amplitude, to improve the image quality, without causing any damage to the fragile transducers or any bioeffect risk to the imaged area. This work aims at identifying how to implement these techniques in an ultrasound simulator and under which conditions one is suggested over the others.

Acknowledgements

I wish to express my sincere gratitude to all the people that contributed in the making of this thesis work, as well as to those that stood at my side during the last two years of my master studies.

First, I would like to thank my best friend Cristina, who, even though I didn't share the higher education path with, has always backed me up whenever I needed, giving me all the warmth and kindness that I could ever hope for.

I wish also to thank the Pizza & Drones group, with whom I shared some very relaxing afternoons dedicated to...eating pizza and flying drones.

A special thanks goes also to Adrian, who supported and encouraged me in any possible way in order to get over many adversities.

I cannot but add to this list also the dear to my heart Abajour group, which alleviated the sleepless nights and the demanding deliveries of the arduous Alta Scuola Politecnica program.

I would also like to thank the people from ULIS that helped me out during the realization of the following work, welcoming me in the incredibly unpredictable research experience. In particular, I am grateful to Professor Tang, for giving me the great opportunity of working alongside exceptionally talented people in a stimulating environment, and to Chee Hau, Antonio and Matthieu, who dedicated much of their time to support me.

Last, but certainly not least, I wish to thank my family. The last few years have been tough for all of us, but I am proud to say that my family stood up strong against all the hardships it has been through. Their fortitude has proved fundamental during my entire studies, and even more in the last two years. I apologize for being difficult to deal with countless times. I just want to let you know that you are the real incentive that keeps me going.

Thanks to everyone.

Contents

List of Figures

List of Abbreviations

RF	Radiofrequency
CPWC	Coherent Plane-Wave Compounding
DAS	Delay And Sum
SNR	Signal to Noise Ratio
TI	Thermal Index
MI	Mechanical Index
MPW	Multiplane Waves
CEUS	Contrast-Enhanced Ultrasound
CDW	Cascaded Dual-Polarity Waves
SVD	Singular Value Decomposition

Chapter 1

Introduction

1.1 Evolution of ultrasound

Ultrasound technology made its first appearance in history in form of SONAR (sound navigation and ranging), bio-inspired by bats' echolocation, as a way of detecting objects in "black boxes". Its development was prompted during World War II for military purposes, thanks to the introduction of the RADAR (radio detection and ranging), which can be effectively referred to as the medical ultrasound scanner precursor [1].

The first applications in the medical field came soon after, starting from the 60s. The following decades assisted to the maturity and the cost cutting of an impressive amount of disruptive technologies, especially in the electronic and digital fields, that triggered the feasibility and the commercialization of new and improved technologies, which beforehand could exist only in theory. Ultrasound technology, in particular, found its way into this technological development and market, thanks to its intrinsic advantages, that made it a valid alternative over other medical imaging techniques, such as magnetic resonance and computerized tomography. Among its advantages it is worth mentioning the temporal resolution, the use of non-ionizing radiations and the low cost. Ultrasound found its application in many medical sectors, ranging from obstetrics to cardiology, and its use is not limited to screening and diagnosis. Nowadays, it is possible to deploy this technology for therapy as well, thanks to the use of HIFU (high-intensity focused ultrasound), which is an ablation technique traditionally used for treating prostate and liver cancers, and only recently improved to treat inoperable tumours such as pancreatic cancer [2]. More modern applications deploy ultrasounds also for the so called sono-poration, which allows the

release of drugs from nanoparticles, that selectively accumulate in precise body locations. Ultrasounds greatly impacted the medical field, and many of their potentialities have yet to be discovered. As more technology enablers become available, new studies in the ultrasound field pave the way to unconventional imaging techniques.

In the last decade, thanks to the videogame industry, which demanded ever growing computational capabilities, parallel computing received an important boost with the development of GPUs (graphics processing units) [3]. This technology represented a revolution also in the way of performing ultrasound scans. It was in fact implemented to promote software-based architectures rather than hardware-based ones. In this way, the signal processing for each channel can be performed at software level, thus allowing the possibility of processing multiple channels altogether. The passage from a serial architecture to a parallel one permits the so-called ultrafast ultrasound imaging [4].

1.2 Ultrasound principles

Ultrasound is a sound wave, *i.e.* a mechanical wave, which propagates with frequencies higher than those audible by humans ($>$ 20 kHz [5]). In particular, the frequencies generally employed in the medical field are over 2 MHz [6].

Ultrasounds are generated thanks to piezoelectric materials, which are crystals that present in their lattice some asymmetries. Because of their peculiar structure, they are transducers which convert mechanical energy into electrical energy and vice-versa. Therefore, to generate an ultrasound wave with a certain frequency, it is sufficient to apply a voltage wave with the same desired frequency to the crystal. This effect is referred to as inverse piezoelectric effect. The same material can be exploited to receive ultrasounds, as their energy distorts the crystal shape, thus generating an electrical signal, which can be subsequently read by electrical circuits. This effect is known as direct piezoelectric effect. The piezoelectric materials are therefore used both as source and receiver for ultrasound waves. It is obvious, however, that the transmitting and receiving phases must be alternated, since the crystals can not operate in both modalities at the same time.

Being a mechanical wave, ultrasound propagates in a medium thanks to compression and rarefaction movements, reason why the ultrasound speed of propagation is strongly

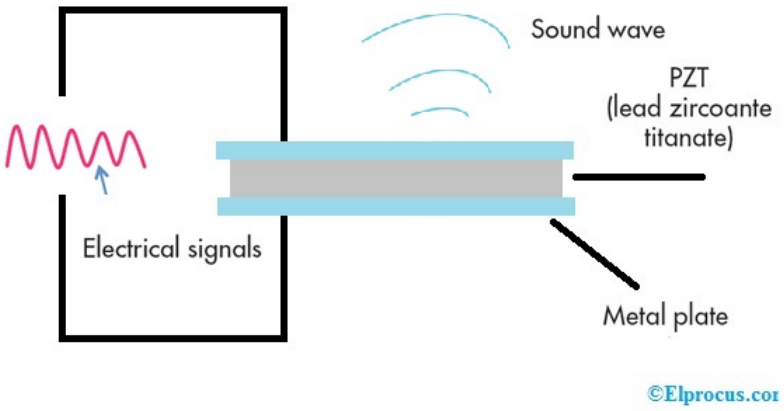

Figure 1.1: Example of a piezoelectric material [7]

correlated to the elastic properties of the medium itself. The stiffer a material is, the faster the ultrasound propagates. For instance, the speed can reach 4000 m/s in bones, while it is generally assumed that in soft tissues the speed reaches 1540 m/s.
While propagating in a homogeneous medium, ultrasounds are subjected to attenuation according to the following expression:

$$A(z) = A_0 e^{-\alpha z} \tag{1.1}$$

where,

$A(z)$ = ultrasound amplitude at depth z;

A_0 = initial ultrasound amplitude;

α = attenuation coefficient, which depends on the medium.

When ultrasounds reach an interface between two different tissues, they can either get reflected or transmitted. The magnitude of the reflection and, therefore, the amplitude of the received echoes, is dictated by the acoustical impedance, or better, the difference in acoustical impedances of the tissues forming the interface. Namely, the reflection coefficient is:

$$R = \left(\frac{Z_1 cos\alpha_2 - Z_2 cos\alpha_1}{Z_1 cos\alpha_2 + Z_2 cos\alpha_1} \right)^2 \tag{1.2}$$

where,

$Z_{1,2}$ are the acoustical impedances of the two materials;

$\alpha_{1,2}$ are respectively the incident and refracted angles.

Generally this expression is further simplified by considering an orthogonal incidence:

$$R = \left(\frac{Z_1 - Z_2}{Z_1 + Z_2}\right)^2 \tag{1.3}$$

It is worth noticing that, contrary to common believes, the acoustical impedance is not an intrinsic property of the material, as it depends not only on the density, but also on the speed of the ultrasound in the medium itself.

Another important relation concerning ultrasound speed and frequency is the following:

$$v = \lambda f \tag{1.4}$$

where λ is the wavelength, which is also a measure of the maximum spatial resolution. In fact, structures with dimensions smaller than the wavelength can not interact with the ultrasounds and, thus, can't be detectable. Consequently, to improve the spatial resolution it is sufficient to increase the frequency. However, waves with higher frequencies are also more subject to attenuation. Therefore, the maximum depth reached by the ultrasounds decreases. Depending on the type of application, a trade-off is necessary to better image organs and tissues at different depths. The more a study subject is deep, the lower the frequency should be.
Besides, another factor adds to diminish the maximum resolution. In fact, waves are normally sent in packets, comprehending therefore more than one cycle, *i.e.* more than one λ. If two objects along the ultrasounds path are at a distance less than the length of the packet, their echoes are not distinguishable. A solution would be therefore to use less cycles in a transmission. However, the uncertainty principle by Heisenberg states that "both velocity and position can not be determined simultaneously with arbitrary accuracy" [8]. Thus, when shorter packages are sent, the echoes received present larger bandwidths and don't allow to reconstruct the correct frequency of the waves. On the other hand, longer packages permit to distinguish the expected frequency, but the resolution inevitably worsens.

A very important advantage of ultrasounds is that they can be easily focused through the use of lenses positioned over the transducers, or through dynamic focusing, by applying

different delays to the transducers array. It is a very common practice to use focused beams, as they allow to concentrate the ultrasound energy in specific zones. Hence, the spatial resolution can be increased where the focus is positioned. Usually, along a scanning line, multiple focus points are applied, to improve the resolution also at different depths.

1.3 Ultrafast ultrasounds

Conventionally, the medium is insonified using multiple subsequent focused beams, and the image is reconstructed by juxtaposing each scanning line. Without considering potential processing times to reconstruct the image or to improve its quality, this procedure allows to obtain one frame, after the transducer channels have subsequently transmitted the beams and received the reflected echoes.

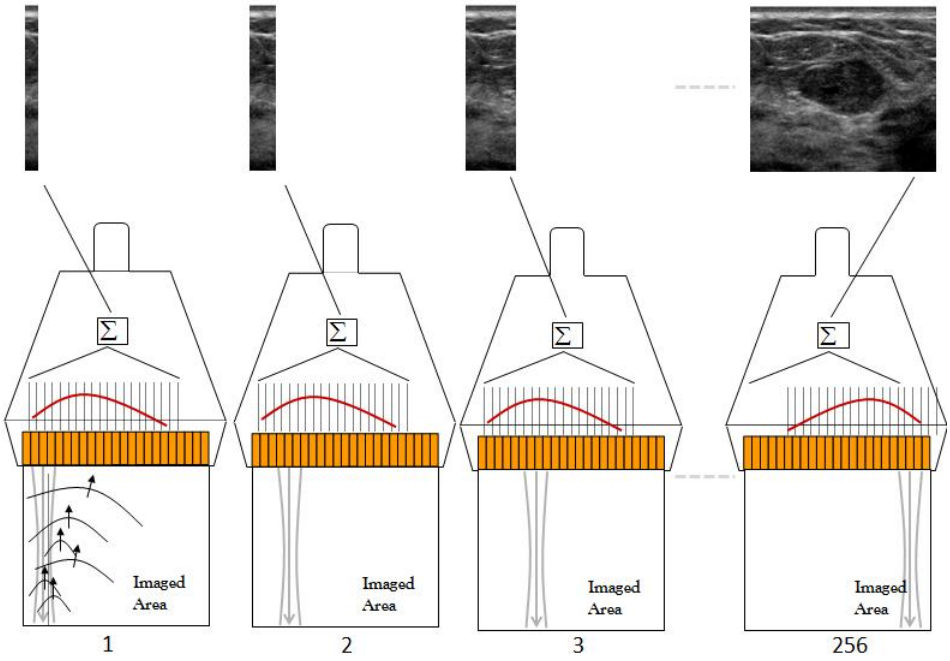

Figure 1.2: Ultrasound scanning line by line [4]

Therefore, the time requested to produce one image is:

$$T_{frame} = \frac{N_{lines} * 2 * z}{c} \tag{1.5}$$

where,

N_{lines} = number of scanning lines;

z = maximum image depth;

c = wave propagation speed in the medium.

Generally, the ultrasound speed is assumed to be constant and equal to 1540 m/s. Therefore, the maximum frame rate that can be achieved using traditional scanning modalities is:

$$FR_{max} = \frac{1}{T_{frame}} \tag{1.6}$$

The limitations of this method are quite evident, especially when it is necessary to increment the frame rate. For most imaging techniques, time is what hinders a good quality. The more time an image requires to be reconstructed, the more motion artefacts are present. It is therefore fundamental to have fast acquisition times. In case of 3D images, the number of scanning lines increases and, accordingly, the time required to reconstruct a volume as well, hence providing lower quality images. Same goes for motion studies, such as echocardiograms. In order to appreciate moving objects, the frame rate should be high enough to perceive the movements.

To overcome conventional architecture's limitations, it is necessary to have available an ultrafast data link between the computer and the acquisition module of the hardware system, and enough computing capabilities to perform beamforming, which will be later described, and signal processing for multiple parallel channels at software level.
Thanks to current parallel computing capabilities, it is possible to achieve this ultrafast architecture, thus allowing an increment in the frame rate and, therefore, a reduction of motion artefacts. Instead of scanning the medium line by line, now multiple channels can transmit altogether with null delays, creating unfocused plane waves. In this way, the whole image area can be acquired in the same time period necessary for only one line scan. This new technique has an image reconstruction process which differs from the one used in conventional ultrasounds, as it doesn't draw inspiration from the concept of the sonar. In fact, the theory at its core is related to the so-called optical holography, first envisioned by Denis Gabor [9], to improve the resolution obtained through an electron microscope. Even though he wasn't successful in applying his theory to electrons, he accomplished his intents with optics. He could reconstruct an object portrait from its light diffraction properties thanks to the wavefront reconstruction method [10].

This concept can be transferred to the acoustic field as well. M. Fink [11] proposed a time-reversal method, that allows the reconstruction of an area even when using wide wavefront transmissions. After registering the backscattered echoes, the received signals are time-reversed and re-emitted. Since these signals bring with them the memory of the "diffused" shape of the scattering objects present in the medium, and the medium characteristics as well, when they get reflected for a second time, a focusing process occurs, allowing, therefore, to optimally reconstruct the field at the second receiving session.

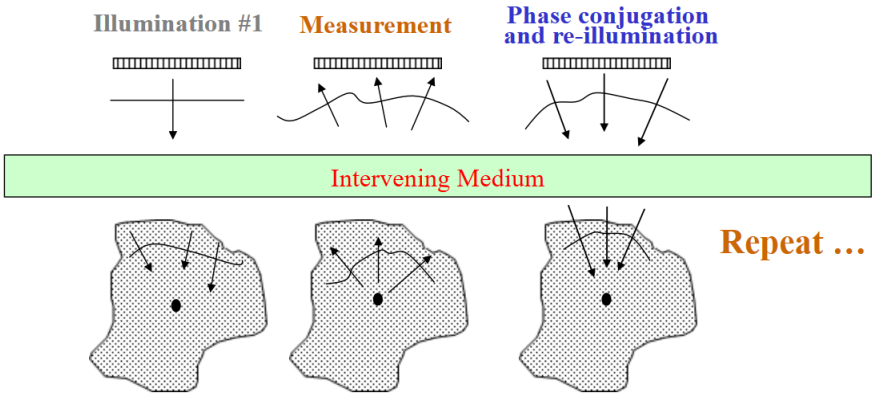

Figure 1.3: Time-reversal method

Nowadays, thanks to the computational power available, this method can be easily converted into a numerical one. Hence, it can be completely performed at software level, supposing homogeneous medium properties. This is commonly known as parallel beam-forming process.

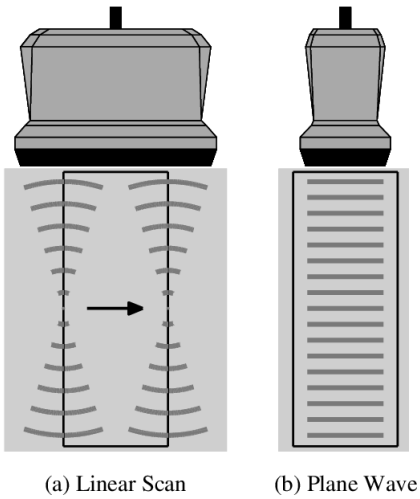

Figure 1.4: Comparison between insonification line by line with focus (a) and insonification with plane waves (b) from [12]

However, as every engineering problem, there is a trade off: if something improves, something else inevitably worsens. In this case, the frame rate can increase by a few hundreds fold with respect to conventional ultrasounds [4], but the single images appear with worse quality in terms of spatial resolution and contrast. This is caused by the absence of a focus, which is in fact the zone in which the resolution is higher. To restore the conventional imaging quality, Montaldo *et.al.* proposed a method to improve the beamforming process by virtually creating a focus. To reconstruct a single frame, multiple plane waves are used, each with a different steering angle, obtained by properly delaying the channels transmissions, as shown in Figure 1.5. This method is named coherent plane-wave compounding [13], and will be thoroughly described in Chapter 2.

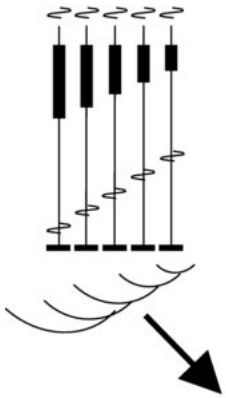

Figure 1.5: Generation of tilted plane waves by delaying the signals in each channel [14]

Spatial compounding is indeed a common practice in ultrasounds, as it allows to reduce the speckle effect of the image, *i.e.* the granular aspect, caused by interferences generated by the propagation of the backscattered waves. Speckle noise is said to be a deterministic type of artefact [15], which means that it would appear in the same way under identical acquisition conditions. Nevertheless, the speckle intensity pattern is treated in a statistical way, in most works using the following Rayleigh probability density function:

$$p(A;\Psi) = \frac{A}{\Psi} exp\left(\frac{-A^2}{2\Psi}\right) \tag{1.7}$$

where,

A = intensity of the pixel;

Ψ = scale parameter of the distribution.

Spatial compounding behaves in a similar way to the averaging method used in signal processing to reduce noise. The idea is to scan the medium as many times as possible, with different steering angles, in order to change the speckle pattern each time. Subsequently, the resulting images are averaged. The scattering objects which repeat in multiple images are more likely to actually be present in the medium. Those which instead in most images don't appear are probably noise components. Hence, by summing the images, the real scatterers are enhanced, whereas the noise is diminished.
In the past, incoherent compounding was generally adopted to reduce this artefact. Only recently, coherent compounding was tested and compared to the incoherent one. The difference between the two methods stands in the position of the summation step along the image processing chain. The coherent summation is performed with radiofrequency (RF) data, *i.e.* when the signals still present their in-phase and quadrature components, whereas, the incoherent summation involves the intensity values of the images, which are obtained by finding the envelope of the received signals. In the latter case, every information on the phase is lost, hence the name incoherent. Even though there are not extensive studies on the effects of coherent compounding, it seems that images thereby obtained not only appear less granulated, but also present improved resolution compared to those reconstructed through incoherent compounding [16].
Consequently, to improve the image quality, it is necessary to perform as much plane wave transmissions as possible. At first glance, the problem of long acquisition times seems to be repeating. However, this method presents several advantages [4]:

- **Dynamic focus**: compared to the conventional ultrasounds physical focusing, thanks to ultrafast ultrasounds it is possible to achieve dynamic focusing at different positions, by coherently summing images obtained with different angles [17]. In this way, each pixel can be virtually positioned at the focus and the resulting images appear more homogeneous;

- **Higher frame rate**: Montaldo demonstrated that, even though the frame rate decrements to obtain higher image quality, an image obtained through the plane waves compounding method, with equivalent quality to one obtained with conventional ultrasounds, is nevertheless acquired with higher frame rate (more than a hundred fold) [13];

- **Ultrafast applications**: it is possible to increase the frame rate to thousands of Hz by slightly lowering the image quality, but leaving it good enough to perform novel studies, such as those about shear wave elastography[1].

The same plane wave compounding technique can be used to reinvent also color flow Doppler images, whose frame rates generally suffer from the physicians need of using duplex or triplex modes (B-mode, color flow and PW-mode images displayed simultaneously). Ultrafast ultrasounds allow to track faster blood flows and, therefore, to detect in a more precise way cardiovascular diseases. Reminding that there is a connection between the frame rate and the number of steering angles used for each image, it is evident that if a high frame rate is used to perceive faster movements, the number of angles used for the images compounding is limited. Therefore, the quality of the image worsens. Nevertheless, it has been proved that, to obtain conventional Doppler images quality, it is not necessary to use numerous steering angles, allowing therefore to adopt very high frame rates [19]. Besides, the plane wave compounding proves very useful also when it comes to slow blood flow. In this case, the frame rate can be lowered, and, thus, the number of angles deployed for each image can be increased. This situation perfectly suits microvasculature, *i.e.* arterioles, venules, and capillaries. In fact, this portion of the circulatory system is responsible for the delivery of nutrients, and for the oxygen and carbon dioxide exchange with tissues. To allow an efficient transport, it is fundamental to slower the blood flow, in order to give time for the delivery processes to occur [20]. For instance, capillary blood flow average speed is around 1 cm/s, whereas aorta reaches 30 cm/s [21]. Because of this, it is possible to use lower frame rates. The number of steering angles can increase, and so the image quality, permitting to discern deeper and smaller vessels than those detected with traditional Doppler images. Ultrafast ultrasounds paved also the way to new groundbreaking imaging applications, from the study of tumour angiogenesis to the study of brain activity using functional ultrasounds. The last represents, in fact, a valid alternative for studying brain haemodynamics and metabolism over the classical fMRI (functional magnetic resonance imaging) and NIRS (near-infrared spectroscopy) techniques [22].

[1] Shear wave elastography is a novel ultrasound imaging technique used to assess mechanical properties of biotissues. Namely, thanks to this technique it is possible to quantify the viscoelasticity of soft tissues. Without ultrafast ultrasounds, it is virtually impossible to observe such shear waves, as their propagation in medium is strongly affected by tissues viscosity. The sampling frequency required to respect the Nyquist limit is over 1000 Hz [18]

Chapter 2

Coherent Plane-Wave Compounding

As previously anticipated, it is possible to restore a B-mode image quality in an ultrafast image thanks to the coherent plane-wave compounding (CPWC) method, proposed by Montaldo [13]. Its main steps comprehend two techniques:

- **Beamforming**
- **Transmission of multiple tilted planes**

Following Montaldo's demonstrations [13], let's give more details about them.

2.1 Beamforming

Beamforming is a spatial filter deployed for directing signal transmissions and/or receptions. It is commonly used for improving the quality of wireless connections, as it allows to locate the position of the connected devices.
Its application in the ultrafast ultrasound field is extensive, and may be in fact considered crucial, since with plane waves transmissions there is no focusing. Hence, as one would expect, the echoes, generated by the reflection of a plane wave, propagate in multiple directions. The core idea of the beamforming process is to collect and reunite all the RF data generated from a single scatterer.
To better understand how beamforming works, let's consider Figure 2.1.

The x-axis follows the same direction of the transducers array, while the z-axis represents the depth direction. Let's define $RF(x_1, t)$ as the signal sensed by the receiving

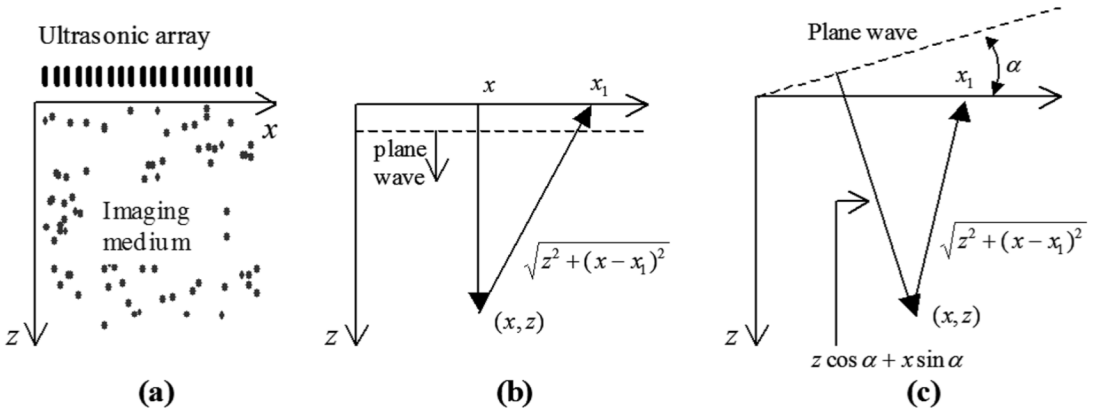

Figure 2.1: Beamforming: (a) definition of the system; (b) computation of the distances when the plane wave has no steering angle; (c) computation of the distances when the plane wave is tilted by α [13]

transducer in position x_1 on the x-axis at time t. Let's also separate the propagation in the medium in two stages: the travel from the transducer to the scatterer, to which the subscript 1 will be applied, and the travel from the scatterer back to the transducer, for which the subscript 2 will be adopted. Finally let's define a single scatterer in the medium at the position (x, z).

If no steering angle is applied to the plane wave, the times required for the two listed stages are the following:

$$\tau_1(\alpha = 0, x, z) = z/c \tag{2.1}$$

$$\tau_2(x_1, x, z) = \sqrt{z^2 + (x - x_1)^2}/c \tag{2.2}$$

The speed in the medium c is assumed to be constant and equal to $1540 m/s$. Hence, the total time required for the wave to propagate in the medium and to go back to the transducer is:

$$\tau(\alpha, x_1, x, z) = \tau_1 + \tau_2 \tag{2.3}$$

In order to reconstruct the scatter point in the position (x, z), it is now sufficient to delay the echoes by τ and coherently sum them. This common beamforming technique is in fact named after these two steps delay-and-sum (DAS) beamforming.

The pixel in (x, z) can be reconstructed using the following equation:

$$s(x, z) = \int_{x-a}^{x+a} RF(x_1, \tau(\alpha, x_1, x, z))dx_1 \tag{2.4}$$

where a corresponds to half of the aperture contributing to the overall backscattered signal. This value can be calculated according to the following expression:

$$F = z/2a \tag{2.5}$$

where F is the F-number, which is in fact defined as the ratio between the focal length and the aperture. Generally it is desirable to keep the F-number constant all over the image.

When the transmitted plane has an inclination α, the formulas for the beamforming process remain identical apart from the calculation of τ_1, in order to consider the time requested to create the different delays in the channels:

$$\tau_1(\alpha, x, z) = (zcos\alpha + xsin\alpha)/c \tag{2.6}$$

2.2 Transmission of multiple tilted planes

2.2.1 Plane waves compounding-multifocus beam equivalence

As previously stated, a single plane transmission generates a lower quality image with respect to conventional linear scanning, due to the absence of a focus. However, thanks to coherent compounding of N images, obtained with plane wave emissions, it is possible to create a synthetic focus.

To show this equivalence, let's hypothesize that the tissues have a linear response to the waves. Therefore, the backscattered echoes, obtained with both methods, can be expressed as the convolution of the initial pressure fields with the impulse response, which combines both transducers and tissues response:

$$RF(x_2, t) = \int p(x_1, t) * h(x_1, x_2, t)dx_1 = \int\int p(x_1, t')h(x_1, x_2, t - t')dt'dx_1 \tag{2.7}$$

where x_1 indicates the transmitting point, whereas x_2 represents the receiving point on the x-axis.

To reconstruct the image in a generic point (x, z), beamforming is performed using the

previously described DAS method (Equation 2.4):

$$s(x,z) = \int RF(x_2, \tau(x,z,x_2))dx_2 \tag{2.8}$$

where, the expressions to obtain τ will change depending on the type of transmission used. Substituting (2.7) in (2.8) the following is obtained:

$$s(x,z) = \int\int\int p(x_1,t')h(x_1,x_2,\tau(x,z,x_2)-t')dt'dx_1dx_2 \tag{2.9}$$

This expression is still valid for both compounding and focused techniques. Nevertheless, as the ultimate objective is to compare them, it is necessary to separate the transmitting and receiving phases in (2.9) to reduce the problem complexity. This choice is motivated by the fact that the differences between the two methods lie in the first of the two phases. For the focused case, no steering angle is applied to the wave, while for the compounding case multiple tilted emissions are performed and compounded.
To achieve this separation, let's consider τ, that is in fact made up of two components, *i.e.* the propagation from the transducers into the medium and the propagation from the scattering points back to the transducers. As already done similarly in (2.3), let's express τ as:

$$\tau(x,z,x_2) = \tau_1(\alpha,x,z) + \tau_2(x,z,x_2) \tag{2.10}$$

If the transmission method implies focused linear scanning, τ_1 can be expressed as:

$$\tau_1(\alpha = 0, x, z) = z/c \tag{2.11}$$

whereas, if multiple plane waves, each with a different steering angle, are used:

$$\tau_1(\alpha_i, x, z) = (zcos\alpha_i + xsin\alpha_i)/c \tag{2.12}$$

Instead, τ_2 is the same for both types of acquisition and its expression is the same found in (2.2):

$$\tau_2(x_2, x, z) = \sqrt{z^2 + (x - x_2)^2}/c \tag{2.13}$$

Substituting (2.10) in (2.9):

$$s(x,z) = \int\int\int p(x_1,t')h(x_1,x_2,\tau_1(\alpha,x,z)+\tau_2(x,z,x_2)-t')dt'dx_1dx_2 \tag{2.14}$$

and replacing:

$$t'' = t' - \tau_1(\alpha,x,z) \tag{2.15}$$

the reconstructed image can be expressed as:

$$s(x,z) = \int\int\int p(x_1,t''+\tau_1(\alpha,x,z))h(x_1,x_2,\tau_2(x,z,x_2)-t'')dt''dx_1dx_2 \tag{2.16}$$

where t'' is the new integration variable.

As one can notice, in this last expression the transmitting and receiving terms are finally separated respectively in the pressure fields and the impulse response. Thus, it is possible to make the comparison between the two methods.
First, let's express (2.16) for the compounding case. Supposing that N planes are used for the compounding process:

$$s_c(x,z) = \int\int\int \left[\sum_{i=1}^{N} p_c^i(x_1,t''+\tau_1(\alpha_i,x,z))\right]h(x_1,x_2,\tau_2(x,z,x_2)-t'')dt''dx_1dx_2 \tag{2.17}$$

Let's express (2.16) for the focused case as well:

$$s_f(x,z) = \int\int\int p_f(x_1,t''+\tau_1(\alpha=0,x,z))h(x_1,x_2,\tau_2(x,z,x_2)-t'')dt''dx_1dx_2 \tag{2.18}$$

The impulse response h remains the same for both techniques. Hence, if the first term related to the pressure fields is the same as well, it is eventually demonstrated that the techniques provide the same exact information:

$$\sum_i p_c^i(x_1,t''+\tau_1(\alpha_i,x,z)) = p_f(x_1,t''+\tau_1(\alpha=0,x,z)) \tag{2.19}$$

As shown in Figure 2.2, the term on the left of the equation could therefore be imagined as an equivalent to the wave with a focus in the position (x,z).

By changing the delays it is possible to move the focus in different positions, both in depth and laterally. This is one of the most crucial advantages of the compounding

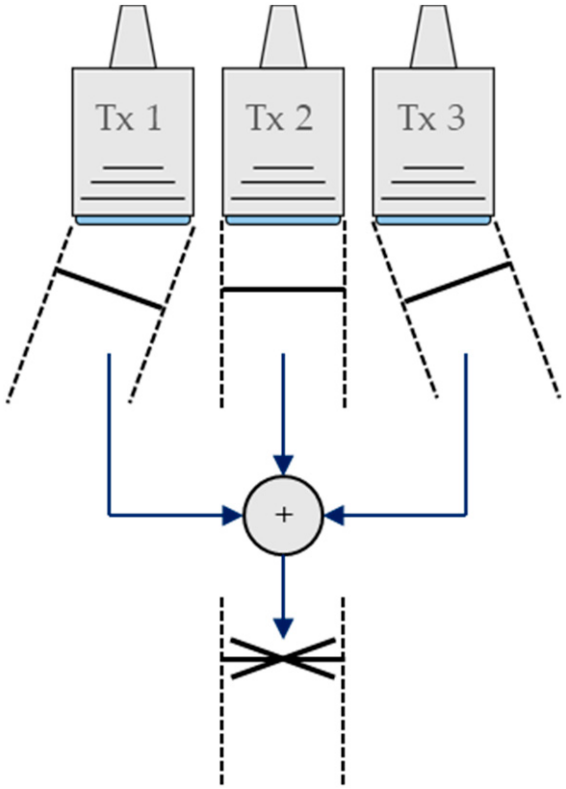

Figure 2.2: Compounding between planes with different steering angles [23]

technique, which allows therefore to preserve the same image of a multi focused linear scanning, while incrementing the frame rate.

2.2.2 Angles choice

To better acknowledge the parameters importance and magnitude in the equivalence, let's further analyse it by expressing the monochromatic plane waves in their complex form, where propagations both in time and space are explicitly expressed:

$$p_c^i(x,z,t) = p_0 e^{j(xk_x^i + zk_z^i - \omega t)} \tag{2.20}$$

where,

$k_x^i = k_0 sin\alpha_i$

$k_z^i = k_0 cos\alpha_i$

are the x and z components of the wavevectors, and:

$k_0 = 2\pi/\lambda$

An important matter to establish a good image quality in the compounding method

is the choice of number of angles and the step between them. To define which angles α_i to use, let's first make an observation. As shown in Figure 2.3, a transducer array is constituted by a finite number of elements, which are spaced by the pitch, which is the sum of width and kerf.

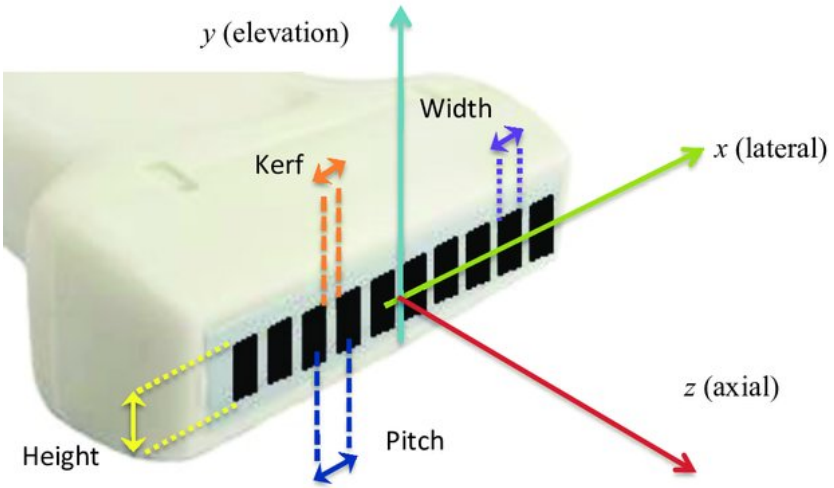

Figure 2.3: Geometry of the elements of an array [24]

Because of this discretization, a spatial filter is applied to the transmitted signals, as it is not possible to send more lines than the number of elements in the x direction. Thus, we may define the sampling spatial frequency as $1/dx$, where dx is the pitch. To use the same space of the wavevector, the sampling frequency is expressed in radians $k_{samp} = 2\pi/dx$. The wavevectors components along x, which are indeed the spatial frequencies along x, have a spectrum defined by the range:

$$(-\frac{pi}{dx}, \frac{pi}{dx}) \tag{2.21}$$

If the transducer array has n_t elements, then:

$$k_x^i = \frac{2\pi}{dx}\frac{i}{n_t}, \qquad i = -\frac{n_t}{2}, ..., \frac{n_t}{2} - 1 \tag{2.22}$$

The number of elements multiplied by the pitch gives exactly the length of the array L. Thus, the previous equation can also be expressed as:

$$k_x^i = i\frac{2\pi}{L}, \qquad i = -\frac{n_t}{2}, ..., \frac{n_t}{2} - 1 \tag{2.23}$$

Combining the two provided definitions for k_x^i, it is possible to define the angles α_i that allow to avoid any loss of spectral information:

$$\alpha_i = arcsin(i\lambda/L), \qquad i = -\frac{n_t}{2}, ..., \frac{n_t}{2} - 1 \tag{2.24}$$

Since λ is much smaller than L, α_i can also be expressed as:

$$\alpha_i \approx i\lambda/L, \qquad i = -\frac{n_t}{2}, ..., \frac{n_t}{2} - 1 \tag{2.25}$$

Thanks to this expression it is possible to define the step between the angles and the number of plane waves to transmit.
However, there is not always the necessity of using all of them. To study how many are necessary to restore the image quality, let's go back to the definition of coherent compounding for $n \leq n_t$ plane waves. Let's also move the reference system origin in the focus by substituting $x' = x - x_f$ and $z' = z - z_f$:

$$p_c(x', z', t) = \sum_{i=-n/2}^{n/2-1} p_0 e^{j(x'k_x^i + z'k_z^i - \omega t)} \tag{2.26}$$

According to the Fresnel-Kirchhoff diffraction theorem [25], it is possible to reconstruct a plane wave propagation in each point of a medium from the knowledge of its behaviour at a generic depth. This theorem applies only if the medium itself can be considered homogeneous, isotropic and linear, and if the aperture used is much bigger than the pitch. Using these hypotheses, the previous equation can be simplified and solved for $z = z_f$:

$$\begin{aligned} p_c(x', t) &= \sum_{i=-n/2}^{n/2-1} p_0 e^{j(x'k_x^i - \omega t)} \\ &= \sum_{i=-n/2}^{n/2-1} p_0 e^{j(x'i2\pi/L - \omega t)} \\ &= p_0 e^{-j\omega t} \sum_{i=-n/2}^{n/2-1} e^{j(x'i2\pi/L)} \end{aligned}$$

This is a geometric series, whose partial solution is:

$$p_c(x', t) = p_0 \frac{j2sin(x'n\pi/L)}{[exp(jx'2\pi/L) - 1]} exp(-j\omega t) \tag{2.27}$$

The Taylor expansion for a complex exponential is:

$$e^{jx} = 1 + jx - \frac{x^2}{2!} - \frac{jx^3}{3!} + ... \tag{2.28}$$

Therefore, we can take the first order approximation and rewrite Equation (2.27) as

$$p_c(x', t) \approx p_0 \frac{j2sin(x'n\pi/L)}{[jx'2\pi/L]} exp(-j\omega t) \tag{2.29}$$

which is a *sinc* function:

$$p_c(x', t) \approx p_0 nsinc(x'n\pi/L) exp(-j\omega t) \tag{2.30}$$

This *sinc* expression is very similar to the one corresponding to the traditional scanning:

$$p_f(x, t) = p_0 g(z_f) sinc(xak_0/z_f) exp(-j\omega t) \tag{2.31}$$

where,

$$g(z_f) = \frac{2a}{\sqrt{\lambda z_f}} \tag{2.32}$$

is the gain which depends on the aperture $2a$, the wavelenght λ and the depth of the focusing point z_f.

In order to have the exact same *sinc* function in both (2.30) and (2.31):

$$\frac{x'n\pi}{L} = \frac{xak_0}{z_f} \tag{2.33}$$

As a result, the number of plane waves should be:

$$n = \frac{ak_0 L}{z_f \pi} = \frac{L}{\lambda F} \tag{2.34}$$

For instance, if the transducer array has 128 elements, the wavelength is approximately the pitch, and the F-number is 2, the number of angles required to have comparable images is 64.

2.3 Foundation for new imaging techniques

To conclude, this method shows great potentialities in the ultrafast imaging domain, as it allows to achieve the same quality of a conventional B-mode image, using less insonifications. Its intrinsic advantages paved the way to a number of studies to push even further this imaging technique. In the following two chapters, two of these studies are analysed. The proposed methods can effectively be considered progressive evolutions of the coherent plane-wave imaging technique, as they push the boundaries for the image quality, without the need to compromise the high frame rate.

Chapter 3

Multiplane Waves Imaging

As previously demonstrated the CPWC technique allows to restore the image quality of conventional B-mode images thanks to the combination of DAS beamforming and coherent compounding of multiple plane wave acquisitions. The obvious advantage that this technique brings about is the high frame rate. However, as shown in Figure 3.1, higher frame rates imply less steering angles and, therefore, less images to perform the compounding, as well as lower image quality.

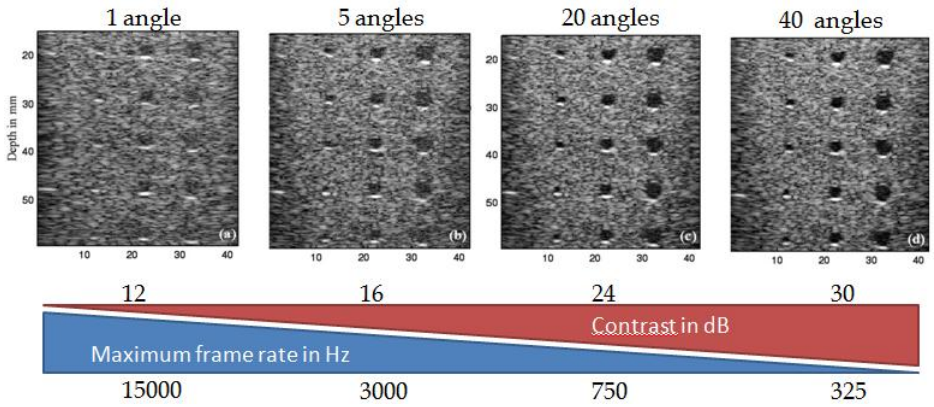

Figure 3.1: Maximum frame rate and contrast trade-off [4]

Consequently, it would be interesting to find a way to improve contrast and signal-to-noise ratio (SNR), without changing the number of angles deployed, and, thus, the frame rate.

There is indeed a way to achieve this goal. With the same imaging technique it is in fact sufficient to increase the voltage amplitude used to generate the waves. In this way, more energy is delivered to the medium and the backscattered echoes present higher amplitudes

as well. Even though this solution seems very simple to implement, most of the time it is not practicable. Some of the reasons comprehend the limitations in the electronics and the probe architecture, and the thermal index (TI) and mechanical index (MI) thresholds.

3.1 Thermal and mechanical indexes

TI and MI represent crucial factors in the use of ultrasounds, as they define the possibility of incurring into safety issues both from a mechanical and a thermal point of view [26]. MI is an estimate of the maximum amplitude that propagates in the medium and it is defined as the ratio between the negative peak of the pressure field and the square root of the frequency:

$$MI = \frac{p_r}{\sqrt{f}} \tag{3.1}$$

It therefore gives a measure of the magnitude of compression-rarefaction movements and of the mechanical damage. MI is fundamental also from the transducer point of view. In fact, the piezoelectric materials used for ultrasounds are usually very fragile. Maintaining the MI under a certain threshold, not only allows to avoid bioeffect risks, but also permits to ensure the transducers integrity.
Instead, TI is a ratio between two powers:

$$TI = \frac{W}{W_{deg}} \tag{3.2}$$

where,

W is the actual power transmitted to the tissue;

W_{deg} is the power necessary to increase the temperature by 1 °C.

For safety reasons, these two indexes are standardized by the Food and Drug Administration (FDA) to ensure regulatory uses. For B-mode images, the most crucial indicator is the MI [27]. For instance, when using ultrasounds for diagnostic purposes, the MI should be less than 1.9 [28]. This value prevents any bioeffects risk, only if the duration of the pulses is short enough. For longer transmissions it may be necessary to reduce the maximum threshold for the MI.
Besides, the use of microbubbles as contrast agent hinders the application of high voltages.

As shown in Figure 3.2, bubbles behave differently depending on the MI. The higher the MI is, the more the bubbles oscillate around different axes, generating therefore lower quality images. Ultimately, if the MI is too high, the bubbles can be subject to bursting, hence the signal needed to generate the contrast is lost. Furthermore, since the microbubbles travel along the circulatory system, their rupture may cause problems such as hemolysis, microvessels rupture and arrhythmia [29]. Therefore, for contrast-enhanced ultrasounds (CEUS), the MI should decrease to very low levels (usually around 0.2). Further details on the microbubbles behaviour will be given later in Section 3.5.

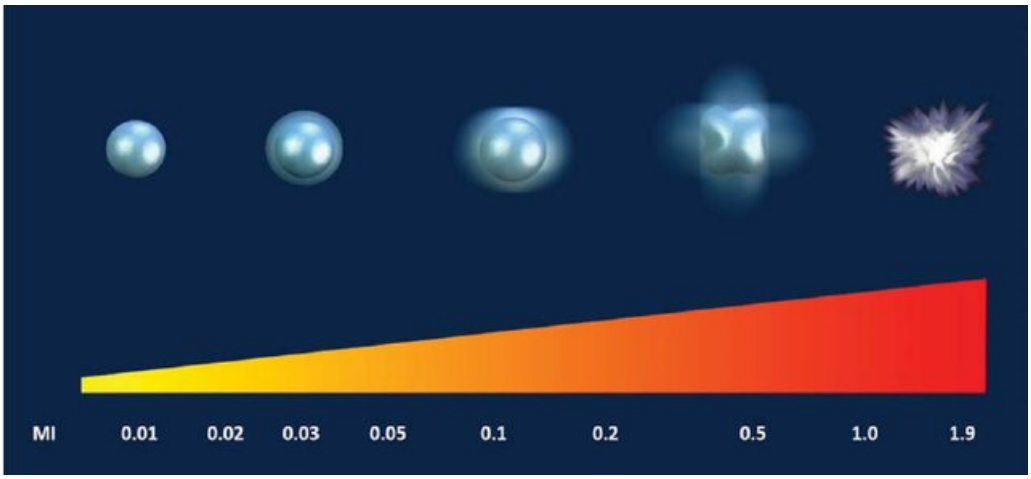

Figure 3.2: Behaviour of microbubbles in reference to the MI [30]

Generally, in the diagnostic field, common sense suggests to keep the MI and TI ALARP.

Although these considerations lead to think that it is therefore rather difficult to find a solution to the frame rate-quality trade-off, a study by Tiran *et.al.* [31] proposes a method, drawing inspiration from the CPWC, to increase the amplitude of the received signal, without the necessity of using higher voltages.
The following aims at describing this variant of the coherent plane-wave compounding method, which allows to further improve the image quality, namely in terms of signal-to-noise ratio, contrast and imaging depth.

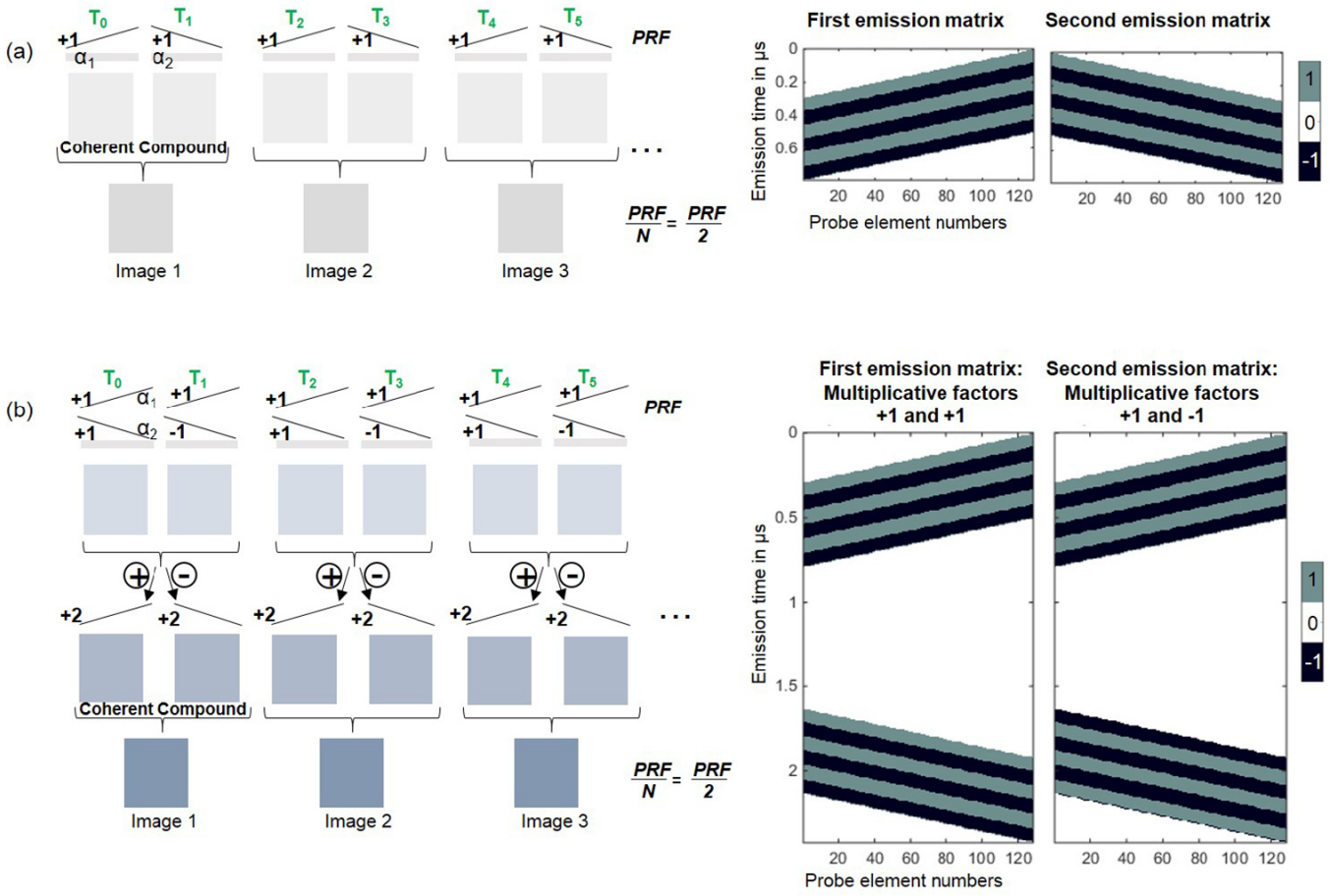

Figure 3.3: Comparison between the plane wave compounding method by Montaldo (a) and the multi-plane wave method by Tiran (b) [31]

3.2 Multiplane wave imaging principles

Let's observe Figure 3.3. On the top the CPWC method is represented, while on the bottom there is the multiplane wave (MPW) method. Let's suppose that only two angles are used for the compounding step. According to the first technique, two transmissions are performed, one for each tilting angle. In the Figure they are called T_0 and T_1 and they correspond respectively to the steering angles α_1 and α_2. The raw data received after each transmission is first beamformed. In this way, two radiofrequency images with low quality are created and are subsequently coherently compounded to create one single radiofrequency image with higher quality. Thanks to the Hilbert transform the intensity values are obtained and, eventually, with a logarithmic compression the first frame, denominated $Image1$ is available. The same steps are then repeated to acquire the following images. The frame rate is therefore defined by the time intervening between the T_i transmissions and the number of angles used for the compounding process. Let's define the time between

the transmissions as pulse repetition period (PRP). This time interval will depend on the type of application, as it establishes the maximum imaging depth. The frequency deriving from PRP is defined as pulse repetition frequency (PRF). In conclusion, if N different plane waves are used during compounding, the overall frame rate is:

$$FR = \frac{PRF}{N} \tag{3.3}$$

In the example only 2 plane waves are used. Therefore, the resulting frame rate will be $\frac{PRF}{2}$.

The method proposed by Tiran, follows a similar concept, but it grants the compounding between images as if they were acquired with higher amplitudes in the transmissions, while preserving the same exact frame rate. Let's analyse this technique in detail.
As for the previous method, only two transmissions are used, T_0 and T_1, thus allowing to keep the same frame rate $\frac{PRF}{2}$. The difference between CPWC and MPW consists in how each transmission is performed. As one can notice from Figure 3.3, during T_0, two plane waves are sent. These two are the exact same type of plane waves used in Montaldo's method, *i.e.* with steering angles α_1 and α_2. They are sent one after the other in a very short time period dt (usually at most 1 μs) and they both present the same polarities used in the previous method. The second transmission T_1, is performed nearly in the same way. The only difference consists in the change of polarity for the second wave. We can describe this choice with the following matrix:

$$\begin{array}{c} \\ \alpha_1 \\ \alpha_2 \end{array} \begin{array}{c} \begin{array}{cc} T_0 & T_1 \end{array} \\ \begin{pmatrix} +1 & +1 \\ +1 & -1 \end{pmatrix} \end{array} \tag{3.4}$$

where, the columns express the polarities assigned to each transmission, while the rows represent the waves polarities for each steering angle. In this example, the first column corresponds to T_0, and the second to T_1, while the first row has the polarities assigned to the plane wave with steering angle α_1 and the second row has the polarities assigned to to planes with angle α_2.
Because of this implementation, the final results of the acquisitions will be two radiofre-

quency images, with low quality, a bit different with respect to those obtained in the previous method. In fact, each image seems to be a superposition of two images, acquired with different steering angles, one slightly delayed with respect to the other. We might express the signals transmitted in T_0 and T_1 as in the following:

$$\begin{cases} x_1(t) = s_{\alpha_1}(t) + s_{\alpha_2}(t - dt) = s_{\alpha_1}(t) + s_{\alpha_2}(t) * \delta(t - dt)) \\ x_2(t) = s_{\alpha_1}(t) - s_{\alpha_2}(t - dt) = s_{\alpha_1}(t) - s_{\alpha_2}(t) * \delta(t - dt)) \end{cases} \tag{3.5}$$

where,

$s_{\alpha_{1,2}}$ are the two tilted plane waves sent in each transmission

$x_{1,2}$ are the two signals sent respectively in $T_{0,1}$

Therefore, the received signals will be:

$$\begin{cases} y_1(t) = x_1(t) * h(t) = s_{\alpha_1}(t) * h(t) + s_{\alpha_2}(t) * \delta(t - dt) * h(t) \\ y_2(t) = x_2(t) * h(t) = s_{\alpha_1}(t) * h(t) - s_{\alpha_2}(t) * \delta(t - dt) * h(t) \end{cases} \tag{3.6}$$

where $h(t)$ is the impulse response that takes into account the medium attenuation and the transducers response.

The next step is to coherently compound the two acquired images, in order to re-conduct them back to two images without any superposition. To achieve this, it is sufficient to perform coherent summation and subtraction of the two images. In fact, a summation will enhance the part of the image acquired with α_1 and, supposing linear behaviour for both the medium and the transducer, it will also cancel out the contribution of α_2. A subtraction will do exactly the contrary: enhance α_2 contribution and cancel α_1 contribution. Thanks to this technique it is possible to "separate" the two angles contributions in two different images, while increasing their amplitudes by 2. These passages can be expressed with the following system:

$$\begin{cases} y_1'(t) = y_1(t) + y_2(t) = 2s_{\alpha_1}(t) * h(t) \\ y_2'(t) = y_1(t) - y_2(t) = 2s_{\alpha_2}(t) * \delta(t - dt) * h(t) \end{cases} \tag{3.7}$$

One last aspect must be taken into account. After the separation, one can notice that the α_2 contribution is slightly delayed. Therefore, before proceeding to the next steps, it is necessary to realign the images, by translating $y_2'(t)$ upwards by the time delay dt used to separate the plane waves in each transmission:

$$\begin{aligned} y_2''(t) = y_2'(t+dt) &= y_2'(t) * \delta(t+dt) = \\ &= 2s_{\alpha_2}(t) * \delta(t-dt) * h(t) * \delta(t+dt) = \\ &= 2s_{\alpha_2}(t) * h(t) \end{aligned}$$

Now, the situation corresponds exactly to the scenario represented in the top part of Figure 3.3, with the only difference that the multiplication factor is no more +1, but it is now +2. At this moment, the steps defined by Montaldo can be followed normally: first beamforming and then coherent compounding. The resulting frame $Image1$ is exactly what we would obtain in the plane wave compounding method using double voltages in the transmission, without, however, incurring in the risk of exceeding the MI and without the need of performing more T_i transmission, *i.e.* without changing the frame rate.

3.3 Generalization of the method

This method can be generalized for any number of angles, thanks to the Hadamard encoding. To assign the polarities to each wave, it is sufficient to follow the definition of the Hadamard matrix of order n:

$$H_n H_n^T = nI_n \tag{3.8}$$

where n is the number of angles chosen for the compounding and can only be 1, 2 or a multiple of 4, representing therefore a limitation in the choice of the number of compounding angles. The matrix H_n, where $n = 2^k$, can be computed through an iterative process, thanks to Sylvester's construction steps [32]:

$$H_{2^k} = \begin{pmatrix} H_{2^{k-1}} & H_{2^{k-1}} \\ H_{2^{k-1}} & -H_{2^{k-1}} \end{pmatrix} \tag{3.9}$$

Let's generate for example the Hadamard matrix of order 4.
k in this case is 2. Therefore, the Hadamard matrices of order 2^{k-1} are H_2, which is the same matrix used in the previous example:

$$H_2 = \begin{pmatrix} +1 & +1 \\ +1 & -1 \end{pmatrix} \tag{3.10}$$

As a result:

$$H_4 = \begin{pmatrix} +1 & +1 & +1 & +1 \\ +1 & -1 & +1 & -1 \\ +1 & +1 & -1 & -1 \\ +1 & -1 & -1 & +1 \end{pmatrix} \tag{3.11}$$

Figure 3.4 shows the application of the Hadamard encoding of order 4 to the multiplane wave method.

The Hadamard matrix is used not only to define the polarities to be assigned to the planes in each transmission, as already explained, but it is also used to define the order of the summation and subtraction operations to be performed to separate the different angles contributions. For this example, the new system of equations will be:

$$\begin{cases} x_1(t) = s_{\alpha_1}(t) + s_{\alpha_2}(t) * \delta(t - dt_1) + s_{\alpha_3}(t) * \delta(t - dt_2) + s_{\alpha_4}(t) * \delta(t - dt_3) \\ x_2(t) = s_{\alpha_1}(t) - s_{\alpha_2}(t) * \delta(t - dt_1) + s_{\alpha_3}(t) * \delta(t - dt_2) - s_{\alpha_4}(t) * \delta(t - dt_3) \\ x_3(t) = s_{\alpha_1}(t) + s_{\alpha_2}(t) * \delta(t - dt_1) - s_{\alpha_3}(t) * \delta(t - dt_2) - s_{\alpha_4}(t) * \delta(t - dt_3) \\ x_4(t) = s_{\alpha_1}(t) - s_{\alpha_2}(t) * \delta(t - dt_1) - s_{\alpha_3}(t) * \delta(t - dt_2) + s_{\alpha_4}(t) * \delta(t - dt_3) \end{cases} \tag{3.12}$$

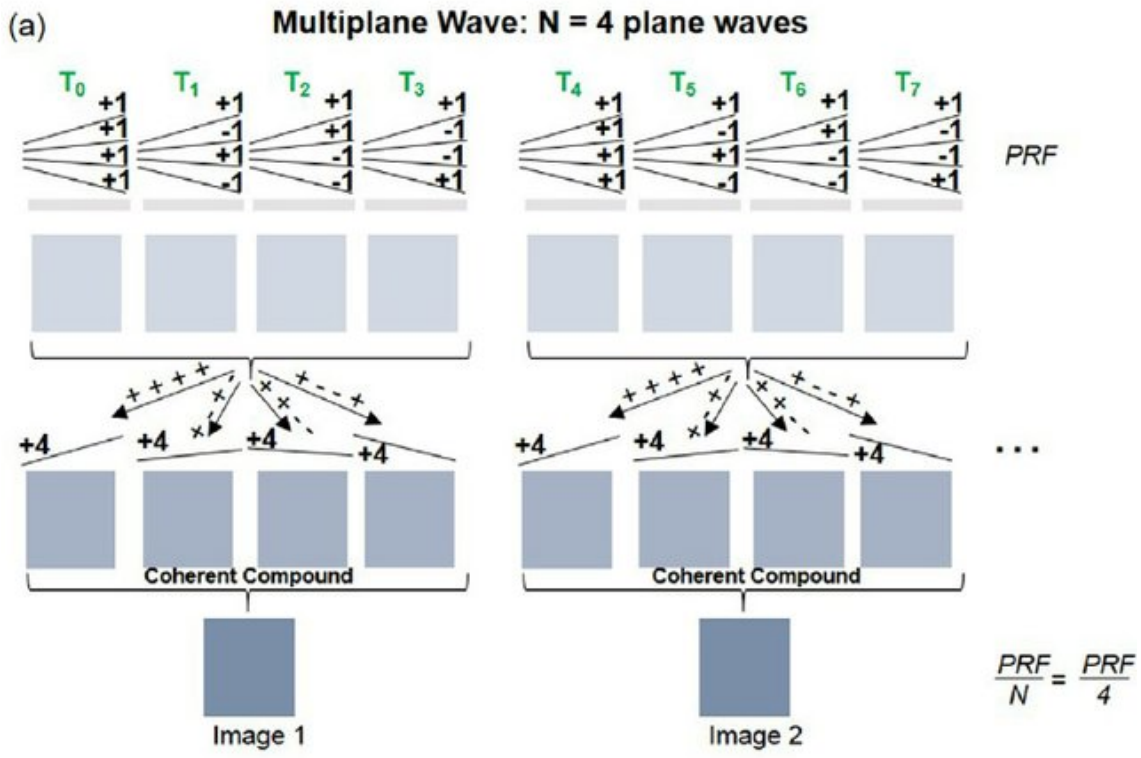

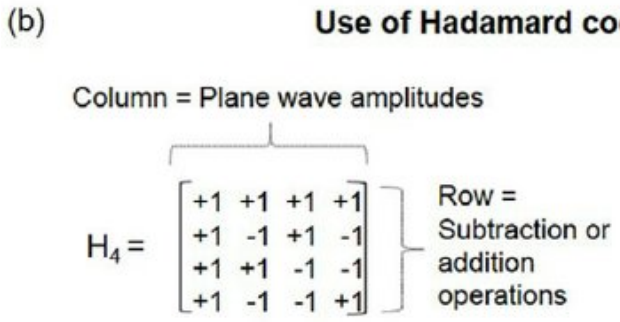

Figure 3.4: Application of the Multiplane wave method with four different steering angles [31]

and,

$$\begin{cases} y'_1(t) = y_1(t) + y_2(t) + y_3(t) + y_4(t) = 4s_{\alpha_1}(t) * h(t) \\ y'_2(t) = y_1(t) - y_2(t) + y_3(t) - y_4(t) = 4s_{\alpha_2}(t) * \delta(t - dt_1) * h(t) \\ y'_3(t) = y_1(t) + y_2(t) - y_3(t) - y_4(t) = 4s_{\alpha_3}(t) * \delta(t - dt_2) * h(t) \\ y'_4(t) = y_1(t) - y_2(t) - y_3(t) + y_4(t) = 4s_{\alpha_4}(t) * \delta(t - dt_3) * h(t) \end{cases} \tag{3.13}$$

3.4 Gain and Limitations

Thanks to MPW, the SNR of the B-mode image increases by:

$$10 \cdot \log_{10} N \tag{3.14}$$

where N is the number of angles or the number of acquisitions used to reconstruct one frame. Furthermore, compared to the coherent plane wave method, multiplane waves imaging allows to increase the sensitivity for shear wave elastography and to detect deeper structures, such as vessels in power Doppler images [31].

SNR and contrast improve especially for longer penetration depths, where we can suppose that noise is primarily generated by electronics rather than clutter artefact.

As usual, however, a new advantage brings about also a new disadvantage. As previously stated in the introductory chapter, transducers can not receive while they are transmitting. There will always be, therefore, a blind area of the medium, which can not be imaged. The depth of this area can be defined by the following expression:

$$d_{blind} \simeq \frac{c \times \Delta t}{2} \tag{3.15}$$

where Δt is the time required for completing a transmission. As a result, the longer the transmission is, the deeper the blind area is. For the Montaldo method, the minimum duration is limited simply by the inclination of the plane, which, for most cases, can be negligible, while in the Tiran method it also depends on the number of angles used for the compounding and on the time interval dt used between each plane. Thus, the more planes are used and the bigger the angle step is, the more crucial this blind area becomes. It could be possible to shorten the transmission duration by compacting the plane waves. However, this would imply that an higher MI is reached, risking therefore to get over the FDA threshold. To reduce the blind area it would be therefore necessary to decrease the voltage, partially losing the advantage of the MPW.

Hence, it is preferable to use this method when the structures to be examined are not superficial.

3.5 Contrast-Enhanced Ultrasound

In medical ultrasonography, air and bones are the media that most permit to obtain high differences in acoustic impedance with respect to the surrounding tissues. As a result, the images present higher contrast where soft tissues interface with either bones or air. To improve images' contrast it is in fact common practice to inject microbubbles, which are gas-filled spheres, stabilized by shells made mostly of surfactants, such as the second-generation microbubbles Sonovue [33]. In the diagnostic field, the contrast agent is used especially for echocardiography and microvasculature detection, since blood is only slightly echogenic. Other modern applications see the use of microbubbles for drug delivery, as a possible therapy for the treatment of tumours.
Since this work focuses on the use of ultrasounds for imaging purposes, the use of microbubbles for therapy won't be discussed.

3.5.1 Microbubbles behaviour

Microbubbles behave differently with respect to the surrounding tissues. Namely, when hit by low pressure fields, they generate a high non linear response, which is what allows a sharper distinction. Three of the most common imaging techniques employed in contrast-enhanced ultrasound (CEUS) are the amplitude modulation, the pulse inversion and the combination of both. They are similar to traditional imaging techniques, with the only difference that some operations are performed on the amplitude of the transmitted pulses. For instance, in amplitude modulation, pulses with half amplitude are alternated to pulses with full amplitude, whereas, in pulse inversion, the polarity of the pulses is alternately changed. The echoes generated by the two alternated pulses are then combined in order to nullify the linear response from the tissues and to enhance the non linear response from the bubbles.

3.5.2 MPW for CEUS

Since low pressure, *i.e.* low MI, is required both to avoid bubbles' disruption and to observe the non linearity, the imaging depth is restricted.
The multiplane wave method with Hadamard encoding is therefore particularly suitable for the use in combination with microbubbles, as it allows to enhance deeper structures,

without compromising the MI and the frame rate, as a study by Ping Gong *et.al.* demonstrates [34].

An example of application using only two compounding angles is reported in Figure 3.5 and Figure 3.6. Even though only two angles are used, the number of transmissions is now 4. This is because each plane wave must be retransmitted with half its amplitude to perform amplitude modulation. Now, in the decoding it is necessary to separate not only the plane waves with different steering angles, but also the plane waves with different amplitudes. Therefore, the Hadamard matrix of order 4 is used both for the encoding and the decoding processes.

Before doing any of these operations, however, the backscattered signals must be first filtered with a band-pass filter, centred on the transducer central frequency, to remove the second harmonic components of the microbubbles signals, which do not follow the Hadamard decoding process of cancellation and enhancement.

The remaining decoding operations are exactly the same as those previously explained.

Unlike the case without contrast agent, in CEUS it is very crucial the choice of the time interval intervening between two pulses. In fact, it should be big enough to let the microbubbles go back to their equilibrium state. This may therefore imply longer transmission times and, therefore, deeper blind areas.

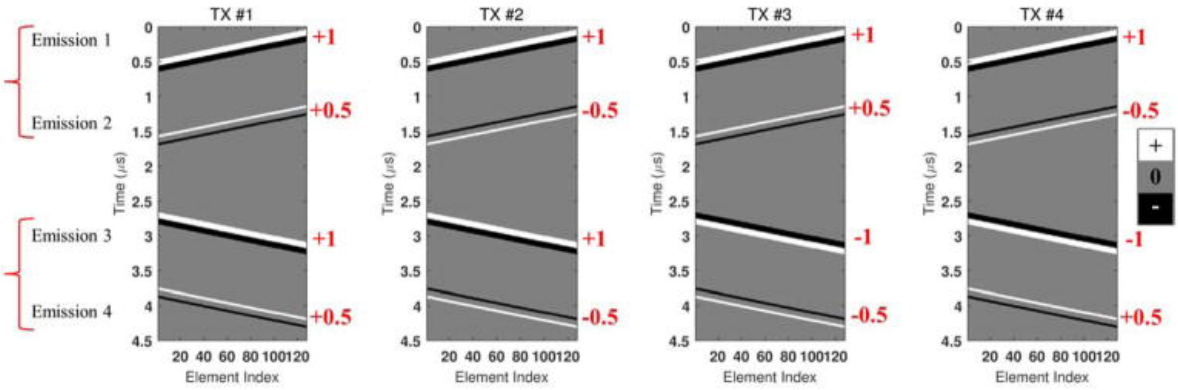

Figure 3.5: Hadamard encoding combined with amplitude modulation [34]

This method strongly depends on the hypothesis that tissues behave differently with respect to microbubbles, namely that their response is only linear. However, this hypothesis doesn't really apply, as non linear terms up to the third order harmonic still fall within the chosen filter bandwidth [35]. These non linearities are all amplified with the Hadamard encoding and may contribute in increasing the clutter artefact, especially in superficial

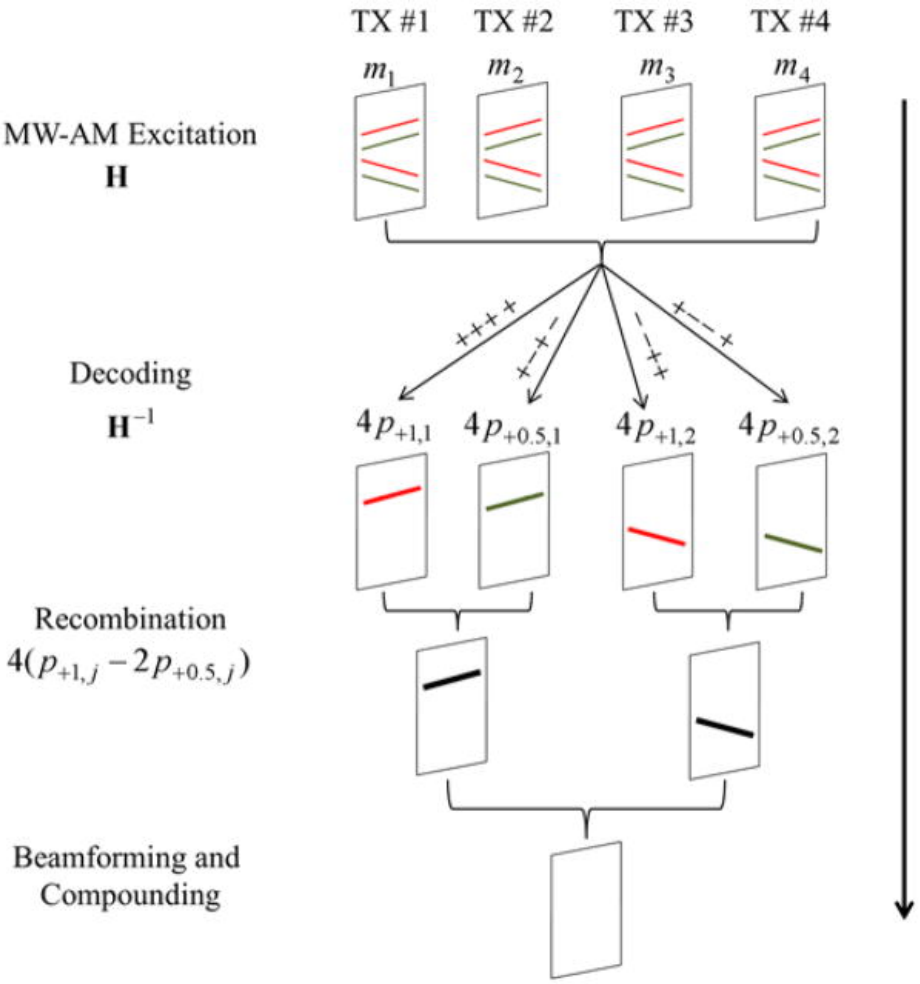

Figure 3.6: Flow of Hadamard decoding operations and coherent compounding to enhance the non linear response [34]

zones, where it predominates over electronic noise. The higher the Hadamard order is, the deeper the image area is, and the more the tissue non linearities are intensified.

Chapter 4

Cascaded Dual-Polarity Waves Imaging

As the previous chapter reported, it is possible to take advantage of each transmission phase to send more than one plane wave, in order to use them to intensify the received signal, as if each transmission was constituted by a single plane with higher amplitudes. The same concept was stretched to its limits in a study by Zhang *et.al.* [27], where another kind of encoding, still based on the Hadamard matrix, is used. In this case, the polarities are assigned to the waves thanks to the construction of a rectangular matrix, with dimensions $(2, M)$, starting from the Hadamard matrix of order 2. If $M = 2$, the encoding here proposed is exactly the same of the MPW method. Instead, if $M = 4$ the differences begin to appear. Before defining the new encoding matrix $C_{2\times4}$, it is necessary to identify other two matrices. The first one is generated by duplicating the Hadamard matrix of order 2 in the following way:

$$C'_{2\times4} = (H_2, H_2) = \begin{pmatrix} +1 & +1 & +1 & +1 \\ \\ +1 & -1 & +1 & -1 \end{pmatrix} \tag{4.1}$$

The second one takes each entry from the Hadamard matrix, from top to bottom and from left to right, arranges them in a row vector and duplicates the latter for the second row:

$$C''_{2\times4} = \begin{pmatrix} a_{11} & a_{21} & a_{12} & a_{22} \\ \\ a_{11} & a_{21} & a_{12} & a_{22} \end{pmatrix} = \begin{pmatrix} +1 & +1 & +1 & -1 \\ \\ +1 & +1 & +1 & -1 \end{pmatrix} \tag{4.2}$$

The final encoding matrix is defined as the element-wise multiplication between the two previously created matrices:

$$C_{2\times4} = C'_{2\times4} .* C''_{2\times4} = \begin{pmatrix} +1 & +1 & +1 & +1 \\ \\ +1 & -1 & +1 & -1 \end{pmatrix} .* \begin{pmatrix} +1 & +1 & +1 & -1 \\ \\ +1 & +1 & +1 & -1 \end{pmatrix} =$$
$$= \begin{pmatrix} +1 & +1 & +1 & -1 \\ \\ +1 & -1 & +1 & +1 \end{pmatrix}$$

The meaning of the columns and the rows is the same already described in Chapter 3, with the only difference that now the matrix is transposed. So the rows here represent the acquisitions $T_{0,1}$, while the columns represent the plane waves sent in each transmission. The columns are intentionally not assigned to each steering angle, as another important difference with respect to the MPW to be noticed is that this matrix applies only to a set of two steering angles α_1 and α_2. So the four columns here are four plane waves sent in a single transmission, but their steering angles are only two. To the first half is assigned α_1, while to the second half α_2:

$$\begin{array}{c} \\ T_0 \\ T_1 \end{array} \begin{array}{c} \begin{array}{cccc} \alpha_1 & \alpha_1 & \alpha_2 & \alpha_2 \end{array} \\ \begin{pmatrix} +1 & +1 & +1 & -1 \\ +1 & -1 & +1 & +1 \end{pmatrix} \end{array}$$

Because of this structure, the method is called cascaded dual-polarity waves (CDW) imaging. For a general number of planes $M = 2^K$, these steps are repeated in an iterative way. For constructing $C''_{2\times2^K}$, it is sufficient to substitute the Hadamard matrix of order 2 with $C_{2\times2^{K-1}}$, which must be conveniently divided into four sectors, to represent respectively the four entries of the Hadamard matrix. Figure 4.1 shows this iterative process, while Figure 4.2 reports some examples of $C_{2\times2^K}$ matrices.

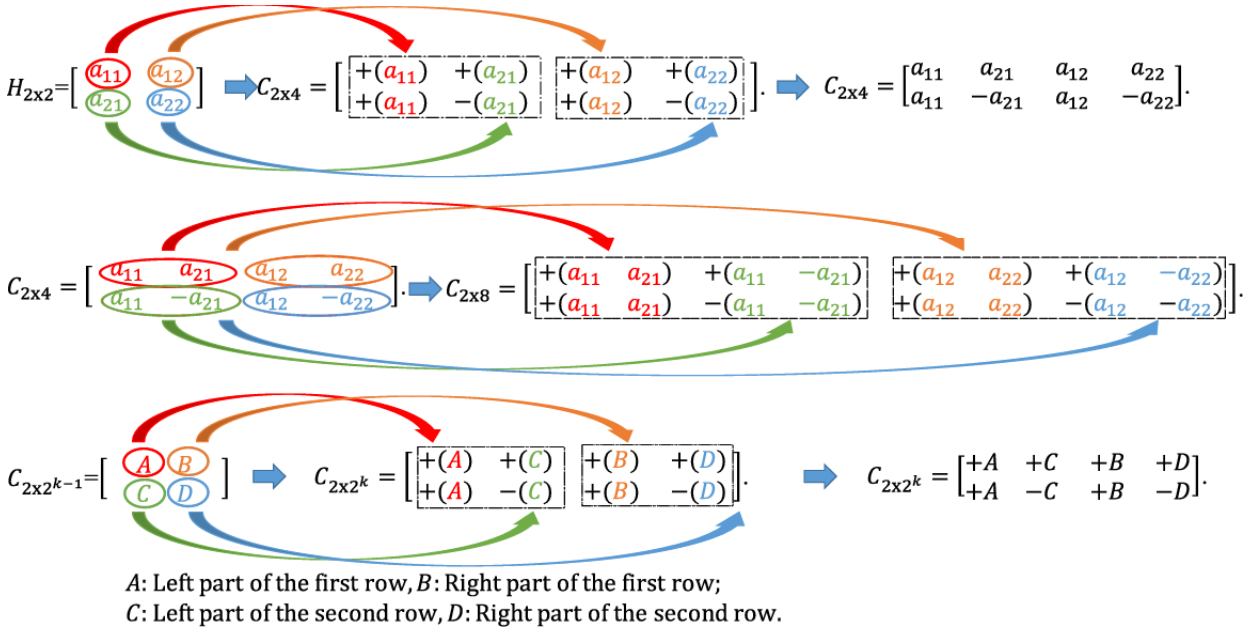

Figure 4.1: Generation of a general $C_{2\times 2^K}$ [27]

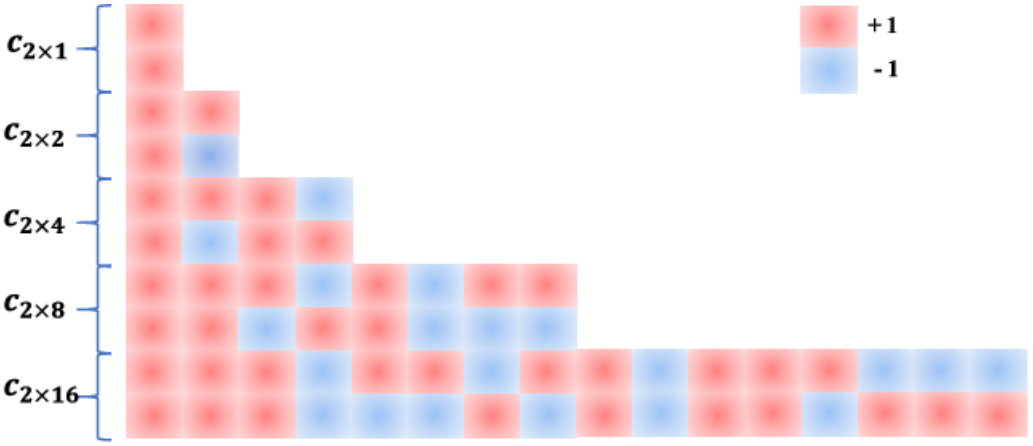

Figure 4.2: $C_{2\times 2^K}$ with $K = 1, 2, 3$ and 4 [27]

Now let's analyse the processing part of this method, using for instance $C_{2\times 4}$.
First, let's define the received signals in the system of equations, as already done in the previous chapter:

$$\begin{cases} y_1(t) = s_{\alpha_1}(t) * h(t) + s_{\alpha_1}(t) * \delta(t-dt) * h(t) + \\ \qquad + s_{\alpha_2}(t) * \delta(t-2dt) * h(t) - s_{\alpha_2}(t) * \delta(t-3dt) * h(t) \\ y_2(t) = s_{\alpha_1}(t) * h(t) - s_{\alpha_1}(t) * \delta(t-dt) * h(t) + \\ \qquad + s_{\alpha_2}(t) * \delta(t-2dt) * h(t) + s_{\alpha_2}(t) * \delta(t-3dt) * h(t) \end{cases} \tag{4.3}$$

The final objective is to separate α_1 and α_2 contributions.
As a first step, the two signals are summed and subtracted:

$$\begin{cases} y_1'(t) = y_1(t) + y_2(t) = 2s_{\alpha_1}(t) * h(t) + 2s_{\alpha_2}(t) * \delta(t - 2dt) * h(t) \\ y_2'(t) = y_1(t) - y_2(t) = 2s_{\alpha_1}(t) * \delta(t - dt) * h(t) - 2s_{\alpha_2}(t) * \delta(t - 3dt) * h(t) \end{cases} \tag{4.4}$$

$y_1'(t)$ contains the contributions with same sign, whereas $y_2'(t)$ contains the contributions with opposite sign. The processed signals now have double amplitude, but in both there are still the two angles. Therefore, at least one other summation and subtraction step is required. As they are now, however, it wouldn't be possible to separate them, due to the delays involved. Thus, beforehand it is necessary to realign the signals, translating the second one by dt:

$$y_2''(t) = y_2'(t + dt) = 2s_{\alpha_1}(t) * h(t) - 2s_{\alpha_2}(t) * \delta(t - 2dt) * h(t) \tag{4.5}$$

Hence,

$$\begin{cases} y_1''(t) = y_1'(t) + y_2''(t) = 4s_{\alpha_1}(t) * h(t) \\ y_2'''(t) = y_1'(t) - y_2''(t) = 4s_{\alpha_2}(t) * \delta(t - 2dt) * h(t) \end{cases} \tag{4.6}$$

Now the two angles contributions are separated, but, before proceeding with compounding, it is necessary to account for the delay in $y_2'''(t)$.
The processing is therefore a sequence of sum/subtract and time delay operations.

To know at each cycle l how much a signal must be translated for a perfect realignment:

$$n * dt = \begin{cases} \frac{M}{2^{(l+1)}} * dt, & 0 < l < L \\ \frac{M}{2} * dt, & l = L \end{cases} \tag{4.7}$$

where, M is the column dimension of the matrix, *i.e.* the number of planes used in each transmission, and $L = \log_2 M$ is the total number of loops necessary to separate α_1 and α_2.

For this last passage, since $l = L$ and $M = 4$, the delay is $2dt$:

$$y_2''''(t) = y_2'''(t + 2dt) = 4s_{\alpha_2}(t) * h(t) \tag{4.8}$$

Eventually, the received signals are exactly those we would obtain with 4-fold amplitude transmissions. Comparing the CDW with the MPW, when only 2 angles are deployed, it is evident that with the same number of transmissions the CDW shows signals with higher amplitudes, thus granting improved image quality.

In Figure 4.3, a self-explanatory example with $C_{2\times 8}$ as encoding matrix is graphically represented to better understand the cycles' operations.

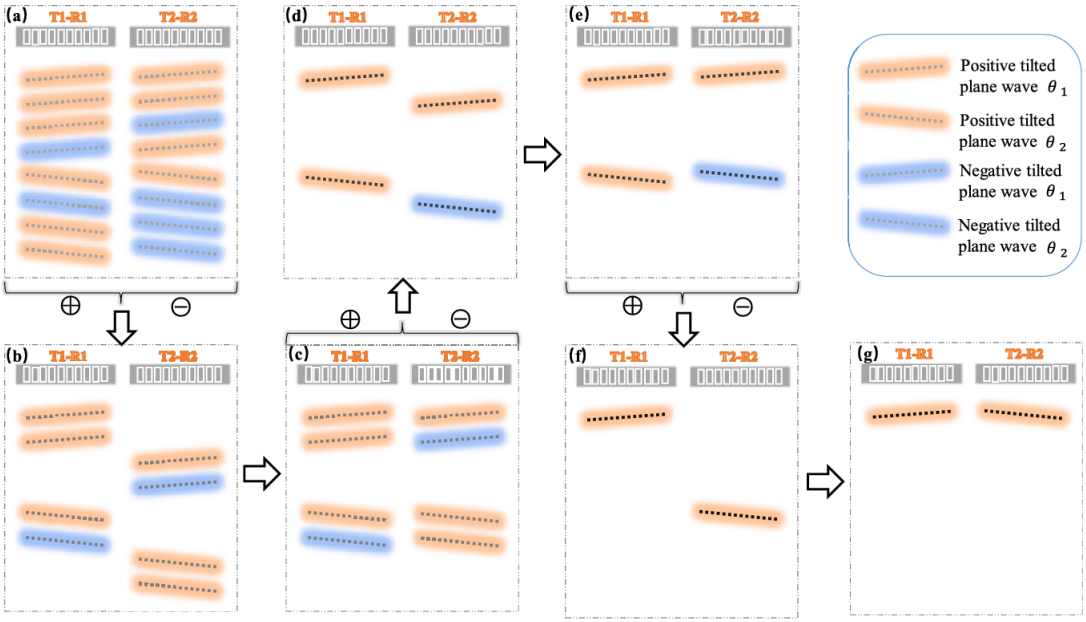

Figure 4.3: Example of application of CDW method with 8 cascaded waves [27]

CDW can be further complexed, to take advantage of the compounding process as well. Namely, it is possible to repeat the same steps with another pair of angles α_i and α_{i+1}.

4.1 Advantages and Limitations

According to the authors, thanks to the CDW, it is possible to increase the SNR with respect to coherent plane wave compounding by $10 \cdot \log_{10} M$, where M is the length of the new rectangular matrix used to assign the +1 and -1 polarities. So, with CDW it is possible to achieve higher SNR, improve the image contrast and increase the penetration depth, even more with respect to MPW, without reducing the frame rate. The axial and lateral resolutions remain similar to the other two methods, but, according to the authors, the variance is smaller.

An important limitation of MPW, that here is finally overcome, is the number of plane waves for each transmission. In the MPW method the Hadamard matrix order must be

a power of 2. For the CDW method this restraint doesn't apply, as any even number of compounding angles can be used. It will only be necessary to remember to generate two transmissions for each pair of angles.

However, for CDW acquisitions, the blind area at the superficial part of the medium becomes larger with respect to the MPW one, as more plane waves are sent in one transmission. Therefore, the higher is M, the deeper goes the blind area, reaching even more than 10 mm.

4.2 Imperfect realignment

Both MPW and CDW results largely depend on the hypothesis of linear behaviour of the medium. However, especially in in vivo situations, the cancellation of contributions during the summation and subtraction operations may be imperfect, due to second harmonic signals generated by non-linear responses. Besides, even though these techniques are thought to reduce motion artefacts, scatterers moving fast enough can be another cause of imperfect cancellation.

4.3 CDW for CEUS

The method proposed by Zhang is relatively recent, and, to the best of my knowledge, the literature doesn't seem to present any application of the CDW in combination with contrast agents. Nevertheless, as CDW is profoundly based on MPW, there might be the possibility of exploring the merging of contrast enhanced ultrasounds with cascaded dual-polarity waves.

Because of the new encoding matrix choice, it is not possible to follow the same directions seen in Chapter 3 to apply this method to CEUS. In fact, if the amplitude modulation is applied in each transmission, by alternating pulses with full and half amplitudes, the decoding process doesn't allow to separate planes with different steering angles and different amplitudes.

However, as previously stated, microbubbles need time to go back to their equilibrium state, in order to be able to provide the non linear response we are looking for. This means that microbubbles shouldn't have memory of what happened to them in the past. Thanks

to this consideration, it may be possible to test CDW with contrast agents, without the need of alternating the pulses' amplitudes in the same transmission. Specifically, it would be sufficient to double the transmissions and to give the duplicates half of the amplitude. Two possible transmission sequences are reported below. Both might be tested to see if they cause any difference in the microbubbles' behaviour. For the second one, in order to perform the decoding, it is necessary however to switch the second and third acquisitions.

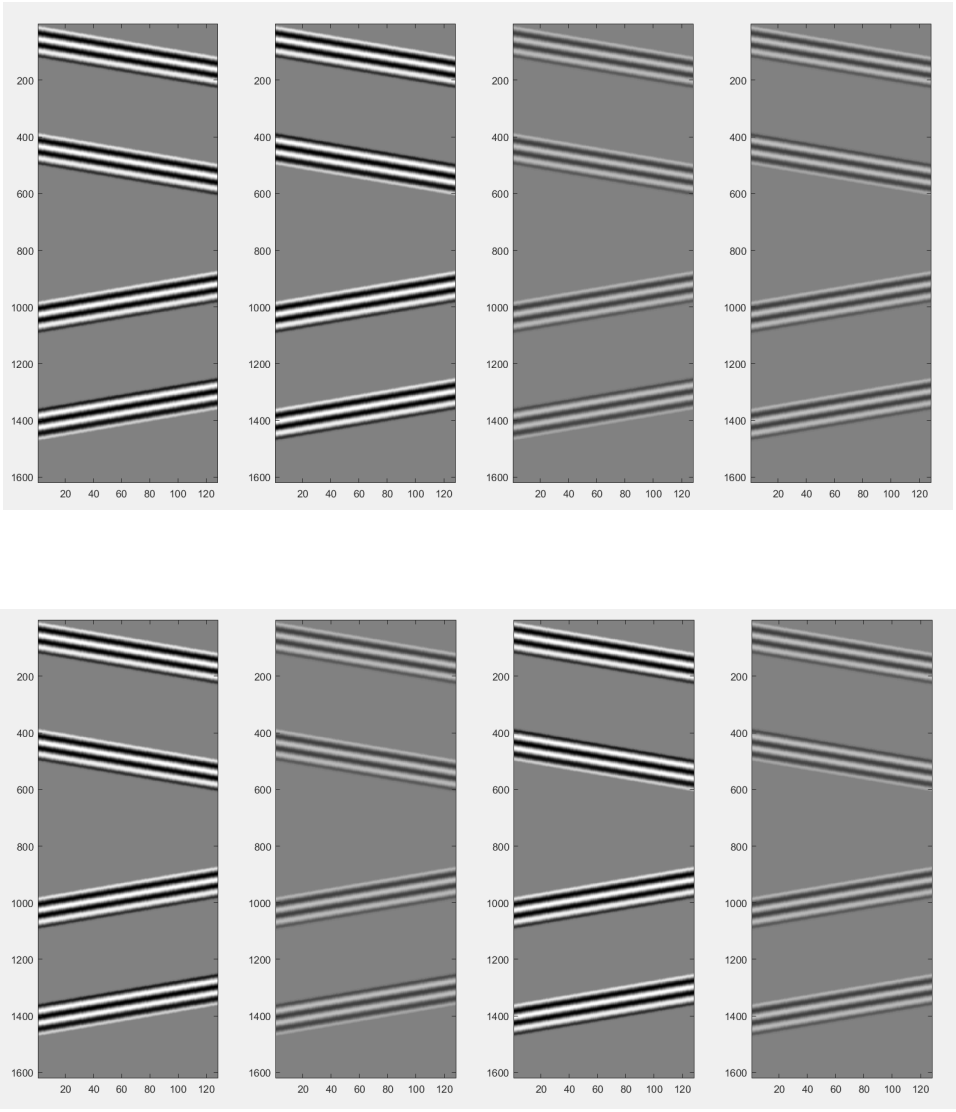

Figure 4.4: Examples of CDW sequence for contrast enhanced ultrasounds

Thanks to CDW it could be possible to increase even more the SNR in deeper zones. However, the same considerations on the choice of the matrix dimension apply here as well. The longer the matrix, the more the clutter artefact is intensified and the deeper the blind area is. This CEUS-CDW technique must be thoroughly tested to study the microbubbles' behaviour to subsequent fast plane transmissions, in order to avoid their disruption.

Chapter 5

Implementation

5.1 Simulations

The methods described in Chapters 2, 3 and 4 were tested using Field II [36] [37], an ultrasound simulator that runs in a Matlab environment. The program provides a number of functions, that allow a wide range of possibilities, from the definition of any possible transducer geometry and apodization, to the choice of the characteristics of the imaging medium.

The simulator works well for linear responses, as it uses linear systems to compute the pressure fields for pulsed or continuous waves. Field II is, therefore, not suggested to study microbubbles' non-linear behaviour.

Furthermore, the author recommends using as sampling frequency 100 MHz, which is smaller than the usual few GHz used to reconstruct all the discontinuities of the spatial impulse response, but it allows to preserve its energy. Nevertheless, as beamforming is performed in these simulations, using high sampling frequencies increases the computational time to several hours rather than few seconds. Therefore, after the acquisition and before beamforming, it is necessary to resample the received data with a frequency equal to four times the central frequency of the transducer, which still allows to respect the Nyquist-Shannon theorem for the reconstruction of signals.

5.1.1 Script organization

The script is organized into the following sections:

1. Field II and variables initialization;
2. Transducers definition in terms of geometry of the array, number of elements, central frequency, apodization and impulse response for both the transmitting and receiving apertures;
3. Definition of the transmitting sequence, *i.e.* the number of plane waves and their polarities, the number of steering angles and the step in between, and the time intervening each pulse;
4. Medium definition in terms of number, position and amplitude of the scattering points;
5. Calculation of the pressure fields, whose computational load depends on the number of scattering points defined;
6. Decoding (only for MPW and CDW);
7. Beamforming;
8. Coherent compounding;
9. Hilbert transform to obtain the envelope, logarithmic compression and image display.

It is now worth explaining more in details the choices adopted for some of these steps. All the three methods have been tested with both 2 and 4 steering angles. For the first case, 2° and -2° were deployed, whereas, for the second case, 6°, 2°, -2° and -6° were used. Furthermore, to test the effective improvement of the CDW method compared to MPW, the encoding matrices were chosen in order to obtain theoretically higher SNR with CDW. Namely, with two steering angles, the matrices with lengths 4 and 8 ($C_{2\times4}$, $C_{2\times8}$) were chosen, while with four steering angles, only $C_{2\times8}$ was used, since a longer matrix would have required very long computational times, *i.e.* more than a day.
In the following figures all the plane waves sequences, with respective encoding, are shown for each transmission.

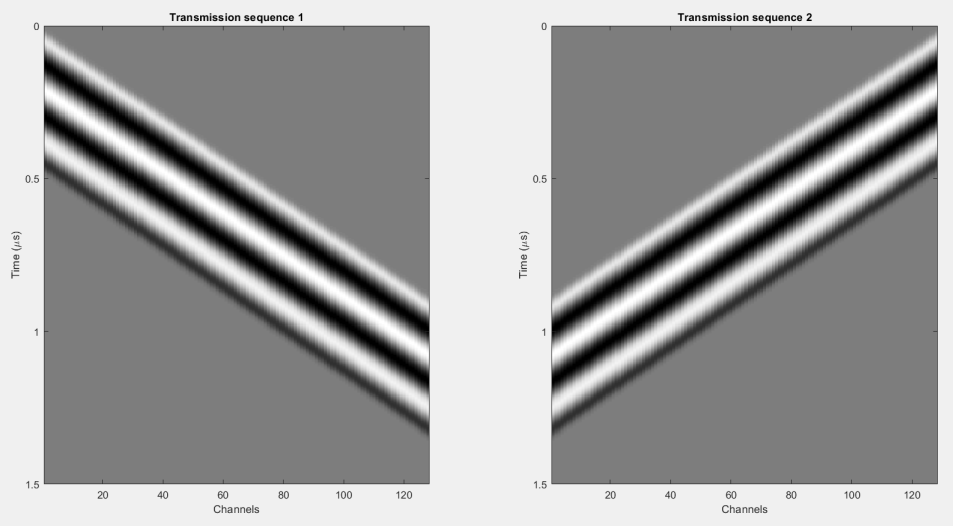

Figure 5.1: CPWC transmissions with 2 angles (2° and -2°)

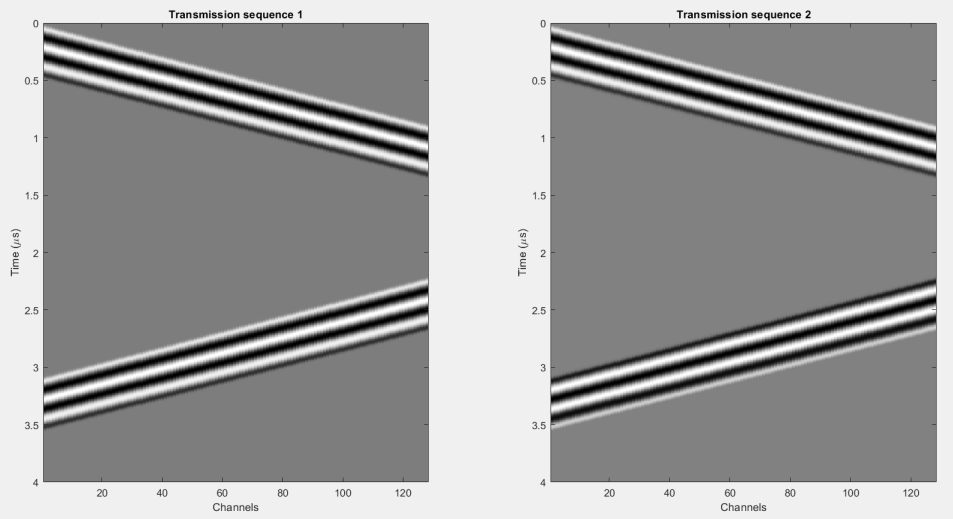

Figure 5.2: MPW transmissions with 2 angles (2° and -2°)

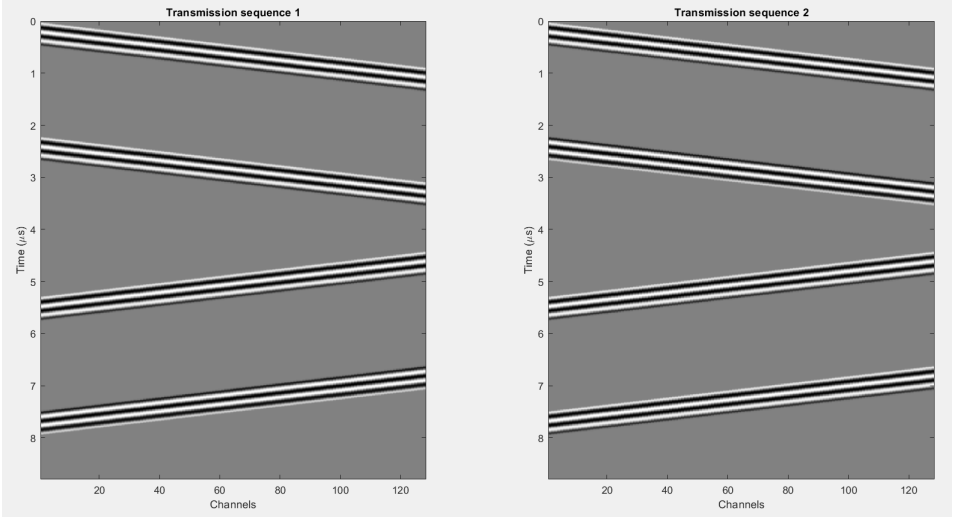

Figure 5.3: CDW transmissions with 2 angles (2° and -2°) and encoding matrix $C_{2\times4}$

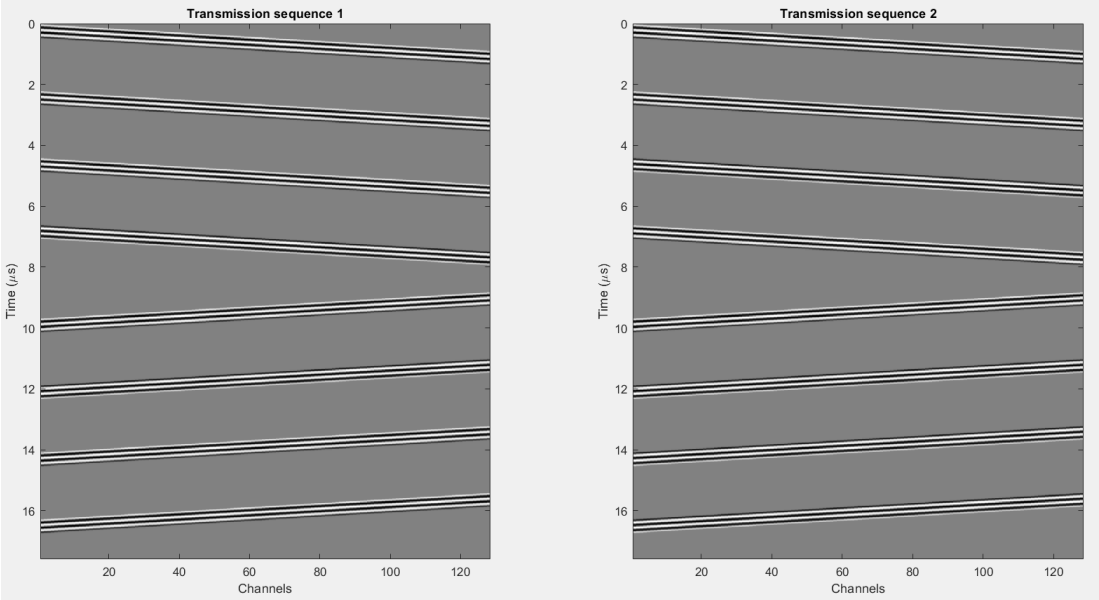

Figure 5.4: CDW transmissions with 2 angles (2° and -2°) and encoding matrix $C_{2\times8}$

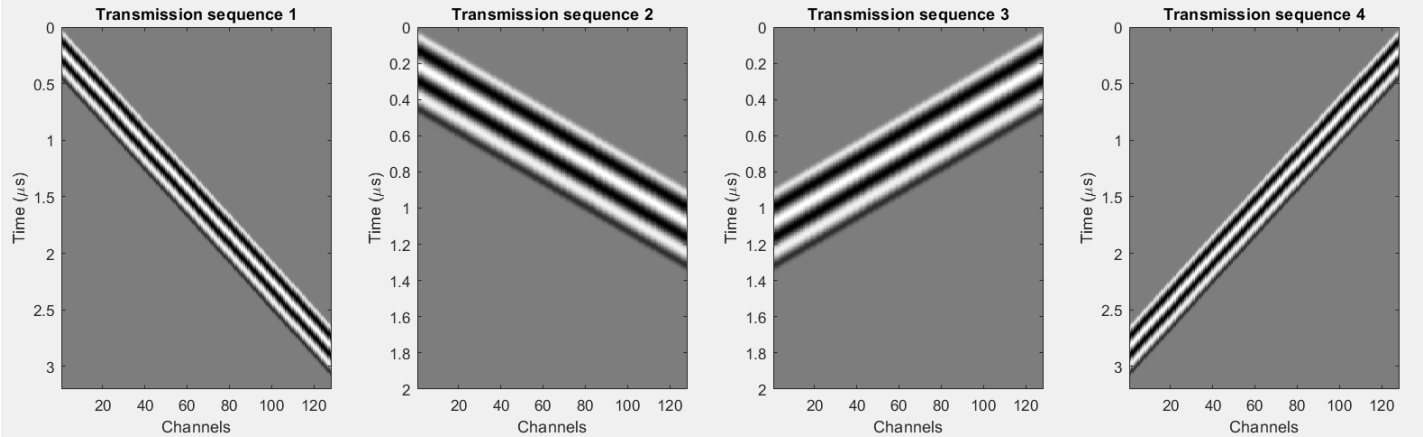

Figure 5.5: CPWC transmissions with 4 angles (6°, 2°, -2° and -6°)

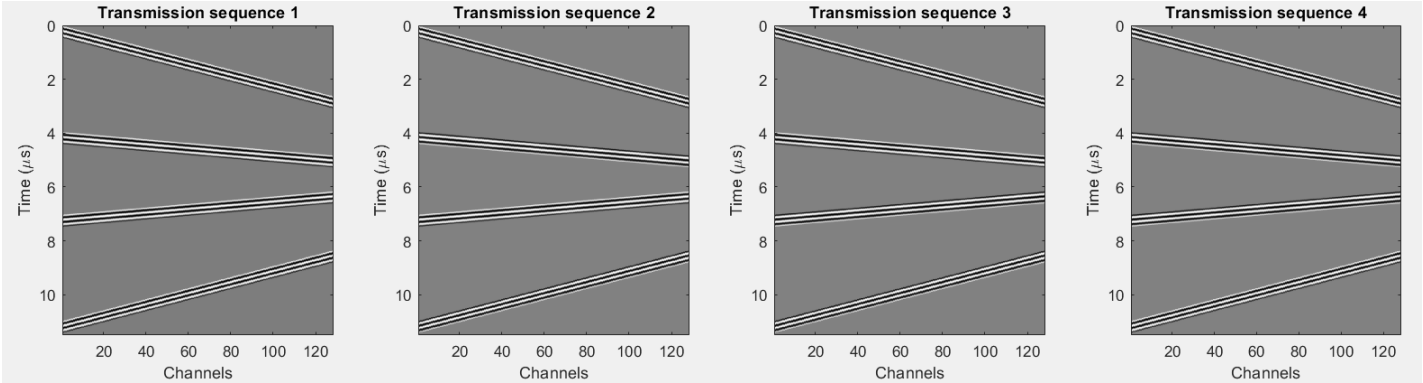

Figure 5.6: MPW transmissions with 4 angles (6°, 2°, -2° and -6°)

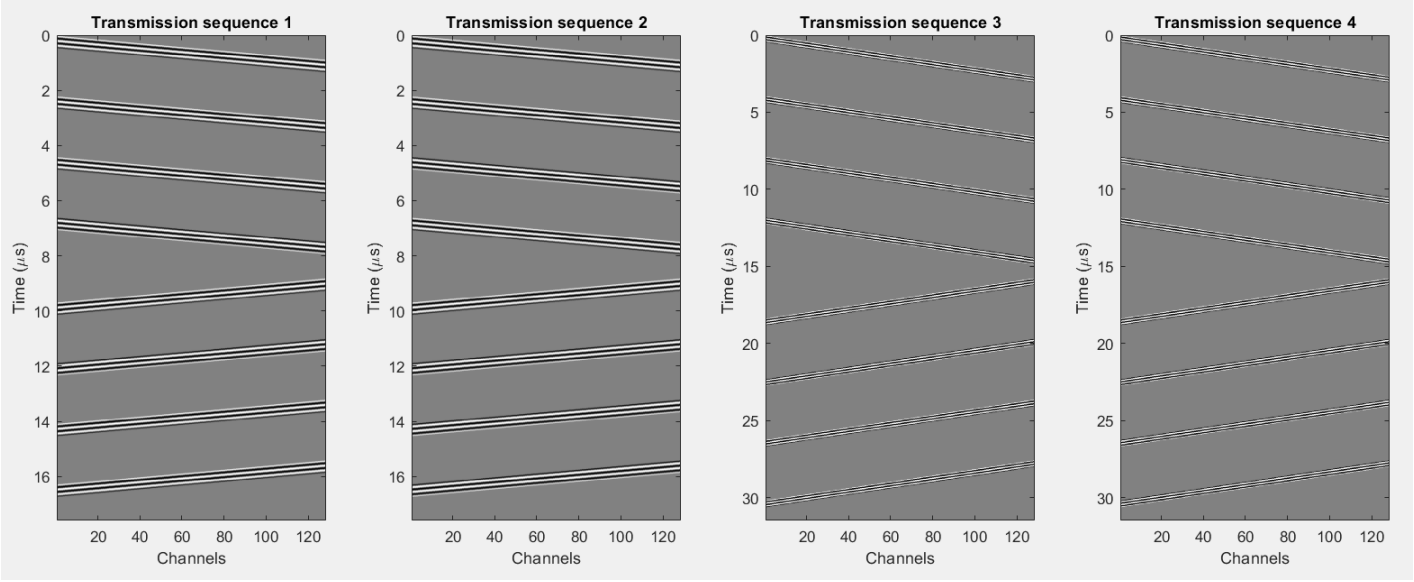

Figure 5.7: CDW transmissions with 4 angles (6°, 2°, -2° and -6°) and encoding matrix $C_{2\times8}$

The transducers geometry was defined following the dimensions of an L11-4v probe with 128 elements. The apodization for the transmitting aperture was set using a tukey window to reduce the wave edge effect, which is caused by the absence of infinite elements to generate a plane wave.

The chosen media start at a depth different from 0 cm, to take into account the presence of the blind zone. In fact, Field II doesn't behave well if scattering points are defined in the blind area. The program provides as outputs not only the signals received by the transducers, but also the time at which the first sample was acquired. Since, however, it bases its calculations on the scattering points positions, without knowing that the transmission hasn't finished yet, the time provided can be negative, thus causing problems in the beamforming process.

Two different media have been used for testing the three methods. One is an array of strong reflectors in vertical and horizontal directions, used to perform calculations on the spatial resolution. The other is a vertical line of 6 mm diameter cysts, in presence of tissue attenuation (-0.5 dB/cm/MHz) and with gaussian noise added, to simulate electronic noise. This medium was used to assess the progressive improvement of SNR and contrast from CPWC to CDW.

Finally, for the beamforming process, two arrays were defined: a 2D one and a 3D one. They both have same row and column dimensions, as these represent all the pixels of the image that we want to reconstruct. The 2D array was used to define for each pixel the

time necessary for a plane wave to get to it, calculated as seen in (2.6). The 3D array third dimension is equal to the number of elements of the probe, bacause, in fact, this array reports the time requested for an echo to get from each pixel to each element of the transducer. This time is computed as seen in (2.2). From the 3D array, only the entries included in the aperture are then considered in the computation of the total propagation time.

Further details can be found in the Appendix, where all the scripts produced for Field II are reported.

5.1.2 Results

Wires

The first set of images is the one with an array of wires, reported in Figures 5.8 and 5.9.

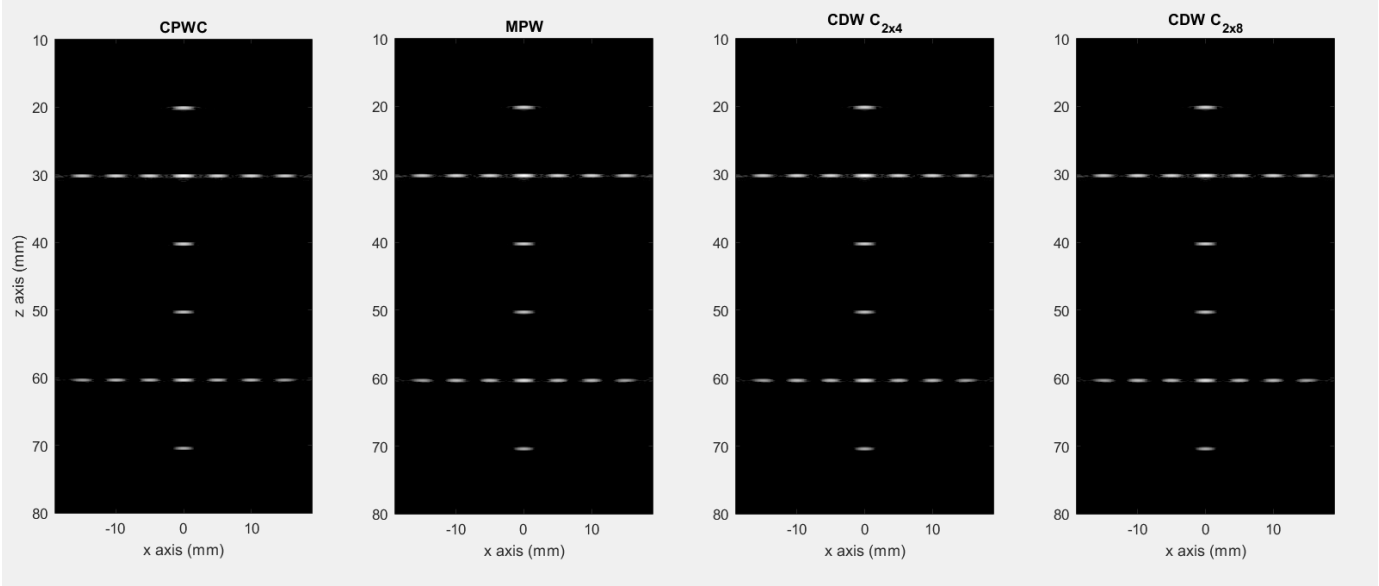

Figure 5.8: Simulation of wires with 2 steering angles

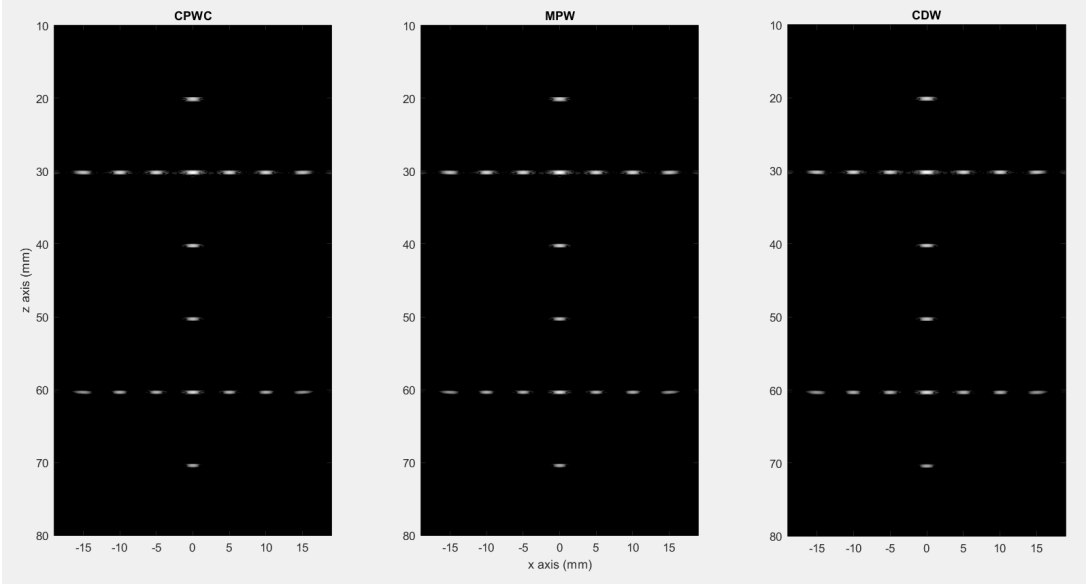

Figure 5.9: Simulation of wires with 4 steering angles

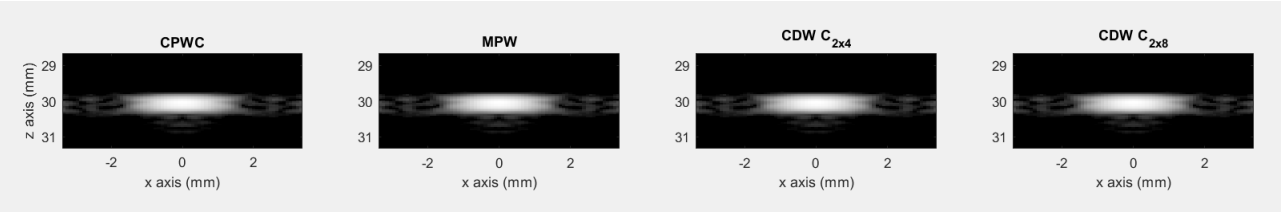

Figure 5.10: Detail of a scatterer in the 2 angles case

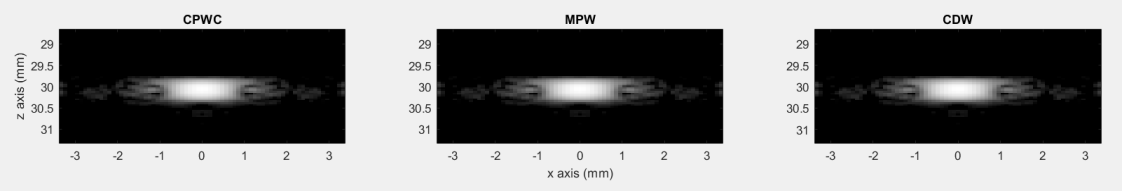

Figure 5.11: Detail of a scatterer in the 4 angles case

First off, it is possible to notice the effect of increasing number of steering angles on the image quality. In fact, the points in Figure 5.11 result much less spread out with respect to those in Figure 5.10. To give a more quantitative measure in terms of spatial resolution, the point spread functions for the scatterers, in the position at azimuth 0 mm and depth 30 mm, are represented in Figures 5.12 and 5.13, for the lateral direction, and Figures 5.14 and 5.15, for the axial direction.

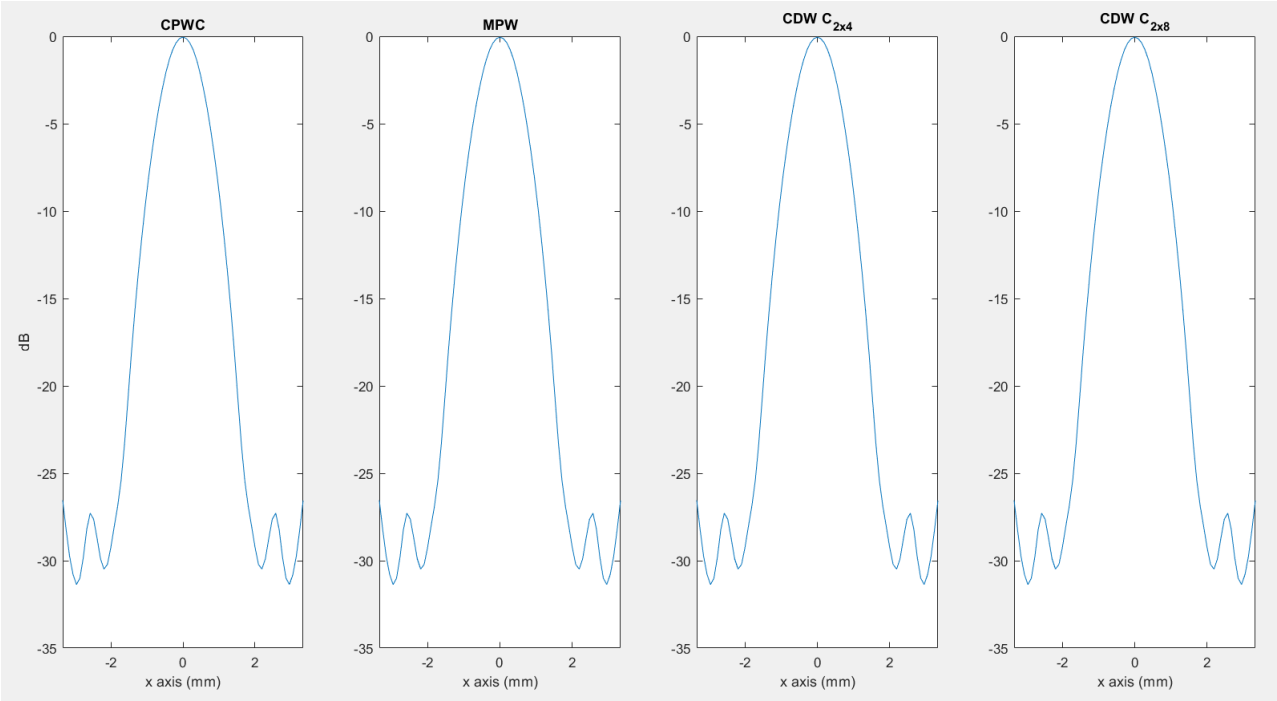

Figure 5.12: Point Spread Functions in the horizontal direction for the 2 angles case

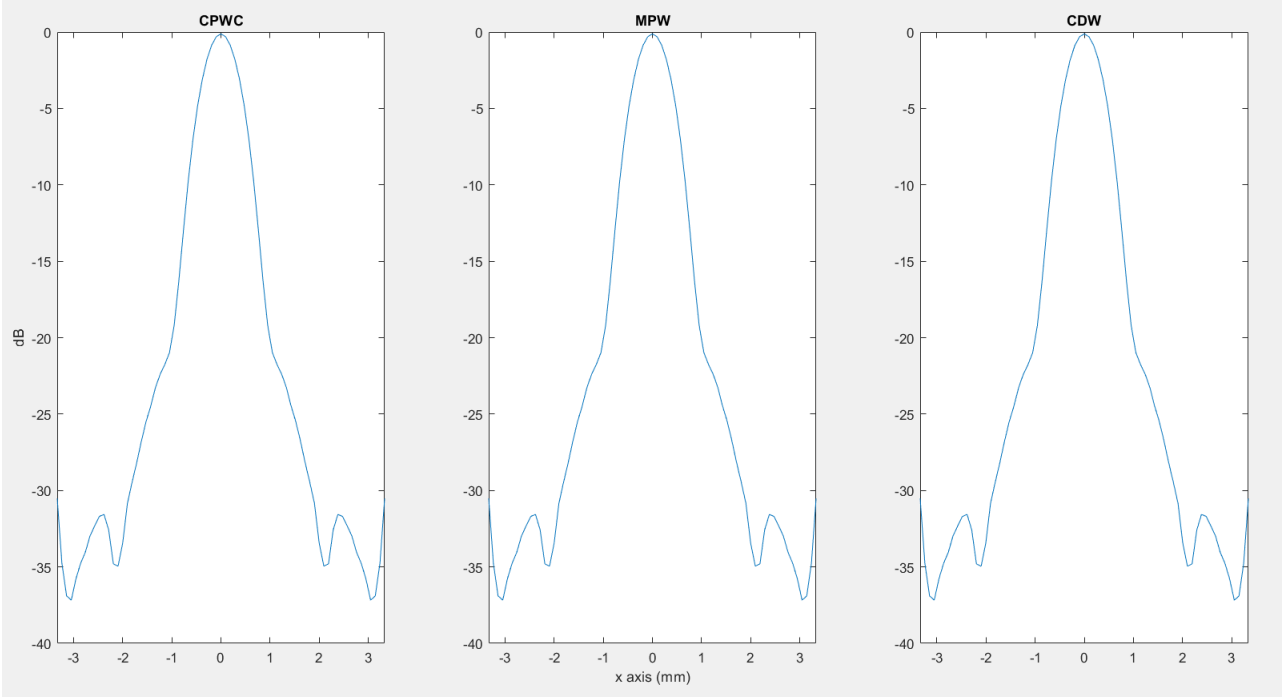

Figure 5.13: Point Spread Functions in the horizontal direction for the 4 angles case

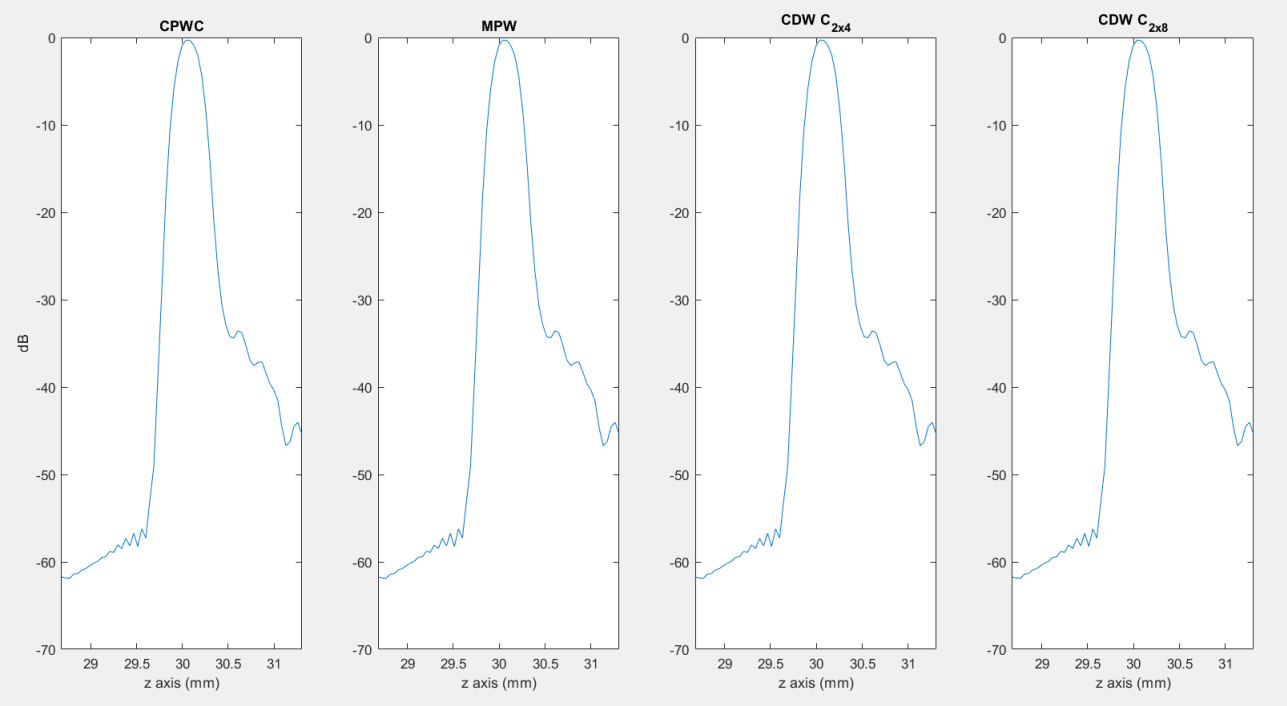

Figure 5.14: Point Spread Functions in the vertical direction for the 2 angles case

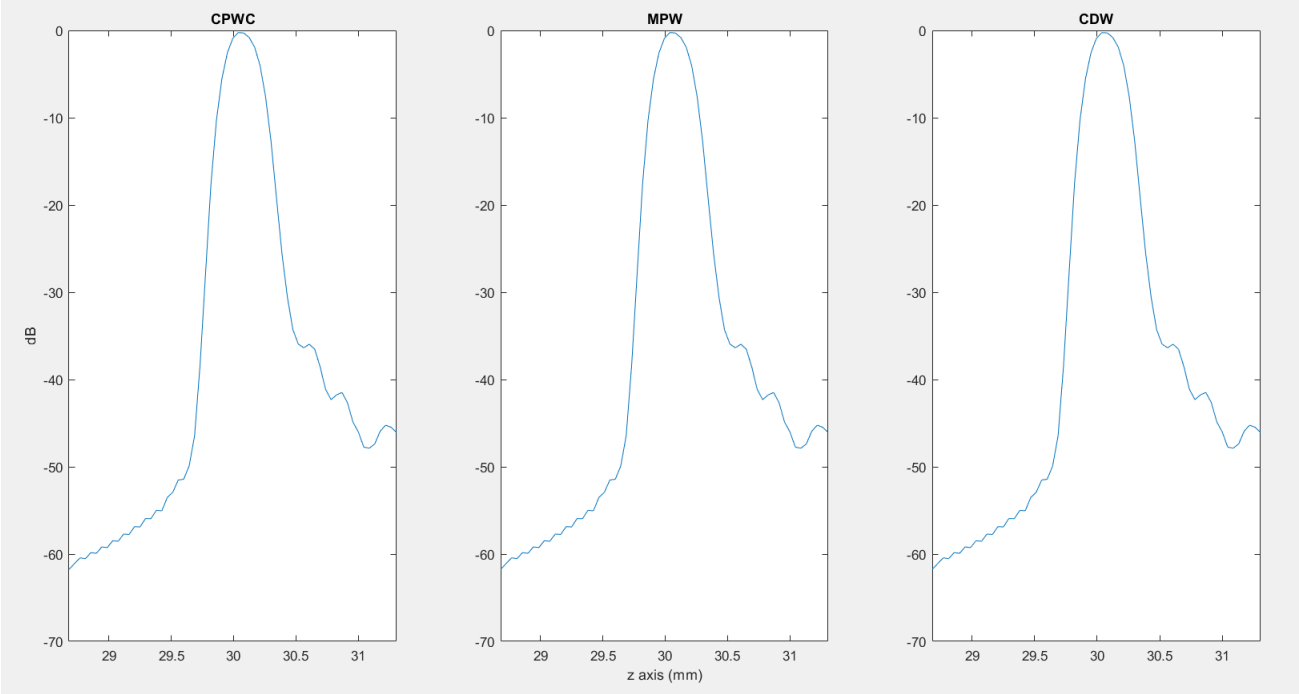

Figure 5.15: Point Spread Functions in the vertical direction for the 4 angles case

The spatial resolution can be computed as the full width at half maximum of the point spread functions (conventionally around -10 dB). It is immediate, therefore, that the lateral resolution improves in the case of four compounding angles, whereas the axial resolution slightly increases.
Another important aspect to be noticed is that, considering separately the two cases of different number of compounding angles, the three methods provide the same point spread function, meaning, therefore, that the resolution is the same in all the three methods. In the following table the spatial resolution values computed for the simulations are reported.

	Lateral resolution	Axial resolution
2 angles	2.124 mm	0.399 mm
4 angles	1.346 mm	0.412 mm

Table 5.1: Spatial resolution values

Finally, it is worth noticing that, in the axial point spread functions, there is a slight positive slope on the right, due to reverberation effects, which are caused by the use of strong reflectors.

Cysts

The second set of images presents higher complexity. Nevertheless, as shown in Figures 5.16 and 5.17, the three methods were all able to reconstruct the medium, with an increase in the intensity values from CPWC to CDW.

It is visually immediate the improvement: cysts in depth become more and more visible observing the figures from left to right. As for the resolution, here there is also the necessity of performing quantitative measurements. This was achieved thanks to two parameters: SNR and contrast.
The first was computed considering ROIs of dimension 10x10 pixels, along the central vertical axis of the images, in order to observe the behaviour at different depths and to include the cysts in the computation. The SNR was calculated using the formula:

$$SNR = 20 \log_{10} \frac{\mu_s}{\sigma_n} \tag{5.1}$$

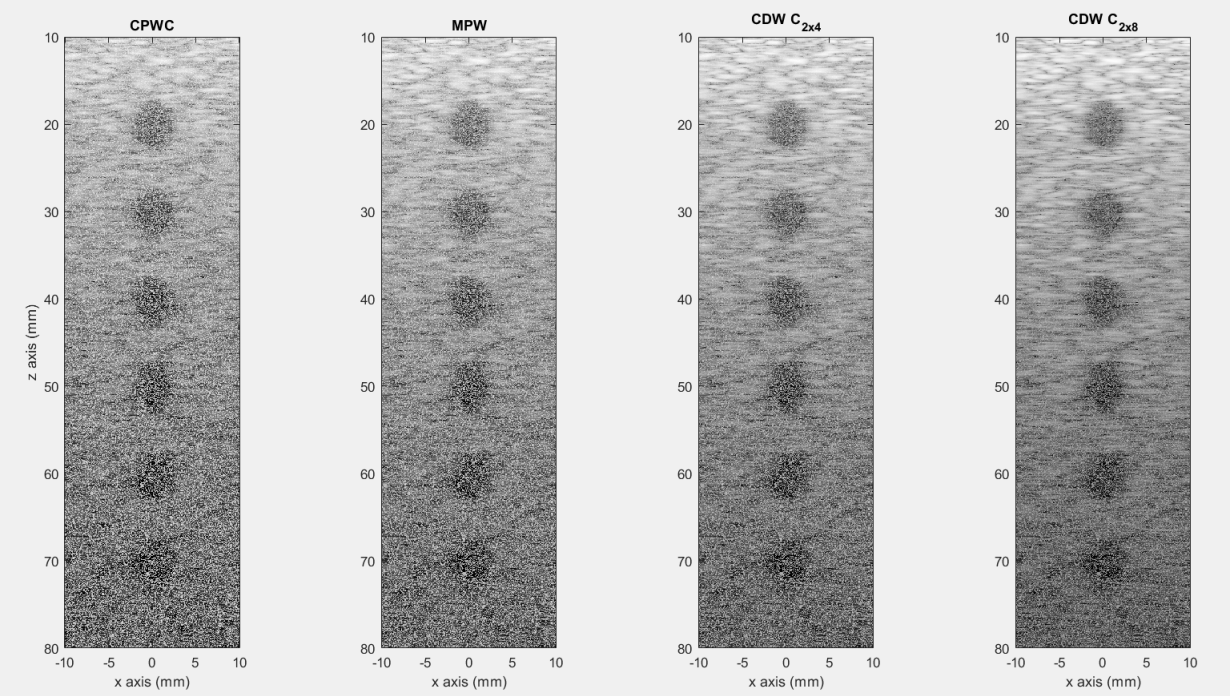

Figure 5.16: Reconstruction of cysts for the 2 angles case

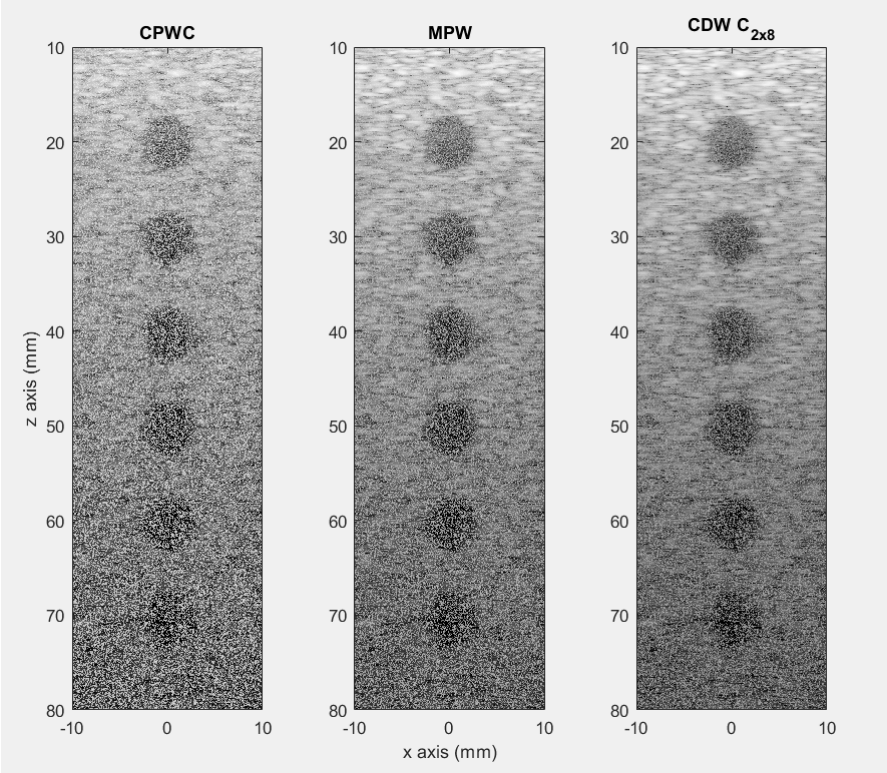

Figure 5.17: Reconstruction of cysts for the 4 angles case

where,

μ_s is the mean of the signal

σ_n is the standard deviation of the noise

The results are represented in Figures 5.18 and 5.19.

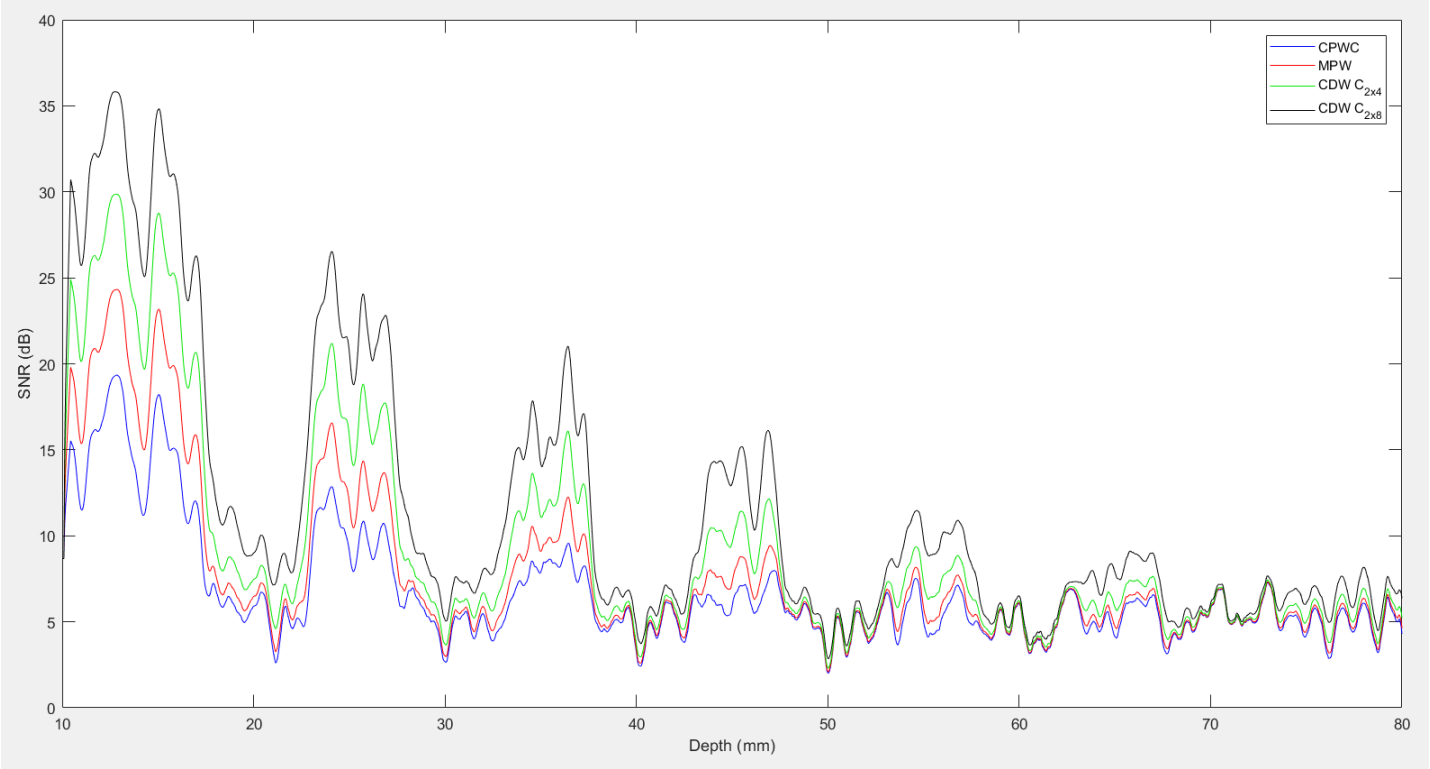

Figure 5.18: SNR as a function of depth for 2 angles with four different transmission sequences

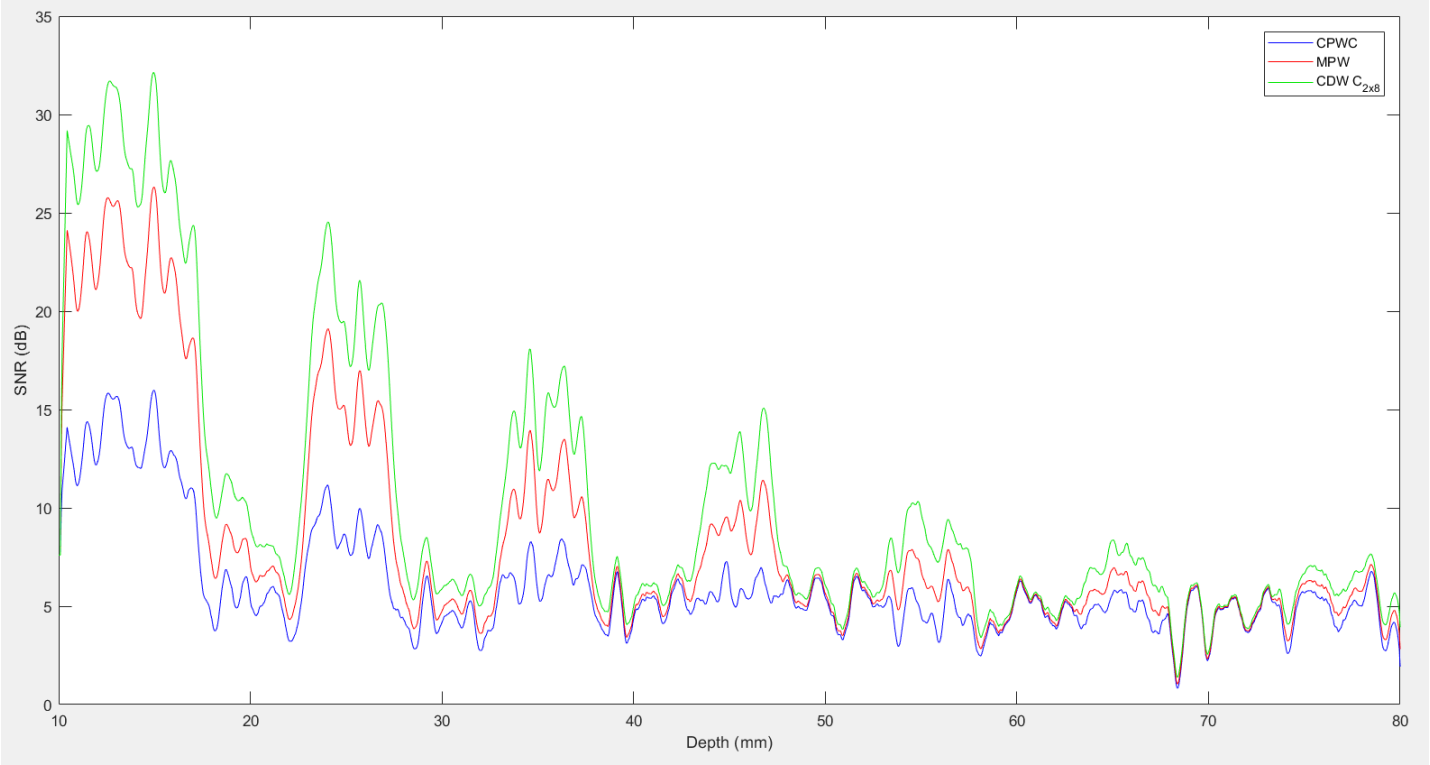

Figure 5.19: SNR as a function of depth for 4 angles with three different transmission sequences

In both cases it is possible to observe an increment in SNR from CPWC to MPW and even more in CDW. In fact, as already stated, the SNR should increase if the number of planes in a single transmission increases. Specifically, according to theory, the SNR increases by $10\log_{10} N$, where N is the number of plane waves in a single transmission. Therefore, the expected increments with respect to the CPWC method are:

	MPW	CDW ($C_{2\times4}$)	CDW ($C_{2\times8}$)
2 angles	3 dB	6 dB	9 dB
4 angles	6 dB	-	9 dB

Table 5.2: Theoretical SNR increment

The simulated results are indeed similar to the predictions, around the third inclusion, which is positioned at 50 mm in depth.
Thanks to this behaviour, it is also possible to prove that the penetration depth, that can be defined as the point at which the SNR falls down 6 dB, increases from CPWC to CDW.

Similarly, it can be noticed that the contrast increases from CPWC to CDW. This second parameter was computed considering four ROIs in total for each image: one for the cyst and one for the background near the same cyst, at two different depths. The following definition was applied to calculate the contrast:

$$CNR = |\mu_{background} - \mu_{cyst}| \tag{5.2}$$

where,

$\mu_{background}$ is the mean of the intensity values, already logarithmically compressed, included in the background ROI

μ_{cyst} is the mean of the intensity values, already logarithmically compressed, included in the cyst ROI

The results are reported in Figures 5.20 and 5.21, and it can be noticed, in fact, a progressive increment of the contrast.

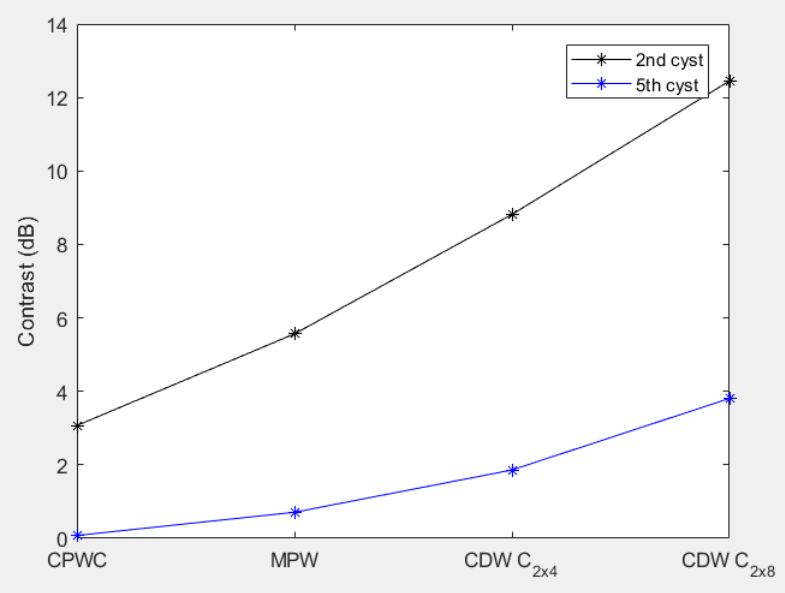

Figure 5.20: Contrast values for 2 angles: the black line represents a more superficial zone (2nd cyst depth), whereas the blue line refers to a deeper zone (5th cyst depth)

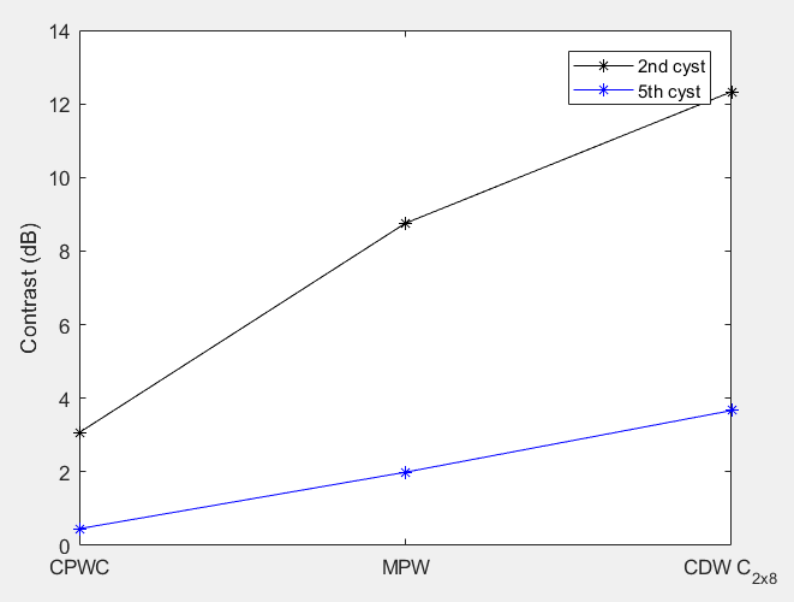

Figure 5.21: Contrast values for 4 angles

Nevertheless, as the simulated medium and noise still didn't reflect a real situation, the following step was to compare the three methods with a real ultrasound system on standard phantoms, namely the GAMMEX Ultrasound 403GS LE Grey Scale Precision Phantom, to asses effectively the parameters improvement, as well as to test the techniques with microbubbles.

5.2 Acquisitions

The acquisitions were performed using the Versonics Vantage system (Verasonics, Kirkland, WA), and the probe used was the L11-4v, with 128 channels and central frequency equal to 6.25 MHz.

Before using a real phantom, some tests were performed to assess the quality of the transmission, thanks to an hydrophone, which is a needle that has on its tip a very small piezoelectric transducer. The following photos show the setup used.

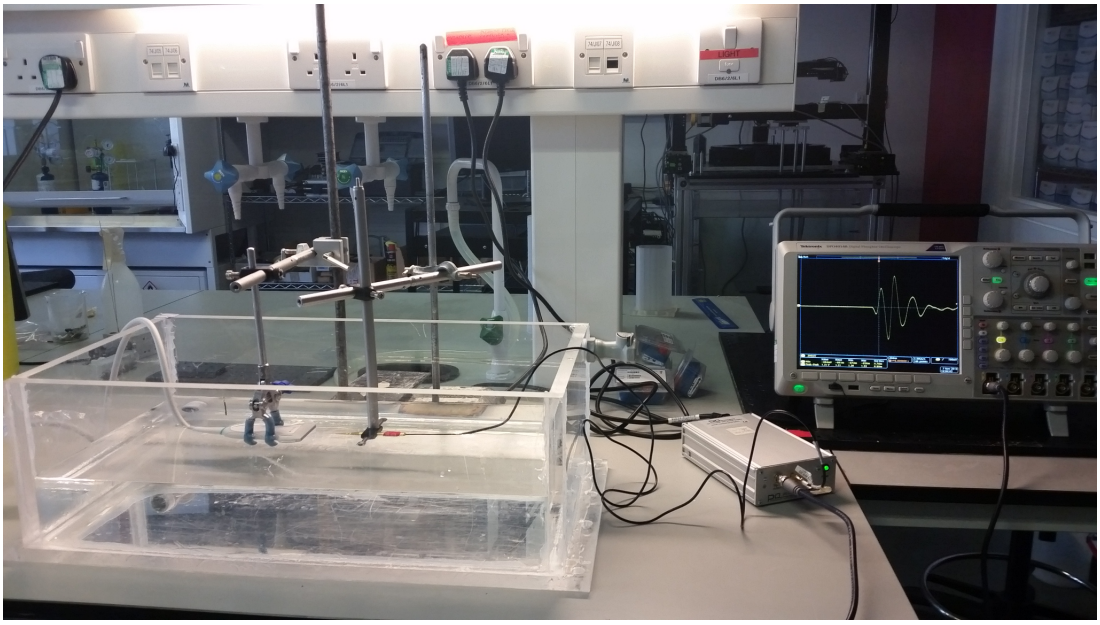

Figure 5.22: Overall setup

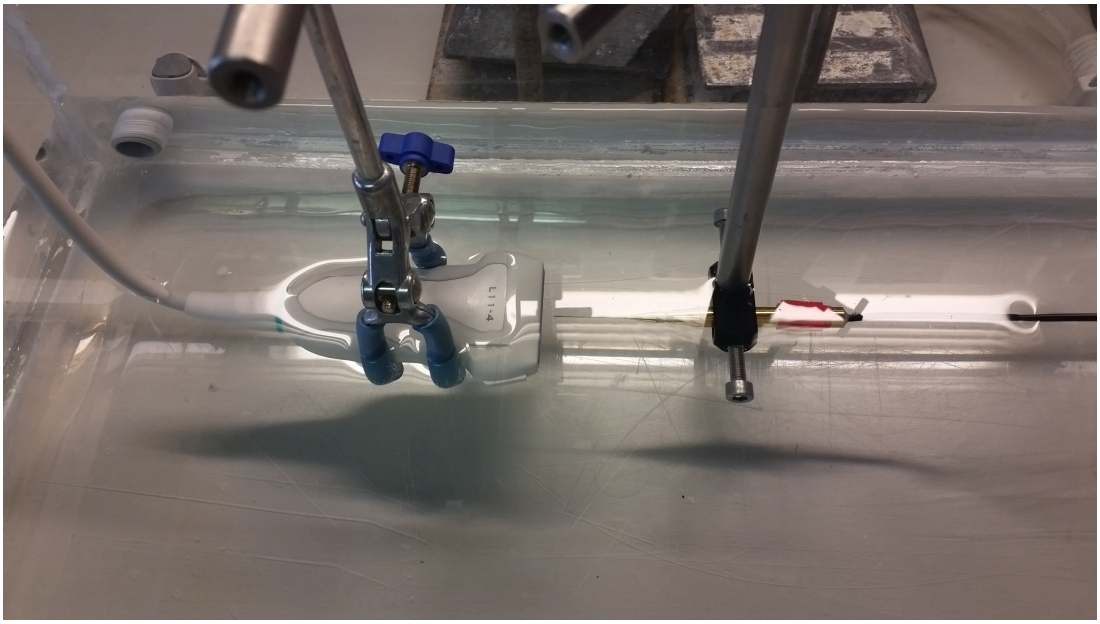

Figure 5.23: Water tank with the instrumentation

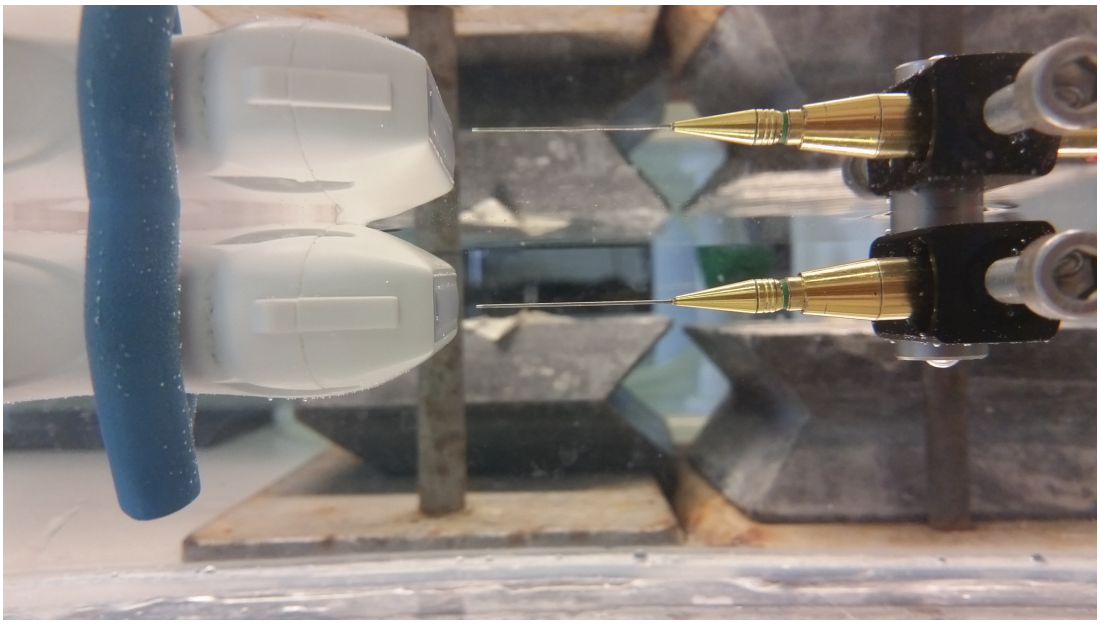

Figure 5.24: Probe and hydrophone

In the first photo, on the left, there is the tank filled with water and the probe and hydrophone already submerged, but still near the surface. The hydrophone includes a pre-amplifier, and it is then connected to an amplifier, which is the silver box near the center of the photo. Finally, an oscilloscope can be noticed on the right. This is used to observe the shape and amplitude of the pressure fields generated by the transmitted waveforms.
The wave that can be seen displayed on the oscilloscope was generated using one of the Vantage software built in functions, in order to verify the correct positioning of all the elements of the setup.
To generate the waves, three scripts, one for each method, were first prepared to save all the structures needed by the software to launch the transmissions. In particular, the TW (Transmit Waveforms) structure was set in order to respect the specifications shown in Figures 5.5, 5.6 and 5.7 and also to test a frame rate equal to 2000 Hz. Since each channel is supposed to deliver different waveforms, because of both polarities and delays, a PulseCode generator was used for customizing the waves as preferred.
Before passing to the actual acquisition with the hardware, Vantage software gives also the possibility of using the SimulateMode, in order to test the script and the structures generated beforehand.
Even though the simulations were perfectly functioning and the processing, performed in a second moment as these methods are not real time (see Chapter 6), was giving similar results to those seen with Field II, the actual experiments did not allow to observe any

pressure field with the hydrophone. Since with other transmission sequences it was possible to observe some waves, the issue was supposed to be related to the fact that each channel has now to transmit a different waveform, which is actually a combination of all the plane waves.

To identify the problem, another setup was used, this time with motors to move in a very precise way the hydrophone below the transducer array, to detect each channel transmission. Also, the script was revised in order to isolate one channel and to observe only its generated wave. In this way it was finally possible to observe the desired transmission.

Therefore, a debugging phase came soon after, to spot the differences in the scripts.

Unexpectedly, the program run by Vantage, when in HardwareMode, tries to use a provided function called computeTWwaveform, even though a TW structure already exists, and it was, in fact, generated with the same function. It is worth noticing that the computeTWwaveform function had previously reported an error in SimulateMode, related to the length of the signals, which was actually not supposed to appear. The Verasonics technical support was, in fact, contacted, the error was promptly corrected and a new function was therefore used, allowing eventually SimulateMode to work. However, there is still the necessity to contact again the technical support to correct what happens when the function is called for a second time in HardwareMode. Simply removing the call to the function doesn't seem to be working. In fact, this step is necessary to read and elaborate the PulseCode present in the TW structure. Nevertheless, while reading the TW structure, some alterations are made to it. The most crucial one is supposedly related to the field called States, which loses in the passage the total number of channels used, which is 128. No real acquisitions were therefore performed, as the technical support must be contacted for a second time, in order to solve the problem related to the function.

Chapter 6

Conclusions and Future Developments

The three described methods represent a revolution in ultrasound imaging. Thanks to the development of parallel computing, they allow to increase the frame rate without compromising the image quality. Furthermore, the MPW and CDW methods may be considered an extension of CPWC, as they keep the same high frame rate, while improving both SNR and contrast. To achieve this, MPW and CDW use multiple plane waves in a single transmission for mimicking the exploitation of higher voltages, without actually damaging neither the transducers nor the medium. However, since their transmission times are longer, especially in the CDW case, the superficial zone can not be perceived. Therefore, they are surely a valid alternative over traditional ultrasound imaging techniques for bigger penetration depths, while they are not recommended for shallow structures.

In all the three methods, the use of simple sums, differences and time delays allows to avoid any extra loading on the software signal elaboration. This doesn't mean, however, that the overall computational cost is low. In fact, these techniques can not be considered real-time, especially due to the beamforming process, which may require up to few seconds, depending on the number of pixels to be reconstructed, the length of the received signals and the computational capabilities of the system deployed.
Another clear disadvantage of these techniques is the necessity of using numerous plane waves for the compounding process. As demonstrated in Chapter 2, it is possible to restore the quality of an image obtained with coherent plane wave compounding to that of a

conventional linear scan, only using a large number of angles for the compounding process. However, increasing the number of tilted planes may not always be the right solution. In fact, while the image appearance improves, the maximum achievable frame rate decreases and fast motion might actually degrade the image quality.

The following aims at describing possible solutions to speed up the proposed imaging methods, first, in terms of reducing the number of tilted planes and, second, in terms of time requested for the beamforming process.

6.1 Reduction of the number of tilted planes

Several studies tried solving the conflict between reduced number of plane waves and image quality. The general objective seems to be the necessity of reducing the clutter artefact, which is generated by off-axis transmissions and/or echoes, as well as by random electronic or acoustic noise [38]. Due to the absence of a focus, in plane wave imaging one of the main sources of clutter is the presence of higher sidelobes, which cause power leakages and mask weak scatterers. A simulation of the point spread function for both linear scan and plane wave imaging is reported in Figure 6.1.

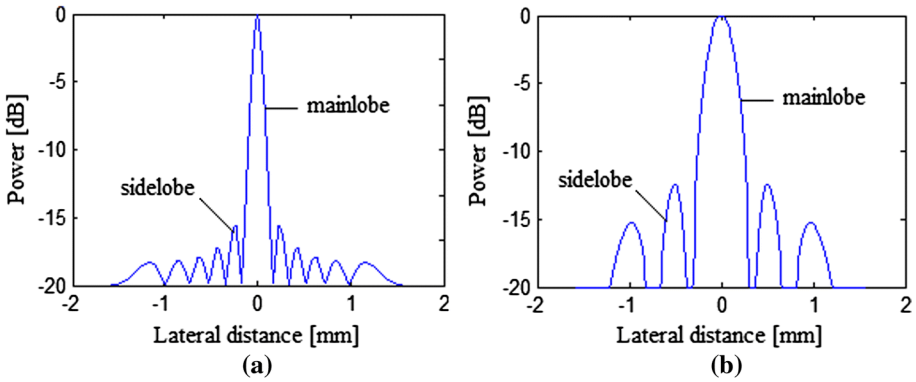

Figure 6.1: PSF for (a) linear scanning and (b) plane wave imaging [39]

Among the disparate possibilities to reduce the sidelobes' levels, a very simple one is to use apodization, which consists in applying a window to the receiving apertures [40]. Traditional types of windows used for reducing the sidelobes are the Hamming and Hanning windows, which, however, degrade the shape of the mainlobe and, thus, worsen the lateral resolution. Furthermore, they don't consider the attenuation factor brought about

by different depths and they apply equally to various types of images, independently of the subjects.

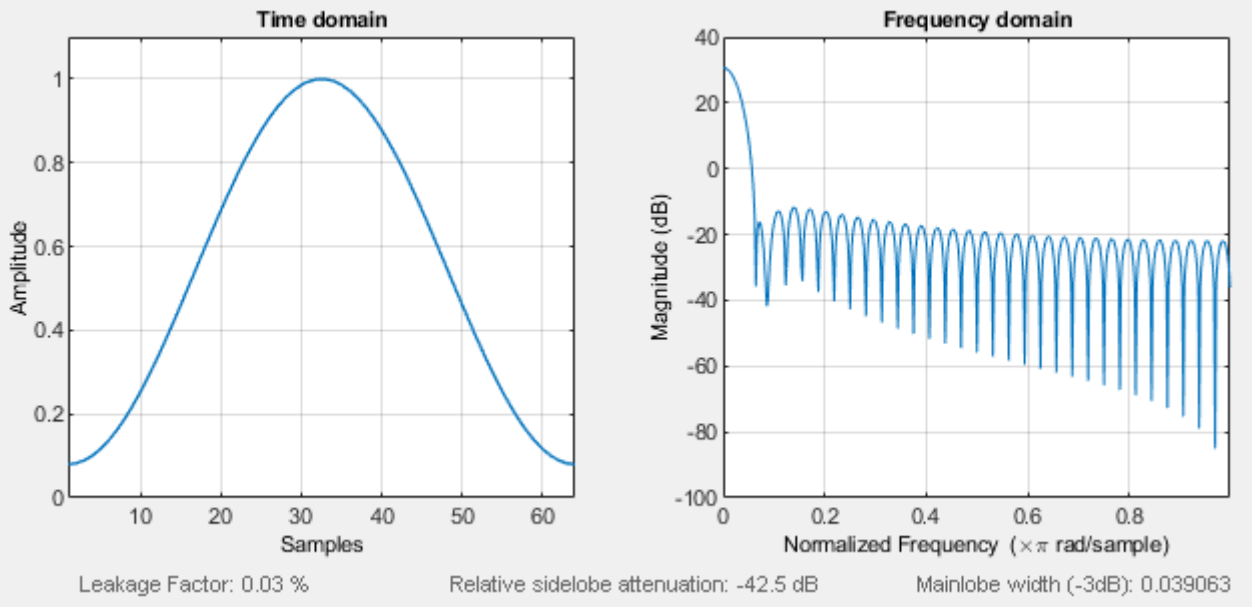

Figure 6.2: Hamming window

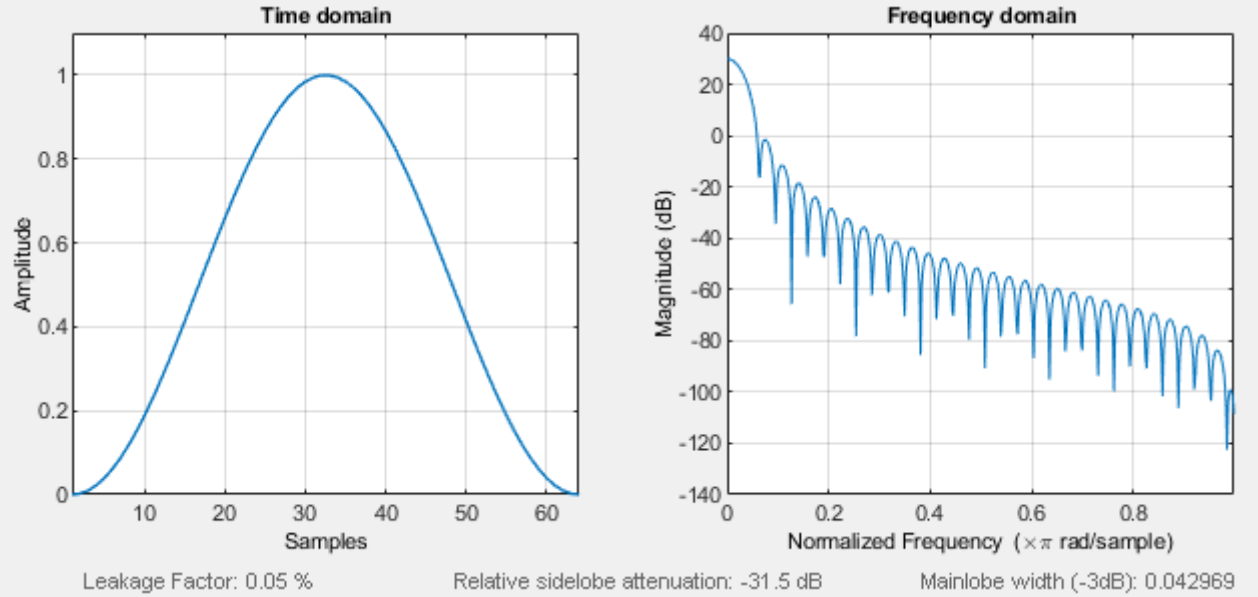

Figure 6.3: Hann window

Therefore, other methods have been explored in order to avoid these trade-offs. Few examples are the design of robust windows by solving optimization problems [41] and the use of adaptive beamformers based on the computation of the minimum variance [42]. Despite these methods work perfectly fine in theory and in simulations, in real acquisitions they perform less than or equal to those that don't implement any clutter filter.

Another interesting technique, used to reduce the clutter effect, is the singular value decomposition (SVD) filter, which was originally introduced to the ultrasound field for Doppler images to distinguish and reduce the background signal with respect to the weak blood signal [43]. SVD uses a set of n_a images, each with dimensions (n_x, n_z). These images are rearranged into a matrix P, with dimensions $(n_x * n_z, n_a)$, which is then decomposed into its singular value components according to the following formula:

$$P = U\Delta V^H = \sum_i \lambda_i U_i \times V_i \tag{6.1}$$

where,

U = unitary matrix with dimensions $(n_x \times n_z, n_x \times n_z)$

Δ = rectangular diagonal matrix with dimensions $(n_x * n_z, n_a)$ that contains the singular values

V^H = conjugate transpose of V

V = orthonormal matrix with dimensions (n_a, n_a)

λ_i = singular values of P

U_i = i-th column of U

V_i = i-th column of V

The core idea is to observe the correlation between images acquired in short time intervals. For instance, the background has high coherence in subsequent images and it is possible to distinguish it from moving subjects, such as blood, hence the convenience of using this method for Doppler images. Instead, when using the plane wave methods, images acquired with different steering angles present sidelobes with very low coherence. Because of this, the sidelobes contributions will be found most likely in the last singular values [43]. To extract the main lobe it is therefore sufficient to establish a threshold for the number of singular values to be accepted:

$$P_{mainlobe} = \sum_{i=1}^{\beta} \lambda_i U_i \times V_i \tag{6.2}$$

The same authors of the SVD implementation in CPWC imaging proposed also another method, which supposedly can stretch the reduction of number of planes even further. They use the concept of distance, which is commonly employed in classification problems of fea-

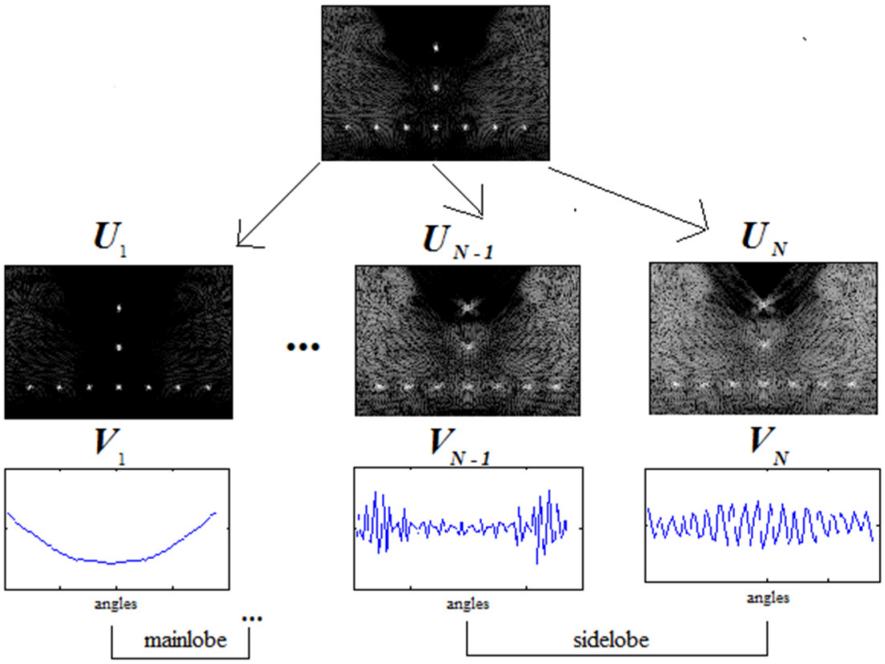

Figure 6.4: Graphical explanation of the method proposed by [43]

ture selection, to compute the coherence. In particular, rather than the Euclidean distance, they use the probabilistic effective distance, first introduced for studies on epidemics [44]. Let's analyse in detail this sidelobe reduction method.

Since this is a feature selection problem, first, a matrix containing the features from the received and beamformed radiofrequency data is defined:

$$X = [x_1, ..., x_N] \tag{6.3}$$

where x_i is a column vector with all the features computed in a certain point for the $i-th$ plane wave transmitted. x_i has dimension d, that is in fact the number of features computed. The authors used as only feature the signals' envelope. For computing the effective distance, it is necessary to define a connectivity matrix, whose elements have a certain probability of belonging to each other's class. To achieve that, the following vector is defined for each x_i:

$$p_i = [p_{i,1}, ..., p_{i,i-1}, 0, p_{i,i+1}, ..., p_{i,N}]^T \tag{6.4}$$

where, $p_{i,j}$ represents how much x_j contributes to the reconstruction of x_i, and it is acquired by solving a modified l_1 minimization problem:

$$\min_{p_i} |p_i|_1, \qquad s.t. \qquad x_i - Xp_i < \delta, \qquad 1 = 1^T p_i \tag{6.5}$$

where δ is a tolerance.

The 0 contribution in p_i means that the element $p_{i,j}$ with $i = j$ has been removed. With these vectors, the connectivity matrix of dimension $(N \times N)$ is constructed:

$$P = [p_1, ..., p_N]^T \tag{6.6}$$

At this point the effective distance can be computed as:

$$EF = \frac{1}{P_{mn}} \tag{6.7}$$

where P_{mn} is the probability of an element n of belonging to an element m's class, defined in the connectivity matrix P. Limit of this definition of effective distance is that the envelope of the radiofrequency data has amplitudes very similar, bringing therefore P_{mn} values to be all close to 1. Therefore Guo *et.al.* proposed a modified definition of effective distance:

$$ED_g = 1 - \min_{j=1...N} (\sum_{i=1}^{N} p_{i,j}) \tag{6.8}$$

The smaller the connectivity is, the higher the distance is.

Thanks to this definition it is therefore possible to separate the image into three regions, by choosing two thresholds: one dominated by the mainlobe, one dominated by sidelobes and one for the background. As Figure 6.5 shows, Guo work results are very promising, since the method seems very robust against noise and performs even better than SVD.

The method was tested by the authors both with simulations on Field II and acquisitions with Verasonics, and it effectively proved the possibility of reducing the number of compounding angles without risking an image quality degradation.

6.2 Fast Beamforming

As the Nyquist-Shannon theorem states, in order to reconstruct a signal from its samples, it is necessary to use a sampling frequency at least 2 times the maximum frequency of the signal itself. Besides, it is generally good practice to increase even more the sampling to at

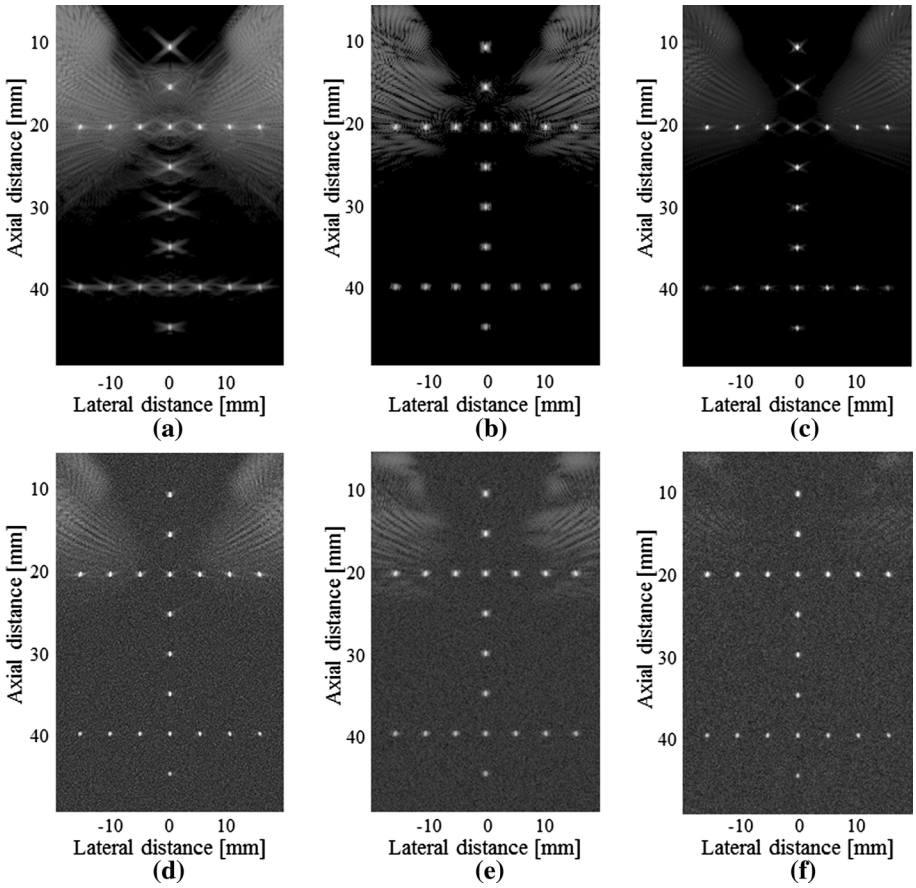

Figure 6.5: Images of scatterers processed with only CPWC (a)(d), CPWC with SVD (b)(e) and CPWC with effective distance (c)(f). The first row has no noise, while in the second row a -30dB noise was added [39]

least 4 times the maximum frequency. This translates into the need for more space in memory and also the increase in computational load, thus hindering the possibility of realizing real-time acquisitions and processing. If, however, instead of performing beamforming in the time domain, the frequency domain is used, it is possible to obtain the same processing quality for a much lower sampling frequency, namely with the Nyquist frequency or even a sub-Nyquist frequency. According to some authors, the frequency-domain beamforming (FDBF) allows to achieve a 10-fold reduction in the sampling rate with respect to normal acquisitions [45].

Let's now analyse how to perform beamforming in the Fourier domain, following the steps proposed by Chernyakova and Eldar [45]. The sub-sampled signals can be obtained thanks to the concept of Xampling, first introduced in the telecommunication sector [46]. This technique is mainly implemented for two types of applications:

- When the received signals spectrum is a multiband, *i.e.* the frequencies vary and are unknown a priori;

- When the signals can follow different paths and, therefore, their delays are not known.

In traditional signal processing, to reconstruct a signal it is necessary to know a priori to which subspace the signal belongs to. When this is not possible, the union of subspaces is considered, *i.e.* the signal may belong to any of A_{λ_i} subspaces:

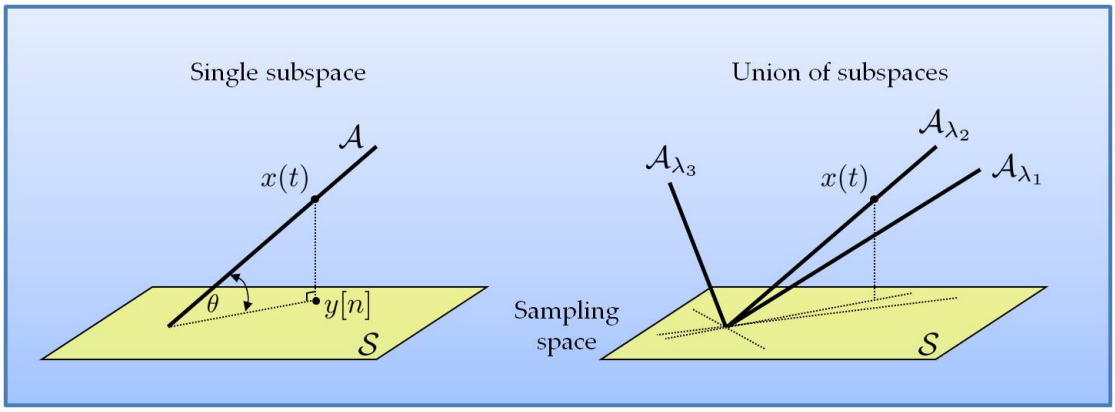

Figure 6.6: (a) known subspace (b) union of subspaces [46]

With a Xampling architecture it is possible to change the bandwidth of a signal to a lower one, thanks to the union compressor, which unites all the possible subspaces into S, that has lower dimension.
For ultrasounds, when using Gaussian modulated signals, Xampling corresponds to using a bandpass filter for decrementing the sampling frequency.

The image is obtained after performing the inverse Fourier transform on the Fourier beamformed signal, which in turn is obtained from the Fourier coefficients of the raceived radiofrequency data. Let's therefore find the correspondence between the Fourier coefficients of the beamformed signal and those of the radiofrequency data.
As seen in Chapter 2, the beamformed signal in position (x, z) can be expressed as:

$$s(x,z) = \int_{x-a}^{x+a} RF(x_1, \tau(\alpha, x_1, x, z))dx_1 \tag{6.9}$$

It is usually common practice to assign weights to the delayed RF data. The weight function depends on both time and depth, so that dynamic aperture and apodization can ensure the F-number constant all over the image:

$$s(x,z) = \int_{x-a}^{x+a} w(t; x_f) RF(x_1, \tau(\alpha, x_1, x, z))dx_1 \tag{6.10}$$

Since we are working on pixels, the above equation can be discretized as follows:

$$s(x,z) = \sum_{m=x-a}^{x+a} w(t;x_f) RF(m, \tau(\alpha, m, x, z)) \tag{6.11}$$

Its Fourier coefficients are therefore:

$$c[k] = \frac{1}{T}\int_0^T s(x,z) e^{-j\frac{2\pi}{T}kt} dt = \sum_{m=x-a}^{x+a} \hat{c}_m[k] \tag{6.12}$$

where T is defined by the imaging depth, and

$$\hat{c}_m[k] = \frac{1}{T}\int_0^T w(t;x_f) RF(m, \tau(\alpha, m, x, z) e^{-j\frac{2\pi}{T}kt} dt \tag{6.13}$$

The RF data can be rewritten in terms of its Fourier coefficients called $c_m[n]$, thus obtaining:

$$\hat{c}_m[k] = \sum_n c_m[n] \frac{1}{T}\int_0^T w(t;x_f) e^{-j\frac{2\pi}{T}(k-n)t} dt \tag{6.14}$$

which can be expressed also as:

$$\hat{c}_m[k] = \sum_n c_m[k-n] W[n] \tag{6.15}$$

where $W[n]$ are the Fourier coefficients of the weight function, which doesn't depend on the RF data and, hence, can be computed even before the acquisitions.

Appendix

A.1 CPWC Matlab Script for Field II

```
clear all
close all
clc

tic;

%% Set parameters
na = 4;             % Number of angles used to perform
   coherent compounding
c = 1540;           % Wave speed in tissues
fs = 100e6;         % Sampling frequency

field_init(0);      % Initialize Field II
set_field('c',c);
set_field('fs',fs);
set_field('use_rectangles',1);

% Comment if you don't want attenuation
Freq_att = 0.5*100/1e6;
att_f0 = 6e6;
att = att_f0*Freq_att;
set_field('att',att);
set_field('Freq_att',Freq_att);
set_field('att_f0',att_f0);
set_field('use_att',1);


%% Define transducer
Trans.name = 'L11-4v';
Trans.numelements = 128;
Trans.frequency = 6.25;
                                                    % [MHz]
Trans = computeTrans(Trans);
Trans.elementWidth_m = Trans.elementWidth/1000;
                            % [m]
Trans.elementHeight_m = Trans.elevationApertureMm/1000;
                     % [m]
Trans.elementKerf_m = (Trans.spacingMm - Trans.elementWidth)
   /1000;       % [m]

focus = [0 0 0];      % Initial focal point [m]

%% Define transmit and receive
xdc_Tx = xdc_linear_array(Trans.numelements, Trans.
   elementWidth_m, Trans.elementHeight_m, Trans.elementKerf_m,
    10, 10, focus);
xdc_Rx = xdc_linear_array(Trans.numelements, Trans.
   elementWidth_m, Trans.elementHeight_m, Trans.elementKerf_m,
    10, 10, focus);
```

```
% Calculate the apodization
apo_vector_Tx = tukeywin(Trans.numelements,0.25);       % To
   prevent edge wave
apo_vector_Rx = ones(1,Trans.numelements);
xdc_apodization(xdc_Tx, 0, apo_vector_Tx');
xdc_apodization(xdc_Rx, 0, apo_vector_Rx);

% Set the impulse response of the transmit aperture
fo = Trans.frequency*1e6;
impulse_response = sin(2*pi*fo*(0:1/fs:2/fo));
impulse_response = impulse_response.*hanning(max(size(
   impulse_response)))';
xdc_impulse(xdc_Tx, impulse_response);

% Set the impulse response for the receive aperture
xdc_impulse(xdc_Rx, impulse_response);

% Set center focus for xmit and rcv aperture
xdc_center_focus(xdc_Tx,focus);
xdc_center_focus(xdc_Rx,focus);
xdc_focus_times(xdc_Tx,0,zeros(1,Trans.numelements)); % No
   focusing
xdc_focus_times(xdc_Rx,0,zeros(1,Trans.numelements)); % No
   focusing

%% Create Multi Plane Waves
prompt = 'Do you want to select already existing CPWC sequence
   ? Y/N: ';
str = input(prompt,'s');
if str == 'N' || str == 'n'
    disp('Generating the waves...');
    Resource.Parameters.numTransmit = Trans.numelements;
    [multiWaveforms, startAngle, dtheta, waves_delay] =
       generateCPWC(na, Trans, fs);
    disp('Done');
else
    msg = ['Please select a MW file with na = ', num2str(na)];
    disp(msg);
    [file,path] = uigetfile('*.mat');
    load(file);
end

% Check Multi Plane Waves
for nacq = 1:na
    figure(), imagesc(multiWaveforms(nacq).tot);
end

%% Define phantom
% Define phantom size
x_size = (Trans.ElementPos(end,1)-Trans.ElementPos(1,1))/1000;
```

```
      %  Width of phantom [m]
y_size = 10/1000;    %  Transverse width of phantom [m]
z_size = 80/1000;    %  Height of phantom [m]
z_start = 10/1000;   %  Start of phantom surface [m]

N = 22;

% Create the scatterers
[positions, amp] = scatter(x_size, y_size, z_size, z_start, N)
    ;

%% Transmit, receive and process RF data
% Transmit plane waves and receive
for nacq=1:na
    ele_waveform(xdc_Tx, (1:Trans.numelements)',
       multiWaveforms(nacq).tot');
    [data(nacq).rf, tstart] = calc_scat_multi(xdc_Tx, xdc_Rx,
       positions, amp');
    figure(), imagesc(data(nacq).rf);
end

%% Decode (allows to obtain signals as if they were obtained
   from a single steering angle)
for nacq = 1:na
    dec(nacq).rf = data(nacq).rf;
end

% Resample rf data
f_resample = Trans.frequency*4e6;
for nacq = 1:na
    dec(nacq).rf = resample(dec(nacq).rf,f_resample,fs);
    figure(), imagesc(dec(nacq).rf);
end

same_size = zeros(size(dec(1).rf,1)-size(dec(2).rf,1),Trans.
   numelements);
dec(2).rf = [dec(2).rf; same_size];
dec(3).rf = [dec(3).rf; same_size];

%% Beamforming
%Axes definition
x_axis = 0:x_size/400:x_size;                %[m]
z_axis = z_start:(z_size-z_start)/1600:z_size;        %[m]

%Pixels positions
X = repmat(x_axis,length(z_axis),1);
Z = repmat(z_axis',1,length(x_axis));

%Transducers pitch
pitch = Trans.spacingMm/1000;       %[m]
```

```
%F-number and aperture definition
F = Trans.elevationFocusMm/Trans.elevationApertureMm;
M = ceil((z_axis/(2*F))/pitch);

%Delay matrices initialization
delay_transmission = zeros(size(X,1),size(X,2),na);
delay_receive = zeros(size(X,1),size(X,2),Trans.numelements);

for nacq = 1:ceil(na/2)
    alpha = (startAngle-(nacq-1)*dtheta);
    if alpha == 0
        delay_transmission(:,:,nacq) = Z/c;
    else
        delay_transmission(:,:,nacq) = (Z*cos(alpha)+X*sin(
           alpha))/c;
        delay_transmission(:,:,na-(nacq-1)) = flip(
           delay_transmission(:,:,nacq),2);
    end
end

x_channels = (Trans.ElementPos(:,1) + abs(Trans.ElementPos
   (1,1)))/1000;    %[m]
for i = 1:Trans.numelements
    delay_receive(:,:,i) = sqrt((X-x_channels(i)).^2+Z.^2)/c;
end

interp_value = zeros(size(X,1),size(X,2),Trans.numelements);
weights = zeros(size(X,1),size(X,2),Trans.numelements);
t = tstart:1/f_resample:(tstart+(size(dec(1).rf,1)-1)/
   f_resample);

for nacq = 1:na
    for i = 1:Trans.numelements
        delay_tot = delay_receive(:,:,i) + delay_transmission
           (:,:,nacq);
        interp_value(:,:,i) = interp1(t,dec(nacq).rf(:,i),
           delay_tot,'linear',0);

        delta_fm = repmat(abs(X(1,:)-x_channels(i))/c,size(X
           ,1),1);
        N_t = (0.54^2 + (0.46^2)/2)*c*delay_tot/(2*F);
        A_m = (0.54 + 0.46*cos(4*pi*F*delta_fm./delay_tot));
        weights(:,:,i) = (delay_tot >= (4*F*delta_fm)).*A_m./
           N_t;
    end
    beamformed(nacq).rf = sum(interp_value.*weights,3);
    figure(), imagesc(beamformed(nacq).rf);
end

%% Coherent compounding
%Coherent compounding
```

```
frame_rf = beamformed(1).rf;
for nacq = 2:na
    frame_rf = frame_rf + beamformed(nacq).rf;
end

frame_def = abs(hilbert(frame_rf));

%Free space for apertures
xdc_free (xdc_Tx)
xdc_free (xdc_Rx)

field_end;
toc;

%% Display reconstructed frame
log_env = 20*log10(frame_def/max(max(frame_def)));
figure(),imagesc((-x_size/2:x_size/400:x_size/2)*1000,z_axis
   *1000,log_env),colormap(gray(256)),colorbar;
clim = caxis;
caxis([clim(2)-40, clim(2)]);
daspect([1 1 1]);
```

A.1.1 CPWC plane waves

```
function [multiWaveforms, startAngle, dtheta, waves_delay] =
   generateMW(na, Trans, fs)

% Load the single waveform generated through ArbWaveToolbox
load('Single waveform.mat','TW');

% Remove ringing effect
zci = @(v) find(v(:).*circshift(v(:), [-1 0]) <= 0);        %
   Returns Zero-Crossing Indices
zx = zci(TW.Waveform);
negative_peaks = TW.Waveform(islocalmin(TW.Waveform));
negative_peaks_reordered = sort(negative_peaks,'ascend');
peak_a_pos = find(TW.Waveform == negative_peaks_reordered(3));
peak_b_pos = find(TW.Waveform == negative_peaks_reordered(4));
if peak_a_pos < peak_b_pos
    left_peak_pos = peak_a_pos;
    right_peak_pos = peak_b_pos;
else
    left_peak_pos = peak_b_pos;
    right_peak_pos = peak_a_pos;
end
left_boundary = zx(find(zx > left_peak_pos,1));             %
   Left boundary of the tukey window
right_boundary = zx(find(zx < right_peak_pos,1,'last')+1);
   % Right boundary of the tukey window
lenw = right_boundary - left_boundary;
window = [zeros(left_boundary-1,1); tukeywin(lenw,0.25); zeros
   (length(TW.Waveform)-right_boundary+1,1)];
```

```
Waveform = TW.Waveform .* window;                % Single
    waveform windowed
start = find(Waveform ~= 0,1);
Waveform = Waveform(start-1:end);


dtheta = 4*pi/180;                    % Angle step
startAngle = (na-1)*(dtheta/2);       % Starting angle (positive
    )

for nacq = 1:na

    wave_polarity = zeros(length(Waveform),na);
    for i = 1:na
        wave_polarity(:,i) = Waveform;      % Assign the
            correct polarity to the wave
    end

    shift = zeros(na,Trans.numelements);
    alpha = startAngle-(nacq-1)*dtheta;
    if alpha >= 0
        shift(i,:) = round((0:0.0003:0.0381).*tan(alpha)*fs
            /1540);
    else
        shift(i,:) = round((0:0.0003:0.0381).*tan(alpha)*fs
            /1540);
        shift(i,:) = flip(abs(shift(i,:)));
    end

    max_shift = max(shift(i,:));
    buf = zeros(max_shift+size(wave_polarity,1),Trans.
        numelements);

    for j = 1:Trans.numelements
        buf(shift(i,j)+1:shift(i,j)+size(wave_polarity,1),j) =
            wave_polarity(:,i);       % Shift the waveform
            according to the assigned delay
    end

    multiWV = buf;
    waves_delay(i) = size(multiWV,1);


    multiWaveforms(nacq).tot = multiWV;              % Save the
        n-th transmission waves in a structure
    clear multiWV
    clear TX
end
```

A.2 MPW Matlab Script for Field II

```
clear all
close all
clc

tic;

%% Add in functions' paths
addpath('C:\Users\elena\Desktop\Master_thesis\FieldII');
addpath('C:\Users\elena\Desktop\Master_thesis\Vantage
    -4.0.1-1903121200\Thesis\MyFunctions\');

%% Set parameters
na = 4;              % Number of angles used to perform
    coherent compounding
c = 1540;            % Wave speed in tissues
fs = 100e6;          % Sampling frequency

field_init(0);       % Initialize Field II
set_field('c',c);
set_field('fs',fs);
set_field('use_rectangles',1);

% Comment if you don't want attenuation
Freq_att = 0.5*100/1e6;
att_f0 = 6e6;
att = att_f0*Freq_att;
set_field('att',att);
set_field('Freq_att',Freq_att);
set_field('att_f0',att_f0);
set_field('use_att',1);

%% Define transducer
Trans.name = 'L11-4v';
Trans.numelements = 128;
Trans.frequency = 6.25;
                                                    % [MHz]
Trans = computeTrans(Trans);
Trans.elementWidth_m = Trans.elementWidth/1000;
                             % [m]
Trans.elementHeight_m = Trans.elevationApertureMm/1000;
                      % [m]
Trans.elementKerf_m = (Trans.spacingMm - Trans.elementWidth)
    /1000;       % [m]

focus = [0 0 0];      % Initial focal point [m]

%% Define transmit and receive
xdc_Tx = xdc_linear_array(Trans.numelements, Trans.
    elementWidth_m, Trans.elementHeight_m, Trans.elementKerf_m,
```

```
    10, 10, focus);
xdc_Rx = xdc_linear_array(Trans.numelements, Trans.
    elementWidth_m, Trans.elementHeight_m, Trans.elementKerf_m,
    10, 10, focus);

% Calculate the apodization
apo_vector_Tx = tukeywin(Trans.numelements,0.25);       % To
    prevent edge wave
apo_vector_Rx = ones(1,Trans.numelements);
xdc_apodization(xdc_Tx, 0, apo_vector_Tx');
xdc_apodization(xdc_Rx, 0, apo_vector_Rx);

% Set the impulse response of the transmit aperture
fo = Trans.frequency*1e6;
impulse_response = sin(2*pi*fo*(0:1/fs:2/fo));
impulse_response = impulse_response.*hanning(max(size(
    impulse_response)))';
xdc_impulse(xdc_Tx, impulse_response);

% Set the impulse response for the receive aperture
xdc_impulse(xdc_Rx, impulse_response);

% Set center focus for xmit and rcv aperture
xdc_center_focus(xdc_Tx,focus);
xdc_center_focus(xdc_Rx,focus);
xdc_focus_times(xdc_Tx,0,zeros(1,Trans.numelements)); % No
    focusing
xdc_focus_times(xdc_Rx,0,zeros(1,Trans.numelements)); % No
    focusing

%% Create Multi Plane Waves
prompt = 'Do you want to select already existing MPW sequence?
    Y/N: ';
str = input(prompt,'s');
if str == 'N' || str == 'n'
    disp('Generating the waves...');
    Resource.Parameters.numTransmit = Trans.numelements;
    [multiWaveforms, startAngle, H, dtheta, waves_delay] =
        generateMW(na, Trans, fs);
    disp('Done');
else
    msg = ['Please select a MW file with na = ', num2str(na)];
    disp(msg);
    [file,path] = uigetfile('*.mat');
    load(file);
end

% Check Multi Plane Waves
for nacq = 1:na
    figure(), imagesc(multiWaveforms(nacq).tot);
end
```

```
%% Define phantom
% Define phantom size
x_size = (Trans.ElementPos(end,1)-Trans.ElementPos(1,1))/1000;
      %  Width of phantom [m]
y_size = 10/1000;   %  Transverse width of phantom [m]
z_size = 80/1000;   %  Height of phantom [m]
z_start = 10/1000;  %  Start of phantom surface [m]

N = 22;

% Create the scatterers
[positions, amp] = scatter(x_size, y_size, z_size, z_start, N)
    ;

%% Transmit, receive and process RF data
% Transmit plane waves and receive
for nacq=1:na
    ele_waveform(xdc_Tx, (1:Trans.numelements)',
       multiWaveforms(nacq).tot');
    [data(nacq).rf, tstart] = calc_scat_multi(xdc_Tx, xdc_Rx,
       positions, amp');
    figure(), imagesc(data(nacq).rf);
end

%% Decode (allows to obtain signals as if they were obtained
   from a single steering angle)
for nacq = 1:na
    dec(nacq).rf = zeros(size(data(nacq).rf,1),size(data(1).rf
       ,2));
    for  i = 1:na
        dec(nacq).rf = dec(nacq).rf + data(i).rf*H(nacq,i);
    end
    figure(), imagesc(dec(nacq).rf);
end

for nacq = 2:na
    dec(nacq).rf = [dec(nacq).rf((waves_delay(nacq-1)+1):end
       ,:); zeros(waves_delay(nacq-1),Trans.numelements)];
    figure(), imagesc(dec(nacq).rf);
end

% Resample rf data
f_resample = Trans.frequency*4e6;
for nacq = 1:na
    dec(nacq).rf = resample(dec(nacq).rf,f_resample,fs);
    figure(), imagesc(dec(nacq).rf);
end

%% Beamforming
%Axes definition
```

```
x_axis = 0:x_size/400:x_size;                    %[m]
z_axis = z_start:(z_size-z_start)/1600:z_size;          %[m]

%Pixels positions
X = repmat(x_axis,length(z_axis),1);
Z = repmat(z_axis',1,length(x_axis));

%Transducers pitch
pitch = Trans.spacingMm/1000;          %[m]

%F-number and aperture definition
F = Trans.elevationFocusMm/Trans.elevationApertureMm;
M = ceil((z_axis/(2*F))/pitch);

%Delay matrices initialization
delay_transmission = zeros(size(X,1),size(X,2),na);
delay_receive = zeros(size(X,1),size(X,2),Trans.numelements);

for nacq = 1:ceil(na/2)
    alpha = (startAngle-(nacq-1)*dtheta);
    if alpha == 0
        delay_transmission(:,:,nacq) = Z/c;
    else
        delay_transmission(:,:,nacq) = (Z*cos(alpha)+X*sin(
           alpha))/c;
        delay_transmission(:,:,na-(nacq-1)) = flip(
           delay_transmission(:,:,nacq),2);
    end
end

x_channels = (Trans.ElementPos(:,1) + abs(Trans.ElementPos
   (1,1)))/1000;    %[m]
for i = 1:Trans.numelements
    delay_receive(:,:,i) = sqrt((X-x_channels(i)).^2+Z.^2)/c;
end

interp_value = zeros(size(X,1),size(X,2),Trans.numelements);
weights = zeros(size(X,1),size(X,2),Trans.numelements);
t = tstart:1/f_resample:(tstart+(size(dec(1).rf,1)-1)/
   f_resample);

for nacq = 1:na
    for i = 1:Trans.numelements
        delay_tot = delay_receive(:,:,i) + delay_transmission
           (:,:,nacq);
        interp_value(:,:,i) = interp1(t,dec(nacq).rf(:,i),
           delay_tot,'linear',0);

        delta_fm = repmat(abs(X(1,:)-x_channels(i))/c,size(X
           ,1),1);
        N_t = (0.54^2 + (0.46^2)/2)*c*delay_tot/(2*F);
```

```
        A_m = (0.54 + 0.46*cos(4*pi*F*delta_fm./delay_tot));
        weights(:,:,i) = (delay_tot >= (4*F*delta_fm)).*A_m./
            N_t;
    end
    beamformed(nacq).rf = sum(interp_value.*weights,3);
    figure(), imagesc(beamformed(nacq).rf);
end

%% Coherent compounding
%Coherent compounding
frame_rf = beamformed(1).rf;
for nacq = 2:na
    frame_rf = frame_rf + beamformed(nacq).rf;
end

frame_def = abs(hilbert(frame_rf));

%Free space for apertures
xdc_free (xdc_Tx)
xdc_free (xdc_Rx)

field_end;
toc;

%% Display reconstructed frame
log_env = 20*log10(frame_def/max(max(frame_def)));
figure(),imagesc((-x_size/2:x_size/400:x_size/2)*1000,z_axis
    *1000,log_env),colormap(gray(256)),colorbar;
clim = caxis;
caxis([clim(2)-40, clim(2)]);
daspect([1 1 1]);
```

A.2.1 MPW plane waves

```
function [multiWaveforms, startAngle, H, dtheta, waves_delay]
    = generateMW(na, Trans, fs)

% Load the single waveform generated through ArbWaveToolbox
load('Single waveform.mat','TW');

% Remove ringing effect
zci = @(v) find(v(:).*circshift(v(:), [-1 0]) <= 0);        %
    Returns Zero-Crossing Indices
zx = zci(TW.Waveform);
negative_peaks = TW.Waveform(islocalmin(TW.Waveform));
negative_peaks_reordered = sort(negative_peaks,'ascend');
peak_a_pos = find(TW.Waveform == negative_peaks_reordered(3));
peak_b_pos = find(TW.Waveform == negative_peaks_reordered(4));
if peak_a_pos < peak_b_pos
    left_peak_pos = peak_a_pos;
    right_peak_pos = peak_b_pos;
else
```

```
    left_peak_pos = peak_b_pos;
    right_peak_pos = peak_a_pos;
end
left_boundary = zx(find(zx > left_peak_pos,1));              %
   Left boundary of the tukey window
right_boundary = zx(find(zx < right_peak_pos,1,'last')+1);
   % Right boundary of the tukey window
lenw = right_boundary - left_boundary;
window = [zeros(left_boundary-1,1); tukeywin(lenw,0.25); zeros
   (length(TW.Waveform)-right_boundary+1,1)];

Waveform = TW.Waveform .* window;                % Single
   waveform windowed
start = find(Waveform ~= 0,1);
Waveform = Waveform(start-1:end);

H = hadamard(na);                        % Hadamard matrix

dtheta = 4*pi/180;                       % Angle step
startAngle = (na-1)*(dtheta/2);          % Starting angle (positive
   )

for nacq = 1:na

    wave_polarity = zeros(length(Waveform),na);
    for i = 1:na
        wave_polarity(:,i) = Waveform*H(nacq,i);      % Assign
           the correct polarity to the wave
    end

    k = 1;
    shift = zeros(na,Trans.numelements);
    for i = 1:na
        alpha = startAngle-(k-1)*dtheta;
        if alpha >= 0
            shift(i,:) = round((0:0.0003:0.0381).*tan(alpha)*
               fs/1540);
        else
            shift(i,:) = round((0:0.0003:0.0381).*tan(alpha)*
               fs/1540);
            shift(i,:) = flip(abs(shift(i,:)));
        end
        k = k+1;
    end
    for i = 1:na
        max_shift = max(shift(i,:));
        buf = zeros(max_shift+size(wave_polarity,1),Trans.
           numelements);
        for j = 1:Trans.numelements
            buf(shift(i,j)+1:shift(i,j)+size(wave_polarity,1),
               j) = wave_polarity(:,i);       % Shift the
```

```
                waveform according to the assigned delay
        end
        if i == 1
            multiWV = buf;
            waves_delay(i) = size(multiWV,1);
        else
            multiWV = [multiWV; buf];
            waves_delay(i) = size(multiWV,1);
        end
    end

    multiWaveforms(nacq).tot = multiWV;              % Save the
        n-th transmission waves in a structure
    clear multiWV
    clear TX
end
```

A.3 CDW Matlab Script for Field II

```
clear all
close all
clc

tic;

%% Set parameters
na = 8;              % Length of the encoding matrix
angles = 2;          % Half of the number of angles used for
   compounding
dtheta = 4*pi/180;   % Angle step
c = 1540;            % Wave speed in tissues
fs = 100e6;          % Sampling frequency

field_init(0);       % Initialize Field II
set_field('c',c);
set_field('fs',fs);
set_field('use_rectangles',1);

% Comment if you don't want attenuation
Freq_att = 0.5*100/1e6;
att_f0 = 6e6;
att = att_f0*Freq_att;
set_field('att',att);
set_field('Freq_att',Freq_att);
set_field('att_f0',att_f0);
set_field('use_att',1);

%% Define transducer
Trans.name = 'L11-4v';
Trans.numelements = 128;
Trans.frequency = 6.25;
                                                    % [MHz]
Trans = computeTrans(Trans);
Trans.elementWidth_m = Trans.elementWidth/1000;
                            % [m]
Trans.elementHeight_m = Trans.elevationApertureMm/1000;
                     % [m]
Trans.elementKerf_m = (Trans.spacingMm - Trans.elementWidth)
   /1000;       % [m]

focus = [0 0 0];      % Initial focal point [m]

%% Define transmit and receive
xdc_Tx = xdc_linear_array(Trans.numelements, Trans.
   elementWidth_m, Trans.elementHeight_m, Trans.elementKerf_m,
    10, 10, focus);
xdc_Rx = xdc_linear_array(Trans.numelements, Trans.
   elementWidth_m, Trans.elementHeight_m, Trans.elementKerf_m,
```

```
    10, 10, focus);

% Calculate the apodization
apo_vector_Tx = tukeywin(Trans.numelements,0.25);       % To
   prevent edge wave
apo_vector_Rx = ones(1,Trans.numelements);
xdc_apodization(xdc_Tx, 0, apo_vector_Tx');
xdc_apodization(xdc_Rx, 0, apo_vector_Rx);

% Set the impulse response of the transmit aperture
fo = Trans.frequency*1e6;
impulse_response = sin(2*pi*fo*(0:1/fs:2/fo));
impulse_response = impulse_response.*hanning(max(size(
   impulse_response)))';
xdc_impulse(xdc_Tx, impulse_response);

% Set the impulse response for the receive aperture
xdc_impulse(xdc_Rx, impulse_response);

% Set center focus for xmit and rcv aperture
xdc_center_focus(xdc_Tx,focus);
xdc_center_focus(xdc_Rx,focus);
xdc_focus_times(xdc_Tx,0,zeros(1,Trans.numelements)); % No
   focusing
xdc_focus_times(xdc_Rx,0,zeros(1,Trans.numelements)); % No
   focusing

%% Create Cascaded Dual-Polarity Waves
prompt = 'Do you want to select already existing CDW sequence?
    Y/N: ';
str = input(prompt,'s');
if str == 'N' || str == 'n'
    for l = 1:angles
        disp('Generating the waves...');
        Resource.Parameters.numTransmit = Trans.numelements;

        startAngle = (2*pi/180)+dtheta*(l-1);     % Starting
           angle (positive)

        [multiWaveforms, delay(l).samples] = generateCDW(na,
           Trans, fs, startAngle);
        disp('Done');

        % Check Multi Plane Waves
        for nacq = 1:2
            figure(), imagesc(multiWaveforms(nacq).tot);
        end

        CDW(l).pair(:,:,1) = multiWaveforms(1).tot;
        CDW(l).pair(:,:,2) = multiWaveforms(2).tot;
    end
```

```
else
    msg = ['Please select a CDW file with na = ', num2str(na),
       'and angles = ',num2str(angles)];
    disp(msg);
    [file,path] = uigetfile('*.mat');
    load(file);
end

%% Define phantom
% Define phantom size
x_size = (Trans.ElementPos(end,1)-Trans.ElementPos(1,1))/1000;
      %  Width of phantom [m]
y_size = 10/1000;   %  Transverse width of phantom [m]
z_size = 80/1000;   %  Height of phantom [m]
z_start = 10/1000;  %  Start of phantom surface [m]

N = 22;

% Create the scatterers
[positions, amp] = scatter(x_size, y_size, z_size, z_start, N)
   ;

for l = 1:angles
    %% Transmit, receive and process RF data
    % Transmit plane waves and receive
    for nacq=1:2
        ele_waveform(xdc_Tx, (1:Trans.numelements)', CDW(l).
           pair(:,:,nacq)');
        [data(l).rf(:,:,nacq), tstart(l)] = calc_scat_multi(
           xdc_Tx, xdc_Rx, positions, amp');
    end
end

%Axes definition
x_axis = 0:x_size/400:x_size;                %[m]
z_axis = z_start:(z_size-z_start)/1600:z_size;        %[m]

%Pixels positions
X = repmat(x_axis,length(z_axis),1);
Z = repmat(z_axis',1,length(x_axis));

%Transducers pitch
pitch = Trans.spacingMm/1000;       %[m]

%F-number and aperture definition
F = Trans.elevationFocusMm/Trans.elevationApertureMm;
M = ceil((z_axis/(2*F))/pitch);

x_channels = (Trans.ElementPos(:,1) + abs(Trans.ElementPos
   (1,1)))/1000;   %[m]
delay_receive = zeros(size(X,1),size(X,2),Trans.numelements);
```

```
for i = 1:Trans.numelements
    delay_receive(:,:,i) = sqrt((X-x_channels(i)).^2+Z.^2)/c;
end

for l = 1:angles
    %Decode (allows to obtain signals as if they were obtained
        from a single steering angle)
    y1(:,:,1) = data(l).rf(:,:,1);
    y2(:,:,1) = data(l).rf(:,:,2);
    figure(),subplot(1,2,1),imagesc(y1(:,:,1)),subplot(1,2,2),
       imagesc(y2(:,:,1));
    k = 1;
    for i = 1:log2(na)
        k = k+1;
        y1(:,:,i+1) = y1(:,:,i) + y2(:,:,k-1);
        y2(:,:,k) = y1(:,:,i) - y2(:,:,k-1);
        figure(),subplot(1,2,1),imagesc(y1(:,:,i+1)),subplot
           (1,2,2),imagesc(y2(:,:,k));

        if i == log2(na)
            tau = (na/2)*delay(l).samples(1);
        else
            tau = na/(2^(i+1))*delay(l).samples(1);
        end

        k = k+1;
        y2(:,:,k) = [y2((tau+1):end,:,k-1); zeros(tau,Trans.
           numelements)];
        figure(),subplot(1,2,1),imagesc(y1(:,:,i+1)),subplot
           (1,2,2),imagesc(y2(:,:,k));
    end

    y1_def = y1(:,:,end);
    y2_def = y2(:,:,end);

    % Resample rf data
    f_resample = Trans.frequency*4e6;
    y1_def = resample(y1_def,f_resample,fs);
    y2_def = resample(y2_def,f_resample,fs);
    figure(),subplot(1,2,1),imagesc(y1_def),subplot(1,2,2),
       imagesc(y2_def);

    %% Beamforming
    %Delay matrices
    theta = (0.5*pi/180)+dtheta*(l-1);
    delay_transmission(:,:,1) = (Z*cos(theta)+X*sin(theta))/c;
    delay_transmission(:,:,2) = flip(delay_transmission(:,:,1)
       ,2);

    interp_value = zeros(size(X,1),size(X,2),Trans.numelements
       );
```

```
    weights = zeros(size(X,1),size(X,2),Trans.numelements);
    t = tstart(l):1/f_resample:(tstart(l)+(size(y1_def,1)-1)/
       f_resample);

    for i = 1:Trans.numelements

        delay_tot1 = delay_receive(:,:,i) + delay_transmission
           (:,:,1);
        delay_tot2 = delay_receive(:,:,i) + delay_transmission
           (:,:,2);

        interp_value1(:,:,i) = interp1(t,y1_def(:,i),
           delay_tot1,'linear',0);
        interp_value2(:,:,i) = interp1(t,y2_def(:,i),
           delay_tot2,'linear',0);

        delta_fm = repmat(abs(X(1,:)-x_channels(i))/c,size(X
           ,1),1);

        N_t1 = (0.54^2 + (0.46^2)/2)*c*delay_tot1/(2*F);
        N_t2 = (0.54^2 + (0.46^2)/2)*c*delay_tot2/(2*F);

        A_m1 = (0.54 + 0.46*cos(4*pi*F*delta_fm./delay_tot1));
        A_m2 = (0.54 + 0.46*cos(4*pi*F*delta_fm./delay_tot2));

        weights1(:,:,i) = (delay_tot1 >= (4*F*delta_fm)).*A_m1
           ./N_t1;
        weights2(:,:,i) = (delay_tot2 >= (4*F*delta_fm)).*A_m2
           ./N_t2;
    end

    beamformed(l).first = sum(interp_value1.*weights1,3);
    beamformed(l).second = sum(interp_value2.*weights2,3);
    figure(),subplot(1,2,1),imagesc(beamformed(l).first),
       subplot(1,2,2),imagesc(beamformed(l).second);

    clear y1
    clear y2
end

frame_rf = zeros(size(beamformed(1).first,1),size(beamformed
   (1).first,2));
for l = 1:angles
    %% Coherent compounding
    %Coherent compounding
    frame_rf = frame_rf + beamformed(l).first + beamformed(l).
       second;
end

frame_def = abs(hilbert(frame_rf));
```

```
%Free space for apertures
xdc_free (xdc_Tx)
xdc_free (xdc_Rx)

field_end;
toc;

%% Display reconstructed frame
log_env = 20*log10(frame_def/max(max(frame_def)));
figure(),imagesc((-x_size/2:x_size/400:x_size/2)*1000,z_axis
   *1000,log_env),colormap(gray(256)),colorbar;
clim = caxis;
caxis([clim(2)-40, clim(2)]);
daspect([1 1 1]);
```

A.3.1 CDW plane waves

```
function [multiWaveforms, waves_delay] = generateCDW(na, Trans
   , fs, startAngle)

% Load the single waveform generated through ArbWaveToolbox
load('Single waveform.mat','TW');

% Remove ringing effect
zci = @(v) find(v(:).*circshift(v(:), [-1 0]) <= 0);        %
   Returns Zero-Crossing Indices
zx = zci(TW.Waveform);
negative_peaks = TW.Waveform(islocalmin(TW.Waveform));
negative_peaks_reordered = sort(negative_peaks,'ascend');
peak_a_pos = find(TW.Waveform == negative_peaks_reordered(3));
peak_b_pos = find(TW.Waveform == negative_peaks_reordered(4));
if peak_a_pos < peak_b_pos
    left_peak_pos = peak_a_pos;
    right_peak_pos = peak_b_pos;
else
    left_peak_pos = peak_b_pos;
    right_peak_pos = peak_a_pos;
end
left_boundary = zx(find(zx > left_peak_pos,1));             %
   Left boundary of the tukey window
right_boundary = zx(find(zx < right_peak_pos,1,'last')+1);
   % Right boundary of the tukey window
lenw = right_boundary - left_boundary;
window = [zeros(left_boundary-1,1); tukeywin(lenw,0.25); zeros
   (length(TW.Waveform)-right_boundary+1,1)];

Waveform = TW.Waveform .* window;               % Single
   waveform windowed
start = find(Waveform ~= 0,1);
Waveform = Waveform(start-1:end);

H = hadamard(2);                    % Hadamard matrix
```

```
C_k = H;

for i = 1:(log2(na)-1)
    A = C_k(1,1:(size(C_k,2)/2));
    B = C_k(1,(size(C_k,2)/2+1):end);
    C = C_k(2,1:(size(C_k,2)/2));
    D = C_k(2,(size(C_k,2)/2+1):end);
    C_k = [A C B D; A -C B -D];
end

theta = [startAngle, -startAngle];

shift = zeros(2,Trans.numelements);
shift(1,:) = round((0:0.0003:0.0381).*tan(theta(1))*fs/1540);
shift(2,:) = flip(shift(1,:));
max_shift = max(shift(1,:));

for nacq = 1:2

    wave_polarity = zeros(length(Waveform),na);
    for i = 1:na
        wave_polarity(:,i) = Waveform*C_k(nacq,i);     %
           Assign the correct polarity to the wave
    end

    for i = 1:na
        buf = zeros(max_shift+size(wave_polarity,1),Trans.
           numelements);
        for j = 1:Trans.numelements
            if i <= (na/2)
                buf(shift(1,j)+1:shift(1,j)+size(wave_polarity
                   ,1),j) = wave_polarity(:,i);      % Shift
                   the waveform according to the assigned
                   delay
            else
                buf(shift(2,j)+1:shift(2,j)+size(wave_polarity
                   ,1),j) = wave_polarity(:,i);
            end
        end
        if i == 1
            multiWV = buf;
            waves_delay(i) = size(multiWV,1);
        else
            multiWV = [multiWV; buf];
            waves_delay(i) = size(multiWV,1);
        end
    end

    multiWaveforms(nacq).tot = multiWV;              % Save the
        n-th transmission waves in a structure
    clear multiWV
```

```
end
```

Bibliography

[1] J. Woo, *A Short History of the Development of Ultrasound in Obstetrics and Gynecology Part 1*, January 2002. `http://www.ob-ultrasound.net/history1.html`.

[2] M. Ezekiel and H. Joo Ha, "Emerging hifu applications in cancer therapy," *International Journal of Hyperthermia*, vol. 31, no. 3, pp. 302–309, 2015.

[3] J. D. Owens, M. Houston, D. Luebke, S. Green, J. E. Stone, and J. C. Phillips, "Gpu computing," *Proceedings of the IEEE*, vol. 96, pp. 879–899, May 2008.

[4] J. Bercoff, "Ultrafast ultrasound imaging," in *Ultrasound Imaging* (I. V. Minin and O. V. Minin, eds.), ch. 1, Rijeka: IntechOpen, 2011.

[5] `https://global.widex.com/en/blog/human-hearing-range-what-can-you-hear`.

[6] A. Carovac, F. Smajlovic, and D. Junuzovic, "Application of ultrasound in medicine," *Acta informatica medica*, vol. 19, no. 3, p. 168–171, 2011.

[7] `https://www.elprocus.com/what-is-the-piezoelectric-effect-working-and-.its-applications/`.

[8] W. Heisenberg, "On the perceptual content of quantum theoretical kinematics and mechanics," 1927.

[9] M. Tanter and M. Fink, "Ultrafast imaging in biomedical ultrasound," *IEEE Transactions on Ultrasonics, Ferroelectrics, and Frequency Control*, vol. 61, pp. 102–119, January 2014.

[10] R. Collier, C. Burckhardt, and L. Lin, *Optical Holography*. Academic press, 1971.

[11] M. Fink, "Time reversal of ultrasonic fields. i. basic principles," *IEEE Transactions on Ultrasonics, Ferroelectrics, and Frequency Control*, vol. 39, pp. 555–566, Sep. 1992.

[12] I. K. Holfort, F. Gran, and J. Jensen, "Plane wave medical ultrasound imaging using adaptive beamforming," *2008 5th IEEE Sensor Array and Multichannel Signal Processing Workshop*, pp. 288–292, 2008.

[13] G. Montaldo, M. Tanter, J. Bercoff, N. Benech, and M. Fink, "Coherent plane-wave compounding for very high frame rate ultrasonography and transient elastography," *IEEE Transactions on Ultrasonics, Ferroelectrics, and Frequency Control*, vol. 56, pp. 489–506, March 2009.

[14] P. Hoskins, "Ultrasound techniques for measurement of blood flow and tissue motion," *Biorheology*, vol. 39, pp. 451–9, 02 2002.

[15] R. G. Dantas, E. T. Costa, and S. Leeman, "Ultrasound speckle and equivalent scatterers," *Ultrasonics*, vol. 43, no. 6, pp. 405 – 420, 2005.

[16] W. Arnold and S. Hirsekorn, *Acoustical Imaging*, vol. 27. Springer Science, 2004.

[17] C. R. Cooley and B. S. Robinson, "Synthetic focus imaging using partial datasets," in *1994 Proceedings of IEEE Ultrasonics Symposium*, vol. 3, pp. 1539–1542 vol.3, Oct 1994.

[18] M. S. Taljanovic, L. H. Gimber, G. W. Becker, L. D. Latt, A. S. Klauser, D. M. Melville, L. Gao, and R. S. Witte, "Shear-wave elastography: Basic physics and musculoskeletal applications," *RadioGraphics*, vol. 37, no. 3, pp. 855–870, 2017. PMID: 28493799.

[19] J. Bercoff, G. Montaldo, T. Loupas, D. Savery, F. Mézière, M. Fink, and M. Tanter, "Ultrafast compound doppler imaging: providing full blood flow characterization," *IEEE Transactions on Ultrasonics, Ferroelectrics, and Frequency Control*, vol. 58, pp. 134–147, January 2011.

[20] S. Yuan and R. Rigor, *Regulation of Endothelial Barrier Function*, ch. 2. Morgan & Claypool Life Sciences, 2010.

[21] R. Glaser, *Biophysics*. Springer-Verlag Berlin Heidelberg, 4 ed., 2001.

[22] E. Macé, G. Montaldo, and I. Cohen, "Functional ultrasound imaging of the brain," *Nat Methods 8*, p. 662–664, 2011.

[23] D. Go, J. Kang, I. Song, and Y. Yoo, "Efficient transmit delay calculation in ultrasound coherent plane-wave compound imaging for curved array transducers," *Applied Sciences*, vol. 9, no. 13, 2019.

[24] M. Toulemonde, "New beamforming strategy for improved ultrasound imaging : application to biological tissues nonlinear imaging," 11 2014.

[25] K. Bernard C. and M. Patrick, *Applied Digital Optics: From Micro-optics to Nanophotonics*, ch. Appendix B. John Wiley & Sons, 2009.

[26] F. A. Duck, "The meaning of thermal index (ti) and mechanical index (mi) values," *BMUS Bulletin*, vol. 5, no. 4, pp. 36–40, 1997.

[27] Y. Zhang, Y. Guo, and W. Lee, "Ultrafast ultrasound imaging with cascaded dual-polarity waves," *IEEE Transactions on Medical Imaging*, vol. 37, pp. 906–917, April 2018.

[28] T. e. Sen, "Mechanical index," *Anatolian journal of cardiology*, vol. 15, pp. 334–6, 2015.

[29] D. Dalecki, *Biological Effects of Microbubble-Based Ultrasound Contrast Agents*, pp. 77–85. Berlin, Heidelberg: Springer Berlin Heidelberg, 2005.

[30] C. Greis, "Technical aspects of contrast-enhanced ultrasound (ceus) examinations: Tips and tricks," *Clinical hemorheology and microcirculation*, vol. 58, 09 2014.

[31] E. Tiran, T. Deffieux, M. Correia, D. Maresca, B.-F. Osmanski, L.-A. Sieu, A. Bergel, I. Cohen, M. Pernot, and M. Tanter, "Multiplane wave imaging increases signal-to-noise ratio in ultrafast ultrasound imaging," *Physics in Medicine and Biology*, vol. 60, pp. 8549–8566, oct 2015.

[32] Jong-Seon No and Hong-Yeop Song, "Generalized sylvester-type hadamard matrices," in *2000 IEEE International Symposium on Information Theory (Cat. No.00CH37060)*, pp. 472–, June 2000.

[33] P. Dijkmans, L. Juffermans, R. Musters, A. van Wamel, F. ten Cate, W. van Gilst, C. Visser, N. de Jong, and O. Kamp, "Microbubbles and ultrasound: from diagnosis to therapy," *European Journal of Echocardiography*, vol. 5, pp. 245–246, 08 2004.

[34] P. Gong, P. Song, and S. Chen, "Improved contrast-enhanced ultrasound imaging with multiplane-wave imaging," *IEEE Transactions on Ultrasonics, Ferroelectrics, and Frequency Control*, vol. 65, pp. 178–187, Feb 2018.

[35] R. J. Eckersley, C. T. Chin, and P. N. Burns, "Optimising phase and amplitude modulation schemes for imaging microbubble contrast agents at low acoustic power," *Ultrasound in Medicine & Biology*, vol. 31, no. 2, pp. 213 – 219, 2005.

[36] J. Jensen and N. Svendsen, "Calculation of pressure fields from arbitrarily shaped, apodized, and excitedultrasound transducers," in *IEEE Trans. Ultrason.*, no. 39, p. 262–267, 1992.

[37] J. Jensen, "Field: A program for simulating ultrasound systems," in *10th Nordic-BalticConference on Biomedical Imaging*, vol. 4, p. 351–353, 1996b.

[38] M. A. Lediju, M. J. Pihl, J. J. Dahl, and G. E. Trahey, "Quantitative assessment of the magnitude, impact and spatial extent of ultrasonic clutter," *Ultrasonic Imaging*, vol. 30, no. 3, pp. 151–168, 2008. PMID: 19149461.

[39] W. Guo, Y. Wang, G. Wu, and J. Yu, "Sidelobe reduction for plane wave compounding with a limited frame number," vol. 17, p. 94, 7 2018.

[40] C. H. Seo and J. T. Yen, "Sidelobe suppression in ultrasound imaging using dual apodization with cross-correlation," *IEEE Transactions on Ultrasonics, Ferroelectrics, and Frequency Control*, vol. 55, pp. 2198–2210, October 2008.

[41] A. Gholampour, S. M. Sakhaei, and S. M. H. Andargoli, "A robust approach to apodization design in phased arrays for ultrasound imaging," *Ultrasonics*, vol. 76, pp. 10 – 18, 2017.

[42] K. Diamantis, A. Greenaway, T. Anderson, J. A. Jensen, and V. Sboros, "Experimental performance assessment of the sub-band minimum variance beamformer for ultrasound imaging," *Ultrasonics*, vol. 79, pp. 87 – 95, 2017.

[43] W. Guo, Y. Wang, and J. Yu, "A sibelobe suppressing beamformer for coherent plane wave compounding," *Applied Sciences*, vol. 6, no. 11, 2016.

[44] D. Brockmann and D. Helbing, "The hidden geometry of complex, network-driven contagion phenomena," *Science*, vol. 342, no. 6164, pp. 1337–1342, 2013.

[45] T. Chernyakova, R. Cohen, R. Mulayoff, Y. Sde-Chen, C. Fraschini, J. Bercoff, and Y. C. Eldar, "Fourier-domain beamforming and structure-based reconstruction for plane-wave imaging," *IEEE Transactions on Ultrasonics, Ferroelectrics, and Frequency Control*, vol. 65, pp. 1810–1821, Oct 2018.

[46] M. Mishali and Y. Eldar, "Signal acquisition and processing in union of subspaces," 2010.